Contributions to Physics-Based Aeroservoelastic Uncertainty Analysis

Sang Wu

A dissertation

submitted in partial fulfillment of the

requirements for the degree of

Doctor of Philosophy

University of Washington

2016

Reading Committee:

Eli Livne, Chair

Mehran Mesbahi

Dorothy Reed

Frode Engelsen

Program Authorized to Offer Degree:

Aeronautics and Astronautics

University of Washington

Abstract

Contributions to Physics-Based Aeroservoelastic Uncertainty Analysis

Sang Wu

Chair of the Supervisory Committee:
Professor Eli Livne
The William E. Boeing Department of Aeronautics and Astronautics

The thesis presents the development of a new fully-integrated, MATLAB based simulation capability for aeroservoelastic (ASE) uncertainty analysis that accounts for uncertainties in all disciplines as well as discipline interactions. This new capability allows probabilistic studies of complex configuration at a scope and with depth not known before. Several statistical tools and methods have been integrated into the capability to guide the tasks such as parameter prioritization, uncertainty reduction, and risk mitigation.

The first task of the thesis focuses on aeroservoelastic uncertainty assessment considering control component uncertainty. The simulation has shown that attention has to be paid, if notch filters are used in the aeroservoelastic loop, to the variability and uncertainties of the aircraft

involved. The second task introduces two innovative methodologies to characterize the unsteady aerodynamic uncertainty. One is a physically based aerodynamic influence coefficients element by element correction uncertainty scheme and the other is an alternative approach focusing on rational function approximation matrix uncertainties to evaluate the relative impact of uncertainty in aerodynamic stiffness, damping, inertia, or lag terms. Finally, the capability has been applied to obtain the gust load response statistics accounting for uncertainties in both aircraft and gust profiles. The gust response analysis shows a significant increase of the critical loads when system's uncertainties are included.

The work is expected to make a contribution to the understanding of the propagation of uncertainty and the resulting reliability of realistic integrated aeroservoelastic system inherent in real modern aircraft. This work will motivate more research in the aeroservoelastic uncertainty area regarding both methods development in general and reliability studies of different configurations of interest. The mathematical derivations which serve as the foundation of the capability are also well documented.

TABLE OF CONTENTS

LIST OF FIGURES

LIST OF TABLES

LIST OF SYMBOLS

A_i, B_i, C_i, D_i	state space model sub matrices
A	actuator piston cross section area
[AIC]	matrix of aerodynamic influence coefficients
b	reference semi-chord
C_p	pressure coefficient
d, v, a	section displacement, velocity, and acceleration
F, M_b, M_T	section internal force, moment, and torque
f	frequency (Hz)
f_c	fluid friction factor
H	(1-cosine) gust gradient
$H(j\omega)$	transfer function
J	the pure imaginary number $\sqrt{-1}$
k	reduced frequency
K	Kernel function of the unsteady aerodynamic integral equation
K_c	valve pressure-flow coefficient
K_d	voltage amplifier
K_e	convert displacement to voltage
K_I	spool displacement per unit current
K_R	Ampere – Voltage convertor

L	scale of turbulence
L_c	leakage coefficient
L_i	lift force at box i
$\{L\}$	vector of aerodynamic normal forces
M_∞	Mach number of incoming flow
M	mass
N	sample size
p	pressure
$[P_l]$	matrices in a Roger rational function approximation
P_f / POF	probability of failure
q_D	dynamic pressure
q_F	flutter dynamic pressure
$[Q]$	generalized aerodynamic forces matrix
$\Re$, r	auxiliary variable
s	Laplace variable
slinch	inch version of slug and equal to 1 $lb \cdot s^2 / in$ or 12 *slugs*
S_{ref}	configuration reference area
S_i	area of the ith aerodynamic box
$\mathbb{S}$	statistical sensitivity index
T	complementary sensitivity function

U_∞	flight velocity
u_i	system input
V	flight velocity
V_t	total cylinder volume
W_G	magnitude of gust velocity
w	upwash
w_G	gust input profile
x_{D_i}, y_{D_i}	location of upwash point at aerodynamic box *i*
x_{L_i}, y_{L_i}	location of load point at aerodynamic box *i*
x_{vs}	actuator valve spool displacement (Eq. 15)
$\{x\}$	vector of states
y	system output
β	fluid bulk modulus
θ_o	actuator piston displacement
θ_i	desired (commanded) actuator piston displacement
Φ_w	PSD function of vertical gust velocity
Δ	absolute bound of uncertainty
μ	mean value of distribution
σ^2	variance of distribution
σ_w	root-mean-square (rms) gust velocity

Λ, λ	system input modeled as random variable
γ	aerodynamic lag term in a Roger approximation
ω	frequency (rad/sec)
$\left[\tilde{\varepsilon}(i, j)\right]$	ratios of AICs relative to baseline values
$\left[\varepsilon_l(i, j)\right]$	ratios of AICs of case l to the baseline case
η	white-noise input
ρ	density
τ	mass fraction

ACKNOWLEDGEMENTS

First I would like to express my deepest appreciation to my advisor, Professor Eli Livne, who patiently taught me the art of aeroelasticity, airplane design and optimization. Nothing of the research would have been possible without his guidance and support. Furthermore, it is his personality, enthusiasm, and the friendship between us that helped me live through the difficulties of studying and living abroad.

Secondly I would like to thank my committee member Professor K.Y. Lin who served on both my qualification exam committee and PhD committee. His partial support of my pre-doctoral study is also appreciated. Discussions with Professor Mehran Mesbahi were also very helpful and opened the gate for me for further research in area of robust control. Comments and suggestions made by Prof. Dorothy Reed and Dr. Frode Engelsen are much appreciated.

The work of the dissertation was partially supported by NASA, the Boeing Endowed Professorship of Aeronautics and Astronautics, and William E. Boeing Department of Aeronautics and Astronautics teaching assistantships. I want to thank all these companies and organizations.

Furthermore, I would like to express my appreciation to ZONA Technology, Inc., especially to the company's president Mr. P.C. Chen, who generously made it possible for me to use the ZAERO and ZEUS software capabilities during my entire PhD study. An internship opportunity I had at ZONA Technology is also appreciated.

Finally, I want to specially thank my family. My father and mother's encouragement and constant support gave me the confidence to finish my PhD studies. Their career accomplishments and lives of challenge and meaning in the aerospace industry inspired me. I am proud of them. I

feel privileged to pursue a career in the same area. I also want to express my sincere appreciation to my fiancée, who I met during my PhD life, for her support. We got engaged in 2015 and plan to get married on 2017.

DEDICATION

To my fiancée and my parents.

Chapter 1. INTRODUCTION

1.1 BACKGROUND AND CHALLENGES

Aeroelasticity is the branch of physics and engineering which studies the interactions between inertial, elastic and aerodynamic forces. It was defined by Collar in 1947 as "the study of the mutual interaction that takes place within the triangle of the inertial, elastic, and aerodynamic forces (Fig. 1.1) acting on structural members exposed to an airstream, and the influence of this study on design."

The science of aeroservoelasticity (ASE) extends the aeroelastic interactions between aerodynamic forces and a flexible structure to include a control system. The classic Collar triangle can be extended to form the aeroservoelastic pyramid (Fig. 1.1), where there are now forces resulting from the control system as well as the aerodynamic, elastic and inertial forces.

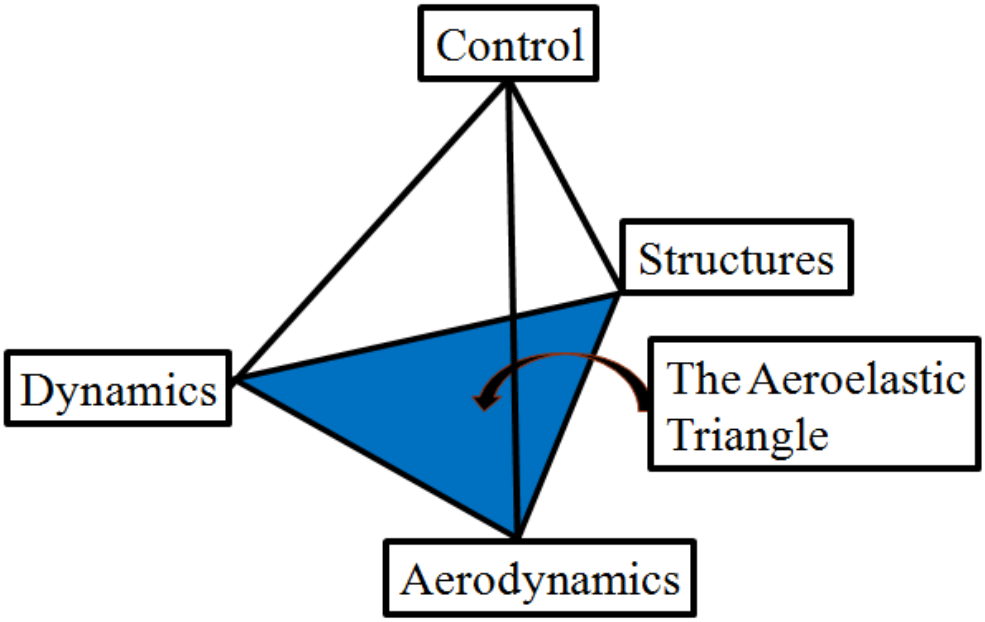

Figure 1.1. Aeroelastic / Aeroservoelastic Triangle and Pyramid

Key features of aeroservoelastic systems include dynamics, structural dynamics, aerodynamics (steady & unsteady), actuator, sensing, control and the mutual interaction between them. (Fig. 1.2). Some typical system parameters and behavior measures for the aeroservoelastic system are listed below.

1. Structures:

   General: element topology, shape and sizing.

   Composites: material properties, fiber directions, stacking order, skin, spar and rib web thickness.

   Mass distribution: non-structural and structural mass distribution.

2. Aerodynamics:

   Geometry, topology, surface properties.

   Atmospheric properties, flight conditions such as Mach number, Reynolds numbers and reduced frequency.

3. Control:

   Actuators: In the case of electro-hydraulic actuators: inertias of parts, hydraulic fluid properties, inner & outer geometry, command valve parts properties (mechanical & electrical), actuator closed loop control structure, and actuator - airframe attachments.

   Sensors: properties of parts (mechanical, electrical, optical) and inner structure, sensor - airframe attachments.

4. External inputs:

   Gust excitation, landing impact, sudden mass changes (external stores ejection), pilot commands to vehicle control effectors, other environmental effects (such as temperature, moisture absorption, etc. affecting structure, actuators, and sensors).

5. System's behavior:

Stability (as quantified using various measures)

Dynamic response to external excitation (rigid body motions, elastic deformations, vibration levels, internal dynamic loads, internal stresses, activity level of actuators, dynamics of actuator supporting hydraulic and electrical systems)

The ASE systems Inputs - Outputs information flow is shown in Fig. 1.2. The inner box shows the simulations of the dynamics of ASE systems where parameters that describe the structure dynamics, unsteady aerodynamics, control law as well as mesh interpolation are defined. The interaction between structure dynamics and aerodynamics are coupled by system equations of motion. The outer box defines, depending on the specific simulation and task, the input and output of the system.

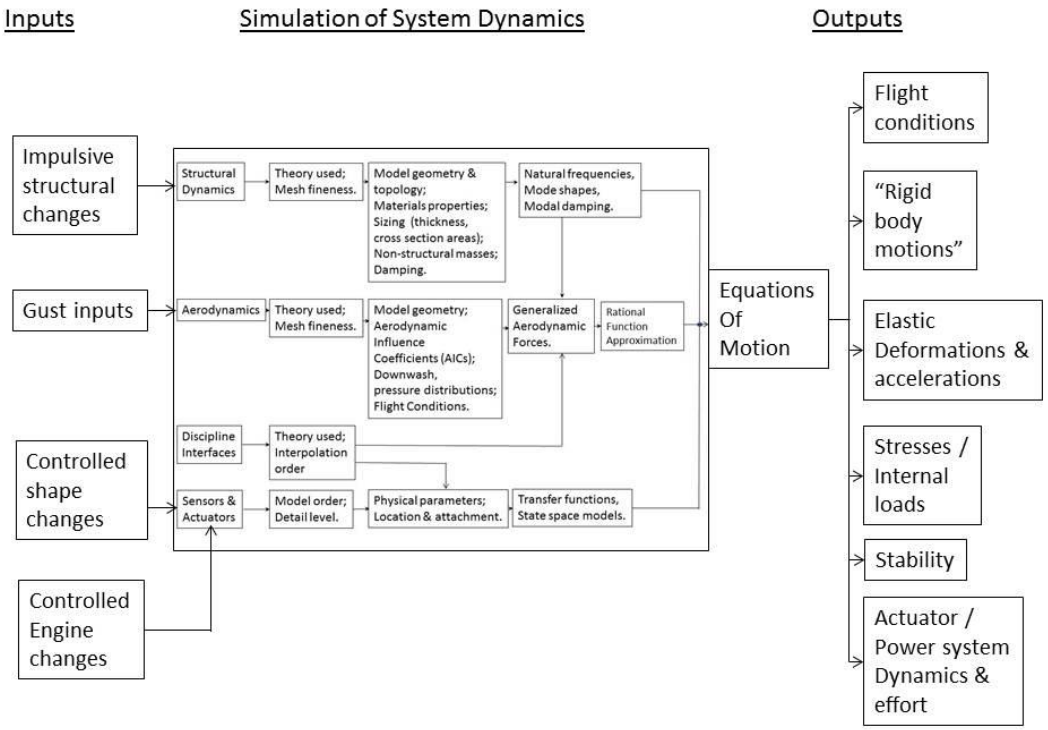

Note: the engine in the diagram above is treated as another actuator.

Figure 1.2. ASE systems Inputs / Outputs flow

ASE simulations, wind tunnel tests, and flight tests technology has been developed from the 1960s (even earlier) and has reached a level of maturity that allows actual airplane application. However, the technology implementation is not complete and requires more development in areas such as: nonlinear structures, structural damping modeling, aerodynamic nonlinearities, ground and flight testing, etc.

The importance of uncertainty in aeroelastic and aeroservoelastic simulations has been recognized for a long time and addressed traditionally by the designers and developers of new aircraft through comprehensive parametric studies covering the range of expected variation of key structural and aerodynamic parameters. The emergence of powerful computers capable of running multiple aeroservoelastic simulations within practical time and computer resource limitation has led to a growing number of efforts to develop new methods for addressing the aeroservoelastic uncertainty problem. Reviews of uncertainty evaluation approaches in aeroelasticity can be found in [1,2] and recently in [3].

With the help of high performance computing direct Monte Carlo simulations have been used to find the probability of flutter failure with consideration of structural uncertainty due to manufacturing [4-6], aerodynamics uncertainty via correction factor techniques [7], as well as uncertainty quantification combined with damage tolerant composite structure design [8]. To overcome the challenge posed by the need to carry out many computationally expensive aeroelastic simulations, reduced order or surrogate modeling methods have been proposed, such as response surface methods, perturbation methods, and first or second order reliability methods (FORM or SORM) that would allow speeding up the simulation process. Representative works in this area are reported in [9-12]. Approaching the problem from another perspective – that of Robust Control Theory and it derivative methods - another set of publications addressing

aeroelastic and aeroservoelastic uncertainty use a non-probabilistic approach, e.g. robust flutter analysis [13-18], the μ-k method [16] and μ-p method [17].

The current challenges in the existing research on aeroelastic uncertainty can be classified into

1. Uncertainty Approaches:
   (1) FORM and SORM – challenge: approximation may miss nonlinear effects such as mode switching, etc.
   (2) Response surface or surrogate models followed by Monte Carlo Simulations – Challenges: computational cost of creating surrogate models when many variables are involved. The potential of missing mode switching and other nonlinear effects.
   (3) Robust control based approaches – Challenges: computational cost, form of source of uncertainty requirement, may be over conservative.
   (4) Direct Monte Carlo approaches – Challenges: Computational cost for high confidence and low error.
2. Aeroelastic uncertainty modeling
   (1) Structural uncertainty – stiffness and inertia variation, structural damping variation.
   (2) Unsteady aerodynamic – the power and limitation of linear theories, correction factors, CFD and the CFD challenges: separation and other nonlinear mechanisms, turbulence modeling, shock and boundary layer interaction, the huge computational costs. The limitations of reduced order models (ROMs)
   (3) Flight conditions uncertainty
3. Very limited work done on uncertainty and system identification (ID) in ground vibration testing and flutter flight testing.

4. Aeroservoelastic uncertainty and reliability (the added complexity with the addition of active control):

   Past work mainly within the Robust Control approach and focused on robust controller design. Very limited work has shown that control component modeling accuracy can have a major impact on ASE simulation results, but no thorough uncertainty / reliability work has been reported that also covers actuator uncertainty.

5. Aeroservoelastic ASE simulation capabilities for real aircraft applications:

   (1) NASTRAN (with limited ASE capability and no built in coupling with modern control)

   (2) ZAERO and ZEUS (coupling with modern control, but no seamlessly integrated structural part. Depends on NASTRAN and other FE tools)

   (3) The commercial codes are expensive, especially when run using parallel processing, which is a must for Monte Carlo simulations.

   (4) Other capabilities in the US and Europe (NASA DYLOFLEX, Karpel's DYNRESP, NASA STARS, etc.) – none allows access to all elements of the ASE model and none was built for uncertainty simulations.

Based on the above discussion, this research has been focused on developing a self-contained industry-appropriate (in terms of complexity and realism) aeroservoelastic analysis simulation tool to perform reliability analyses covering all aspects of system uncertainty. The simulation capability is tailored for efficient Monte Carlo simulations using the state of the art parallel computing of realistic ASE systems.

1.2 THE NEEDS AND GOALS

While commercial codes such as NASTRAN and ZAERO, and similar capabilities developed by aircraft companies, universities, and government organizations for their own use exist, they are either expensive to license and difficult to modify for special needs, or not available to the public. Because of the need in this project to run massive Monte Carlo simulations of aeroservoelastic systems, covering variations in the structural, aerodynamic and control characteristics of airplanes as well as the flight conditions and the environment in which they operate, and because of the need to allow numerical experiments with unusual modeling approaches and numerical details that are not available with the commercial codes, it was decided to develop, in parallel with reliance on commercially available tools such as NASTRAN and ZAERO, an independent self-contained aeroservoelastic modeling capability.

The development of such a comprehensive aeroservoelastic capability was a major effort that was challenging to complete. Nevertheless, the need for a capability that would make it possible to fully access all its modules and parts for code adjustments and adaptations to allow the study of different research questions was important enough to justify such a development.

The aeroservoelastic MATLAB capability developed includes the following features:

For the structural dynamic modeling part three-dimensional beams, springs, and composite plate element form the core of the structural dynamic modeling capability. The elements and associated analysis methods were carefully selected to allow modeling accuracy and complexity that are industry standard.

For the unsteady aerodynamic part a Doublet Lattice modeling capability was developed, together with the necessary mesh to mesh spline. Based on an Aerodynamic Influence

Coefficients (AIC) approach, the new capability can accept CFD-based AICs from a variety of CFD codes.

The aeroelastic and aeroservoelastic modeling part include frequency domain and state space stability analysis options, together with frequency domain and time domain gust response simulation options. Modeling of complete aeroservoelastic systems is allowed, including the modeling of sensors and actuators at different levels of fidelity and complexity as well as the incorporation of control laws of various types.

The creation of such a capability can be viewed as a design and construction of an experimental apparatus and a set up for tests that had not been possible before. A detailed review of the development of this capability is summarized in Chapter 2.

Topics that have been developed and performed using the capability developed are listed below:

1. The effect of control component uncertainty on coupled ASE behavior. (Chapter 3)
2. Adding to the body of knowledge on flutter (ASE stability) uncertainty. (Chapter 3)
3. Testing of several alternative methods for representing aerodynamic uncertainties and studying their effects. (Chapter 4)
4. Adding to the body of knowledge on gust response uncertainty. (Chapter 5)

Chapter 2. TOOL DEVELOPMENT

2.1 THE MATLAB BASED FEM CAPABILITY

Important finite elements used in the FE modeling of wing structures are membrane and plate elements (used to model skins and webs), truss rod elements (used to model; spar and rib caps), and beam as well as rigid bar elements (used to model local reinforcements and attachment areas or link masses to the nodes they should be attached to). Beam elements are often used to model complete wings, in what is called “the stick model”, where in the case of high aspect ratio wings a detailed finite element model of the structures can be replaced by an equivalent stick model with resulting simplicity and computational efficiency.

When composite materials are used to construct airframe structures their anisotropic properties, representing the different directions of layers making the laminates used for skins, webs, and caps, must be modeled properly for both stiffness simulation and the prediction of stress related failure.

The aeroelastic simulation capability developed in the project is based on a finite element (FE) model in Matlab using four key elements: a truss element for modeling spar and rib caps, a composite triangular shell element for skins and webs, beam element for stick model and mass element for lumped mass. The flat triangular shell element from P. Mohan [18] was selected because of demonstrated good performance in linear and nonlinear cases and the availability of a detailed presentation of its development and key equations.

In order to use a finite element code (FE) correctly and efficiently, especially when optimization is involved, it is important to understand the assumptions and mathematical derivations used to develop the finite elements used in the modeling of the structures involved.

Such insight into the properties of the finite elements involved would lead to efficient modeling, efficient sensitivity analysis, efficient approximation, and efficient parametrization for optimization.

The triangular element used in this study is obtained by combining the Discrete Kirchhoff Theory (DKT) Plate bending element of Batoz et al. and a membrane element with drilling degrees of freedom derived from the well-known Linear Strain Triangular (LST) element [18]. A more detailed derivation of this element can be found in Appendix A.

A comparison was performed to verify the accuracy of the FEM capability. A simple FEM modal analysis was taken from the ZAERO application manual for comparison. Fig. 2.1 plots the FEM model which is using plate elements only. The element properties are

$$E = 9.24\times10^{6}\ psi,\ \upsilon = 0.33,\ t = 0.041in,\ \rho = 2.52\times10^{-4}\ slinch/in^{3}$$

Where E is Young's modulus of the material, υ is the Poisson's ratio, t is the plate thickness and ρ is the material density. *slinch* is the inch version of slug and equal to 1 $lb\cdot s^2/in$ or 12 *slugs*.

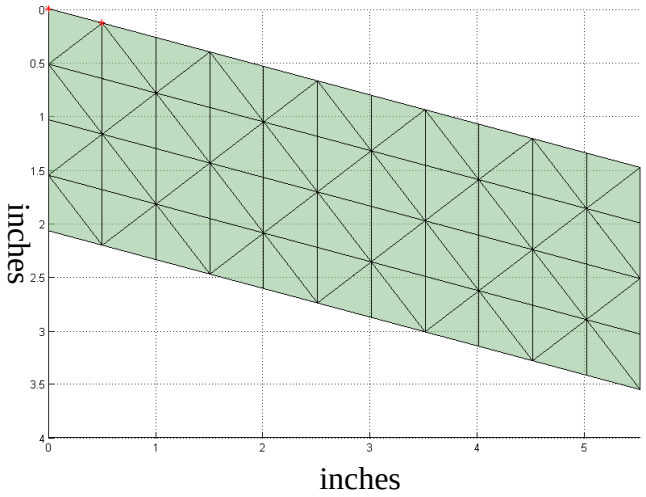

Figure 2.1. FEM model of the 15 deg backswept wing

The FEM modal analysis is illustrated in Table 2.1.

Table 2.1. Comparison of results from modal analysis

Mode NO.	Frequency (UW Code) Hz	Frequency (NASTRAN) Hz	Error
1	40.52	40.26	0.64%
2	216.04	210.2	2.78%
3	261.68	258.0	1.43%
4	649.19	629.9	3.06%
5	777.22	751.2	3.46%

In these modal analyses, the results agree with those of NASTRAN. The finite element code has been validated using other cases and was found suitable for the aeroelastic analyses that would follow.

2.2 UNSTEADY AERODYNAMICS – THE DOUBLET LATTICE METHOD

Aerodynamic compressibility is an important factor in the flutter of high speed air vehicles. It is impossible to solve the unsteady aerodynamic equations without the help of high speed computers. The kernel-function and doublet-lattice method (DLM), for linearized subsonic flows, were developed to take advantage of improvements in digital computer technology. During the past two decades, the simulation of flow around more complicated shapes of objects has been becoming more tractable by CFD. However, the high cost and technical complications associated with non-linear CFD as well as the proven success of DLM (and equivalent methods such as ZAERO) leads to it still being used heavily for the subsonic flutter clearance of airplanes being designed today.

Since the research focus here is on the system's reliability and uncertainty propagation of aeroservoelastic parameters, it was necessary to develop an open source code which would allow access to all aerodynamic terms and parameters. Current commercial codes are packaged as black boxes, which makes it difficult to add uncertainty effects to all unsteady aerodynamic

terms. For this reason we developed our own unsteady aerodynamic code based on doublet lattice method.

A detailed derivation of the mathematics of the doublet lattice method and calculation of generalized aerodynamic forces can be found in Appendix B.

Similar to the finite element code, the doublet lattice code was validated using published aerodynamic results before it was applied to aeroelasticity simulation problems.

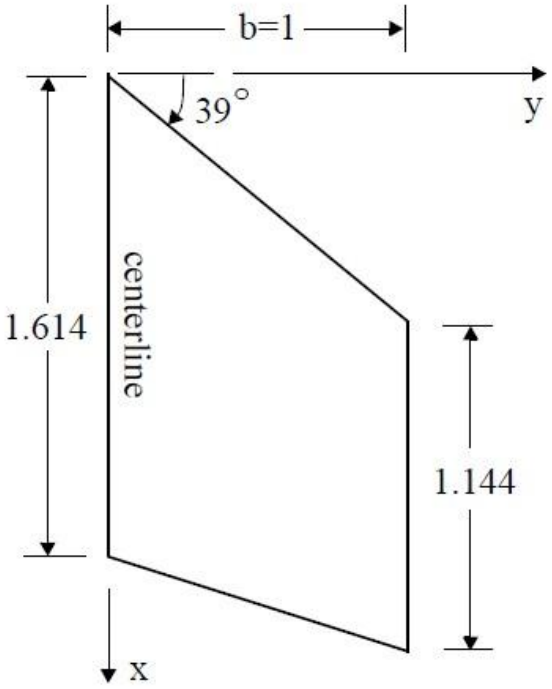

Figure 2.2. Sketch of the swept and tapered wing

One example used is taken from Max Blair [19]. It is a non-dimensional swept and tapered wing with aspect ratio 1.45. The right half of the wing is depicted in Fig. 2.2. The flow is at Mach 0.8. In all cases, the lift due to wing pitch is calculated. For the steady case, we calculated the lift curve slop. For unsteady case, the wing is pitched about the y axis at k=1.4 where k is the reduced frequency and calculated as $k = \omega b/V$.

The results are compared with the report [19] and summarized Table 2.2.

Table 2.2. Unsteady aerodynamics comparison

H7WC

	k=0	k=1.4	
Panel Density	REAL	ABSOLUTE	PHASE(deg)
5 *5	2.32	7.26	77.20
10*10	2.23	7.40	73.95

LATIS

	k=0	k=1.4	
Panel Density	REAL	ABSOLUTE	PHASE(deg)
5 *5	2.3259	7.2748	77.9600
10*10	2.2330	7.7201	79.8095

UW Unsteady Aerodynamic Code

	k=0	k=1.4	
Panel Density	REAL	ABSOLUTE	PHASE(deg)
5 *5	2.3263	7.2577	77.4929
10*10	2.2334	7.3652	74.3525

Both the H7WC code and LATIS code required some steady state correction. The comparison indicates that the DLM code for the project captured the published results well. The new DLM capability developed for this research was thoroughly validated, using “pure” aerodynamic runs as well as aeroelastic cases. Its full potential would become evident in the studies of methods for accounting for aerodynamic modeling uncertainties.

2.3 THE AEROSERVOELASTIC STATE-SPACE MODEL

A complete aeroservoelastic (ASE) model includes the aeroelastic plant, a sensor block, an actuator block, a control law, and a gust filter. The aeroelastic plant includes flexible aircraft structural dynamics, unsteady aerodynamics, and gust response. The closed loop ASE system [20-23] is shown in the block diagram of Fig. 2.3.

A detailed derivation of the state-space model can be found in Appendix C. The simulation capability allows access (regarding parameter variations, model fidelity/complexity changes, uncertainty modeling, and any approximation concept techniques) to all elements/components of

the integrated coupled ASE system at all levels of detail. A summary of the key equations is presented here.

The state-space form of the sub-system equations of motion are shown as

Aeroelastic Plant

$$s\{x_P\} = [A_P]\{x_P\} + [B_C]\{u_C\} + [B_G]\{u_G\} \quad (2.1)$$

$$\{y_P\} = [C_P]\{x_P\} + [D_C]\{u_C\} + [D_G]\{u_G\} \quad (2.2)$$

Actuators

$$s\{x_{ACT}\} = [A_{ACT}]\{x_{ACT}\} + [B_{ACT}]\{u_{ACT}\} \quad (2.3)$$

$$\{y_{ACT}\} = [C_{ACT}]\{x_{ACT}\} \quad (2.4)$$

Sensors

$$s\{x_{SEN}\} = [A_{SEN}]\{x_{SEN}\} + [B_{SEN}]\{u_{SEN}\} \quad (2.5)$$

$$\{y_{SEN}\} = [C_{SEN}]\{x_{SEN}\} \quad (2.6)$$

Control Laws

$$s\{x_{CON}\} = [A_{CON}]\{x_{CON}\} + [B_{CON}]\{u_{CON}\} + [B_{PILOT}]\{u_{PILOT}\} \quad (2.7)$$

$$\{y_{CON}\} = [C_{CON}]\{x_{CON}\} + [D_{CON}]\{u_{CON}\} + [D_{PILOT}]\{u_{PILOT}\} \quad (2.8)$$

The control law formulation can be adapted to cases of Multiple-Input Multiple-Output (MIMO) control laws in transfer function form, or directly in state space form, including linear-quadratic regulator (LQR) or Linear-Quadratic-Gaussian (LQG).

After linking the subsystems together, the closed loop aeroservoelastic system can be written in the state-space form as:

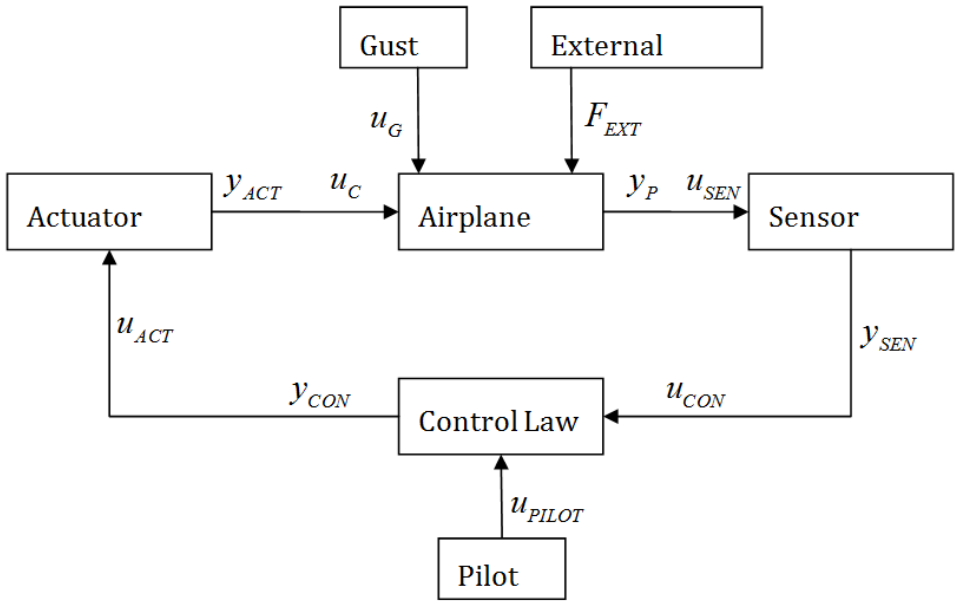

Figure 2.3. Closed loop flow chart of ASE system

$$s\{x_{SYS}\} = [A_{SYS}]\{x_{SYS}\} + [B_{GSYS}]\{u_G\} + [B_{PILOTSYS}]\{u_{PILOT}\} \tag{2.9}$$

where:

$$\{x_{SYS}\}^T = \left\{\{x_P\}^T \quad \{x_{SEN}\}^T \quad \{x_{ACT}\}^T \quad \{x_{CON}\}^T\right\} \tag{2.10}$$

$$[A_{SYS}] = \begin{bmatrix} [A_p] & [0] & [B_C][\bar{C}_{ACT}] & [0] \\ [B_{SEN}][C_P] & [A_{SEN}] & [B_{SEN}][D_C][\bar{C}_{ACT}] & [0] \\ [0] & [B_{ACT}][D_{CON}][C_{SEN}] & [A_{ACT}] & [B_{ACT}][C_{CON}] \\ [0] & [B_{CON}][C_{SEN}] & [0] & [A_{CON}] \end{bmatrix} \tag{2.11}$$

$$[B_{GSYS}] = \begin{bmatrix} [B_G] \\ [B_{SEN}][D_G] \\ [0] \\ [0] \end{bmatrix} \tag{2.12}$$

$$[B_{PILOTSYS}] = \begin{bmatrix} [0] \\ [0] \\ [B_{ACT}][D_{PILOT}] \\ [B_{PILOT}] \end{bmatrix} \tag{2.13}$$

$$\left[\bar{C}_{ACT}\right]=\begin{bmatrix}[C_{ACT}]\\ [C_{ACT}][A_{ACT}]\\ [C_{ACT}][A_{ACT}][A_{ACT}]\end{bmatrix} \tag{2.14}$$

Realizing that the airplane's input $\{u_C\}$ requires displacement, velocity and acceleration of the control surfaces, $\left[\bar{C}_{ACT}\right]$ is defined to transformation the actuator output $\{y_{ACT}\}$ to $\{u_C\}$. A detailed derivation can be seen in Appendix C.

Equation (2.9) can cover both time domain simulation and frequency domain simulation of coupled aeroservoelastic systems accounting for all their sub-systems and components.

The resulting aeroservoelastic simulation capability, including the aeroservoelastic formulation, the structural finite element method (FEM), Doublet Lattice Method (DLM) unsteady aerodynamics, and Fluid-Structures Interaction (FSI) equations, has been created in the MATLAB environment. It is an independent simulation tool that leads to the reliability analysis.

2.4 AEROELASTIC SYSTEM WITH GUST EXCITATION

A block diagram of an integrated aeroservoelastic system with gust input and loads output is shown in Fig. 2.4. The detailed derivation of the state-space model with gust excitation can be found in Appendix C.

The mathematical model for closed loop aeroservoelastic plant, sensors, actuators and control law are same as those defined in Chapter 2.3 with Equation (2.1) – Equation (2.14).

A detailed discussion of the definition of gust profile can be found in Chapter 5. A state space gust input model can be used to convert a white-noise input to a gust input of desired power spectral density characteristics. The subscript G is used for the state space model of gust inputs in such a case. Similarly, control laws can be modeled using a dynamic state space model using subscript CONT.

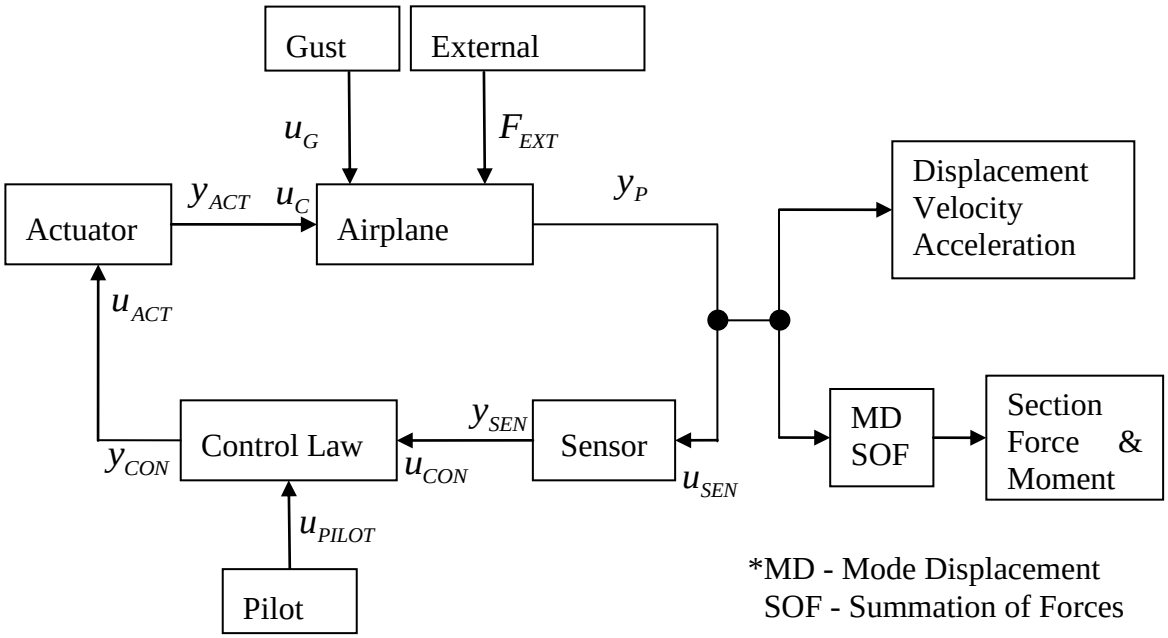

Figure 2.4. Block diagram of aeroelastic / aeroservoelastic system

Using the subscript SYS, the integrated system, including aeroelastic plant, actuators, and sensors, for the open-loop case (no closed-loop via control laws), and with gust inputs is modeled by:

$$s\{x_{SYS}\} = [A_{SYS}]\{x_{SYS}\} + [B_{GSYS}]\{u_G\} \tag{2.15}$$

where the states of the integrated system are:

$$\{x_{SYS}\}^T = \left\{ \{x_P\}^T \quad \{x_{SEN}\}^T \quad \{x_{ACT}\}^T \right\} \tag{2.16}$$

Key system matrices are:

$$[A_{SYS}] = \begin{bmatrix} [A_p] & [0] & [B_C][\bar{C}_{ACT}] \\ [B_{SEN}][C_P] & [A_{SEN}] & [B_{SEN}][D_C][\bar{C}_{ACT}] \\ [0] & [B_{ACT}][D_{CON}][C_{SEN}] & [A_{ACT}] \end{bmatrix} \tag{2.17}$$

$$[B_{GSYS}] = \begin{bmatrix} [B_G] \\ [B_{SEN}][D_G] \\ [0] \end{bmatrix} \tag{2.18}$$

$$[\bar{C}_{ACT}] = \begin{bmatrix} [C_{ACT}] \\ [C_{ACT}][A_{ACT}] \\ [C_{ACT}][A_{ACT}][A_{ACT}] \end{bmatrix} \tag{2.19}$$

And the vector of gust speeds and accelerations is:

$$\{u_G\} = \{w_G \quad \dot{w}_G\}^T \tag{2.20}$$

Similar as Eq(2.9), $\left[\bar{C}_{ACT}\right]$ is defined to transformation the actuator output $\{y_{ACT}\}$ to airplane's input $\{u_C\}$.

Outputs provided by the state space model of the integrated system can include displacements, velocities, and accelerations at points on the airframe, as well as internal stresses or internal cross-sectional forces and moments along wings and fuselages.

The output of the aeroelastic system can be written as

$$\{y\}^T = \left\{\{F\}^T \quad \{M_b\}^T \quad \{M_T\}^T \quad \{d\}^T \quad \{v\}^T \quad \{a\}^T\right\} = \left[C_{output}\right]\{x_{SYS}\} + \left[D_{output}\right]\{u_G\} \tag{2.21}$$

where $\{F\},\{M_b\},\{M_T\}$ are forces, bending moments, and torsional moments, respectively. $\{d\},\{v\},\{a\}$ are the displacements, velocities, and accelerations at specific locations, respectively. The matrices $\left[C_{output}\right]$ and $\left[D_{output}\right]$ are determined by either mode displacement (MD) or summation of forces (SOF) method for dynamic loads recovery. Detailed discussions of MD and SOF methods can be found in [26-28].

2.5 PROBABILISTIC AEROSERVOELASTIC ANALYSIS

The aeroservoelastic (ASE) simulation capability is used by a Monte Carlo (MC) "case driver" to produce response results for ASE systems of varying parameters and inputs, covering uncertainties in the structure, aerodynamics, actuators and sensors, gust and pilot inputs, and flight conditions. Responses, whose variation due to uncertainties in all parameters are generated by the ASE simulation capability, include ASE poles, flutter speeds, modal response to gust and

pilot inputs, physical response to gust and pilot inputs in the form of accelerations, deformations, and loads in the structure, as well as levels of activity of control surfaces and actuators.

The Monte Carlo "case driver" code prepares input sets to be sent to the ASE simulation capability for analysis and it receives the results and processes them to generate the statistical information desired (Figure 2.5).

Therefore, in the following chapters, the aeroservoelastic uncertainty simulation will be separately considered as topics.

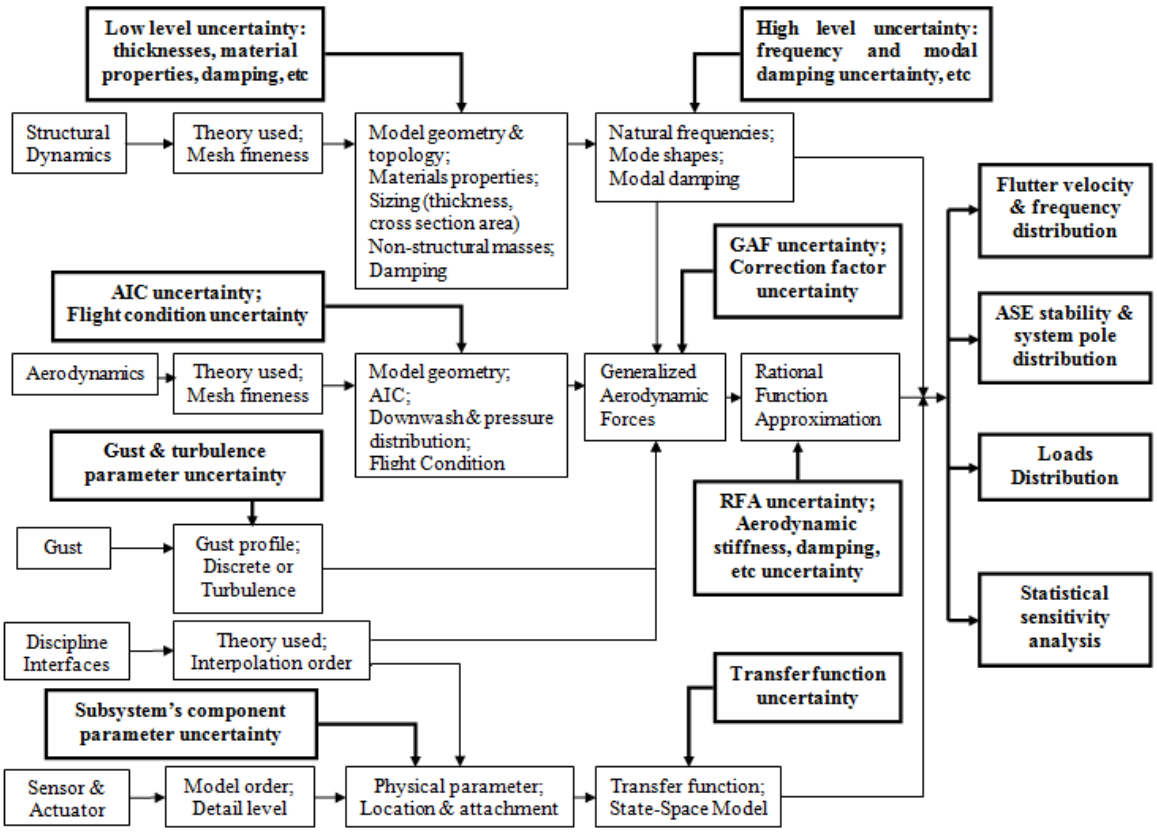

Figure 2.5. Uncertainty propagation in integrated aeroservoelastic models

Chapter 3 focuses on the aeroservoelastic simulation with the control system component uncertainty. The classic notch-filter control design which used to solve the control – structural

interaction problem is challenged by considering the system components uncertainty. The uncertainties are included in the detailed model parameters of the control actuator, material properties and modeling of the control surface, as well as the aerodynamic uncertainty via the rational function approximation. All the test cases show that the notch filter can fail to stabilize the aircraft. Statistical global sensitivity analysis is introduced in this chapter and used to rank the influence of the uncertain parameter to the system's output of interest. Several statistical tools are used to guide the redesign process to enhance the robustness of the notch filter control law including Bayesian updating theory and auxiliary variable method.

Chapter 4 reviews several methodologies that cover the unsteady aerodynamic uncertainty in the flutter analysis. A new way that considers the aerodynamic uncertainty by emphasizing the physical significance and averaging the differences between several unsteady aerodynamic models is developed. The results also compared with the aerodynamic uncertainty approach demonstrated in Chapter 3 using Roger approximation method uncertainty scheme. Structural uncertainties are included through both detailed level (thickness and density) and higher level (natural frequency and modal damping) structural dynamics. Global sensitivity analysis is used in ranking the relative effects of uncertainty parameter to the variance of the output flutter velocity and frequency both aerodynamically and structurally.

Chapter 5 considers the effects to the dynamic loads due to structural and gust profile uncertainty. Both the discrete gust and turbulence models are considered in time and frequency domain with and without uncertainty. Structural uncertainties are considered in the modeling of the stick model aircraft.

Chapter 3. PROBABILISTIC AEROSERVOELASTIC RELIABILITY ASSESSMENT CONSIDERING CONTROL SYSTEM COMPONENT UNCERTAINTY†

3.1 OVERVIEW

The complex nature of uncertainty propagation in aeroservoelastic systems, which are inherently multidisciplinary, makes Monte Carlo simulation methods desirable tools for statistical analysis. With the growing efficiency of analysis methods coupled with growing computing power, such Monte Carlo methods, which were computationally impractical in the past, can now be used to simulate real flight vehicles at industry level of complexity and accuracy and allow statistical analysis of aeroservoelastic behavior on a scope and with depth not possible before. This chapter describes the development of a new fully-integrated computational capability for Monte Carlo simulations of uncertain aeroservoelastic systems and presents results that add important insights regarding their reliability and overall uncertainty. The new capability allows selection of uncertain variables at all levels of details of modeling in all disciplines involved. As an important example, the focus of the work described here is to evaluate the robustness of the "notch-filter" approach, commonly used to decouple aeroelastic and structural dynamic behavior and stabilize unfavorable aeroservoelastic interactions in cases where such interactions lead to instability. It is shown that attention has to be paid, if notch filters are used in the aeroservoelastic loop, to the variability and uncertainties of the aircraft involved. Uncertain parameter prioritization and risk mitigation are proposed through sensitivity analysis and Bayesian updating.

---

†Content of this chapter is published in [25], [119]

3.2 INTRODUCTION

The importance of uncertainty in aeroelastic and aeroservoelastic simulations has been recognized for a long time and addressed traditionally by the designers and developers of new aircraft by using comprehensive parametric studies covering the range of expected variation of key structural and aerodynamic parameters. The emergence of powerful computers capable of running multiple aeroservoelastic simulations within practical time and computer resources has led to a growing number of efforts to develop new methods for addressing the aeroelastic uncertainty problem.

In previous aeroelastic uncertainty studies available in the literature, the number and detail of treatment of the uncertain aeroservoelastic problems have been quite limited. Structural and aerodynamic sources of uncertainty have been addressed in different ways, but have not include the treatment of uncertainties due to variations in parameters of system actuators and other elements of the control system. While transfer functions of control system elements, such as actuators, can be measured more easily than structural and aerodynamic characteristics, such elements may change dynamic behavior after hours of operation due to environmental effects, maintenance, and wear. Because of the computational difficulty of accounting for numerous uncertain variables simultaneously, uncertainty in aeroservoelastic models has been often assigned to “high-level” variables such as natural frequencies and mode shapes, or generalized aerodynamic loads, or the frequency domain transfer functions of actuators, and not to the physical parameters which characterize detailed local action. In addition, when used within the framework of Robust Control Theory, models of the variation of system parameters and equations had to be cast in a form suitable for Robust Control.

The purpose of the work reported in this chapter is to explore the effects of uncertainty in detailed models of the operation of control system elements on the stability of the entire aeroservoelastic system through expanding the work presented in [6]. Once identified the circumstances that would cause variations of control element dynamic behavior to lead to aeroservoelastic instability problem, a feasible methodology for aeroservoelastic risk reduction would be proposed.

A brief derivation of an integrated actuators, aeroelastic plant, sensors and control laws state-space model of an aeroservoelastic system is presented in this chapter, followed by a detailed description of a typical aviation servo-hydraulic actuator used for aeroservoelastic control. It is well known that parameters such as fluid bulk modulus, viscous friction, and leakage can vary with the change of operating temperature, manufacture processes, as well as the aircraft aging. Uncertainty in the actuator's dynamics model is addressed by modeling uncertainties in those physical parameters that are known to be sensitive to change. In addition to the control element uncertainty, both structural and aerodynamic uncertainties are fully covered by the aeroservoelastic simulation.

To study the effects of such uncertainties, a representative roll rate control system designed for the Advance Fighter Aircraft (AFA) model presented in [19] is used. In this case a notch filter had been designed and utilized in the aircraft flight control system to avoid certain flutter problems induced by control - structural interaction. This has been common practice for years in decoupling aeroelastic behavior from high authority flight control systems [20], although disadvantages had led over the years to alternative solutions [21]. The study will show, however, that due to uncertainty in the system, including uncertainty in the dynamics of its actuators, a notch filter (or any pre-set control system) may be ineffective and that there is probability that it

would not be able to prevent system failure. The results should influence the way notch filters are designed for aeroservoelastic applications or to the adoption of other control techniques such as adaptive control as suggested in [22].

In addition, a methodology is proposed for reduction of the probability of system failure due to control element uncertainty. A statistical global sensitivity analysis is used to quantitatively rank the relative importance of uncertain control system parameters to the stability of the overall aeroservoelastic system. Based on the results of the sensitivity analysis, a rapid way of updating probability evaluation is presented by using the Bayesian theorem and auxiliary variable method with the suggested uncertain parameter modification.

3.3 MODEL DERIVATION

3.3.1 *The Aeroservoelastic State-Space Model*

A complete aeroservoelastic (ASE) model includes the aeroelastic plant, a sensor block, an actuator block, a control law, and a gust filter. A summary of the derivation of the closed loop system is shown in Chapter 2.3 and the detailed derivation can be referred to Appendix C.

3.3.2 *Model of Electrohydraulic Servo Actuator*

Electrohydraulic servo actuators are widely used on modern aircraft [29]. Detailed mathematical models of servo-hydraulic actuators were created and tested in the past, e.g. [30-34]. For demonstration study purposes, a servo-hydraulic actuator with a simple position control system is selected here, Fig. 3.1. This system is made of an electrohydraulic servo valve for directing fluid to a cylinder / piston system by applying to the electrical coils of the valve a voltage which is directly proportional to the error between desired position and actual position at any instant.

The servo valve voltage input is zero for the reference position of the actuator. A change in the demand voltage coming from a control computer initiates a voltage difference applied to the coils of the servo valve, thereby causing the displacement of the valve spool. The resulting flow of fluid through the valve would cause the piston to move, which, in turn, alters the voltage from the output potentiometer. This voltage is subtracted from the demand voltage and reduces the voltage difference. The valve stops and ceases the motion of piston once the two voltages are equal again.

The relationship between actuator piston displacement θ_o and valve spool displacement x_{vs} may be written as [29]:

$$\frac{\dot{\theta}_o}{x_{vs}} = \frac{K_q / A}{\left(1/\omega_h^2\right)s^2 + \left(2\zeta/\omega_h\right)s + 1} \tag{3.1}$$

where

$$\omega_h^2 = \frac{4\beta}{V_t}\frac{A^2}{M} \tag{3.2}$$

$$\zeta = \left(L_c + K_c + \frac{f_c V_t}{4\beta M}\right)\frac{1}{A}\sqrt{\frac{M\beta}{V_t}} \tag{3.3}$$

β is the fluid bulk modulus, A is the piston cross section area, V_t is the total cylinder volume, M is the mass, L_c is the leakage coefficient, K_c is the valve pressure-flow coefficient and f_c is the fluid friction factor.

Neglecting the dynamics of the servovalve (its dynamic response can be an order of magnitude faster than that of the actuator), the servo valve displacement x_{vs} will be directly proportional to the control current flowing into the valve coil ($x_{vs} = K_I I_c$) and Equation (3.1) is rewritten as

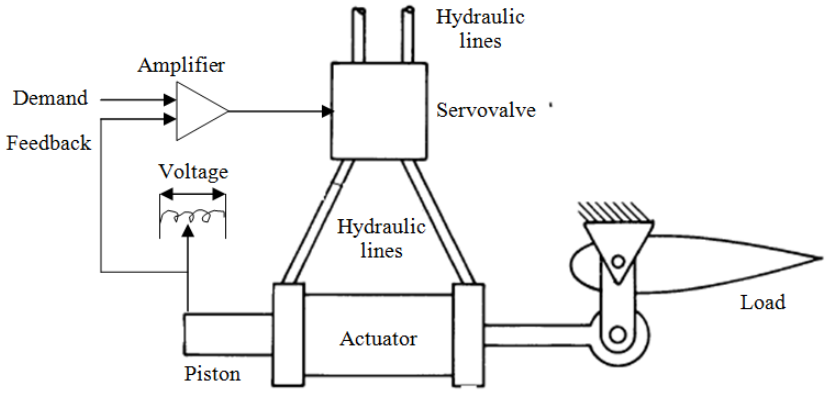

Figure 3.1. Schematic representation of proportional position control actuator loop

$$\frac{\dot{\theta}_o}{I_c} = \frac{K_I K_q / A}{\left(1/\omega_h^2\right)s^2 + \left(2\zeta/\omega_h\right)s + 1} \tag{3.4}$$

The proportional control means that the control signal will be a voltage proportional to the measured error and equals to $K_e\left(\theta_i - \theta_o\right)$. The voltage may be also amplified by a coefficient denoted as K_d. If the servo-valve coil has an electric resistance of K_R, the control current I_c in Equation (3.4) can be written as

$$I_c = K_R K_e K_d \left(\theta_i - \theta_o\right) \tag{3.5}$$

Using Equation (3.5) in Equation (3.4):

$$\frac{\dot{\theta}_o}{\theta_i - \theta_o} = \frac{K_R K_e K_d K_I K_q / A}{\left(1/\omega_h^2\right)s^2 + \left(2\zeta/\omega_h\right)s + 1} \tag{3.6}$$

The transfer function of the actuator is defined as the ratio between the desired output θ_i, provided by the control computer, and the actual piston position θ_o. Derived from Equation (3.6), the actuator transfer function may be written as

$$TF = \frac{\omega_h^2 K}{s^3 + 2\zeta\omega_h s^2 + \omega_h^2 s + \omega_h^2 K} \tag{3.7}$$

where

$$K = \left(K_R K_e K_d K_I K_q\right) / A \tag{3.8}$$

A general expression for an actuator transfer function can be written as:

$$TF = \frac{b_0}{s^3 + d_2 s^2 + d_1 s + d_0} \tag{3.9}$$

Equation (3.7, 3.9) and the equations for their parameters provide a direct and clear link between physical parameters and the resulting transfer function coefficients. Such a model allows identification, through Monte Carlo simulations, of the effects of physical parameters on the statistical distribution of aeroservoelastic (ASE) results rather than physically meaningless transfer function coefficients, and thus it will be used extensively in the study reported here.

With the capability to run large-scale Monte Carlo simulations of realistic aeroservoelastic systems, the reliability of the closed-loop ASE system can be evaluated by calculating the corresponding probability of failure (POF). In order to reduce the POF, several methodologies can be proposed. The next section presents a brief review of statistical methods, such as sensitivity analysis, the Bayesian theorem and the auxiliary variable method. Using Monte Carlo simulations, these methods can be utilized to improve the robustness of the integrated aeroservoelastic system.

3.4 PROCEDURE OF UNCERTAINTY MITIGATION

3.4.1 *Parameter Prioritization with Statistical Sensitivity Analysis*

In order to reduce the probability of failure (POF) of the closed loop ASE system, a factor prioritization, often named sensitivity analysis, can be used to determine which factor, or set of factors, will lead to the greatest reduction in output uncertainty. A variety of approaches can be utilized to perform statistical sensitivity analysis [35-37]. In this chapter, the global sensitivity analysis of [35], which uses the variance as a measurement of uncertainty, is selected to evaluate the factor prioritization.

In variance-based global sensitivity analysis, variability in a model's output is assessed by examining contributions from each of the factors and their interaction. A detailed derivation can be found in [35] and [36]. Some key equations of the global sensitivity analysis are summarized below for clarity of presentation.

Consider a general mathematical representation of the output of a model of interest,

$$Y = f(\Lambda) \tag{3.10}$$

where

$$\Lambda=\left[\Lambda_1,...,\Lambda_i,...,\Lambda_k\right]^T \tag{3.11}$$

and Λ_i is the *i* th set of random variables of the model input.

Based on Sobol's approach [35], the sensitivity index for factor Λ_i can be computed as

$$\mathbb{S}_i = \frac{S_{pi}}{S_f} \tag{3.12}$$

where S_{pi} and S_f are the single-factor partial variances and function variance, respectively, and are calculated as

$$S_f = E\left(Y^2\right)-\left[E\left(Y\right)\right]^2 = \frac{1}{N}\sum_{m=1}^{N} f\left(\Lambda^m\right)^2 - f_0^2 \tag{3.13}$$

$$\begin{aligned} S_{pi} &= \mathrm{var}\left[E\left(Y\middle|\lambda_i\right)\right] \\ &= \frac{1}{N}\sum_{m=1}^{N} f\left(\left[\lambda_1^m,...,\lambda_i^m,...,\lambda_k^m\right]^T\right)\times f\left(\left[\tilde{\lambda}_1^m,...,\lambda_i^m,...,\tilde{\lambda}_k^m\right]^T\right)- f_0^2 \end{aligned} \tag{3.14}$$

where λ_i^m and $\tilde{\lambda}_i^m$ are the different samples of factor Λ_i, and

$$f_0 = \frac{1}{N}\sum_{m=1}^{N} f\left(\Lambda^m\right) \tag{3.15}$$

The random input parameters of a model can then be ranked by calculating the sensitivity index $\mathbb{S}_i$ in a prioritization setting to determine the parameter (or set of parameters) which, if the variance of the distribution is reduced, would result in the greatest expected reduction in output variability that is indicated by the largest value of $\mathbb{S}_i$.

3.4.2 *Bayesian Update and Risk Reduction*

Once the parameter (or the set of parameters) that will result in the greatest expected reduction in output variability is found by global sensitivity analysis, a redesign process can be enforced on this particular parameter to increase the reliability of the overall system. With limited number of measurements, either provided by the manufacturer or measured by the user, of the new designed parameter available, it is difficult to estimate the distribution coefficients such as standard deviation, with a high degree of confidence, and, thus, these coefficients are also treated as random variables.

To clarify the terms used in this context, the word "coefficient" is exclusively used in this chapter to represent the parameter that defines the shape of the distribution, such as mean value and variance, while "parameter" represent the physically input variable such as Young's modulus, thickness and cross section, etc.

Bayesian updating provides a useful statistical tool for reevaluating probability distributions and reducing uncertainty when new test data become available [38, 39]. In Bayesian updating, the coefficients that define the distribution shape in a particular probability model are themselves treated as random variables, with their own probability distributions. New modified and measured test data points are used to reduce the variance of the parameter distributions.

According to the Bayesian Theorem, the probability density function of the posterior distribution of the coefficients that define the distribution of a redesigned parameter is proportional to the product of a likelihood function and the prior distribution. The terms 'prior" and "posterior" are used here to denote the distributions before and after new information becomes available.

$$posterior \propto likelihood \times prior \tag{3.16}$$

For real-valued random variables with limited available measurements whose distributions are not known, the normal distribution as well as the distributions which can be converted to normal (for example, log-normal distribution) may be used for fitting the new measured data. It is also plausible to assume, based on the redesign and modification process, that the prior and posterior distributions have a known mean (parameter's nominal value) but unknown variance.

The likelihood function for a vector ***y*** of *n* iid (independent and identically distributed) new measurements of a redesigned parameter with known mean μ and unknown variance σ^2 is

$$L\left(y \mid \sigma^2\right) = \sigma^{-n} \exp\left(-\frac{n}{2\sigma^2} v\right) \tag{3.17}$$

where

$$v = \frac{1}{n}\sum_{i=1}^{n}\left(y_i - \mu\right)^2 \tag{3.18}$$

According to [40], with limited number of new measurements, the use of non-informative prior distribution can overcome the challenge of adding additional information by the assumption of prior distribution. Thus the non-informative prior distribution for the variance is selected and given by ([41], p.67)

$$p\left(\sigma^2\right) = \frac{1}{\sigma^2} \tag{3.19}$$

The posterior distribution of variance σ^2 then can be calculated as ([41], p.53)

$$p\left(\sigma^2 \mid y\right) \propto \left(\sigma^2\right)^{-\left(\frac{n}{2}+1\right)} \exp\left(-\frac{n}{2\sigma^2} v\right) \propto \text{Inv-}\chi^2\left(n, v\right) \tag{3.20}$$

Since the coefficients that define the parameter distribution are also treated as random variables. A traditional reliability analysis approach using Monte Carlo, FORM or SORM, requires coefficients that define the distribution shape, such as variance, to be sampled in the outer loop first, followed by the values of the system input parameter sampled in the inner loop within each sampled distribution coefficient. This double loop process becomes impractical

when the simulation is either complex or time consuming. The reader is referred to [40] and [42] for detailed presentation of the concept of adding an auxiliary variable to help replace the family of distributions with an equivalent single probability distribution. A brief review of the method is given in the following.

Let an auxiliary variable *r* be defined as

$$r = F_{\Lambda}\left(\lambda \mid \Sigma^2 = \sigma^2\right) = \int_{-\infty}^{\lambda} f_{\Lambda}\left(w \mid \Sigma^2 = \sigma^2\right) dw \tag{3.21}$$

where σ^2 is a sample of the distribution coefficient Σ^2 calculated from Equation (3.20) and *w* is a dummy variable used for integration. The function $F_{\Lambda}\left(\lambda \mid \Sigma^2 = \sigma^2\right)$ is the cumulative distribution function (CDF) of the system input variable Λ for a realization of σ^2. Since F_{Λ} range from 0 to 1, the auxiliary variable *r* follows a uniform distribution between 0 and 1. [40] also shows that the auxiliary variable $\Re$ is statistically independent of the coefficient of distribution, in this particular case Σ^2. The independency of *r* and Σ^2 allows the generation of samples of *r* and σ^2 simultaneously. After generating the sample of *r* and σ^2, respectively, one sample of Λ is obtained by

$$\lambda = F_{\Lambda}^{-1}\left(r \mid \sigma^2\right) \tag{3.22}$$

A distribution for Λ can be then obtained by repeating the above procedure to generate multiple samples of Λ. The fundamental difference between traditional reliability analysis and using the auxiliary variable approach is that the latter replaces the double loop simulation which generates samples of the physical distribution λ by first generating distribution coefficient σ^2, with generating λ and σ^2 simultaneously. The computational cost is, thus, reduced from $O\left(N^2\right)$ to $O(N)$, where *N* is the size of Monte Carlo process.

3.5 NUMERICAL AEROSERVOELASTIC RELIABILITY ANALYSIS

3.5.1 *The Nominal (Baseline) Case*

The Advanced Fighter Aircraft model (AFA) [43], representative of the complex nature and size of aeroservoelastic models of actual aircraft, is available in the open literature and is widely used for validation and comparison in the areas of loads, flutter, and aeroservoelastic control law design. The finite element model of the aircraft is shown in Fig. 3.2 and the aerodynamic model is shown in Fig. 3.3. The structural finite-element model includes 1200 nodes while the aerodynamic model has 300 DLM (Doublet Lattice Method) panels. The two models are coupled by interpolation using the infinite surface spline method.

The AFA model has five independent control surfaces. Two of them, the inboard and outboard elevons, are used for lateral flight dynamics in the test case studied here and are coupled with aeroservoelastic analysis. The case covered here thus, involves evaluation of aeroelastic lateral stability coupled with roll control.

The first 3 nominal natural frequencies and mode shapes plus the one rigid body roll with zero frequency of the fighter aircraft are shown in Fig. 3.4 to Fig. 3.7. Required by the formulating of the closed loop system function, two independent control modes are also calculated and shown in Fig. 3.8 and Fig. 3.9.

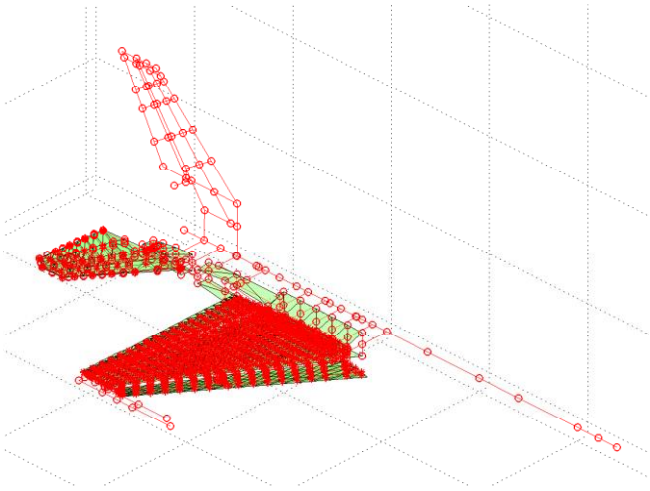

Figure 3.2. The Matlab Finite Element model of the AFA configuration

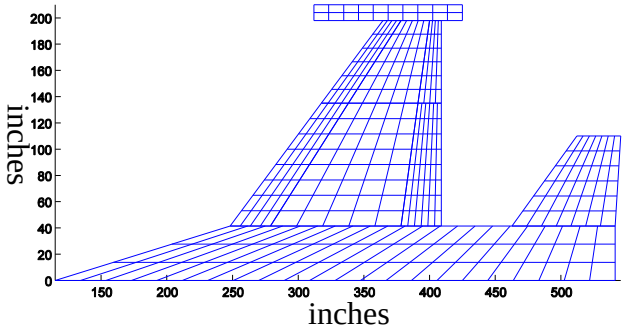

Figure 3.3. The Matlab Doublet Lattice Aerodynamic model of AFA

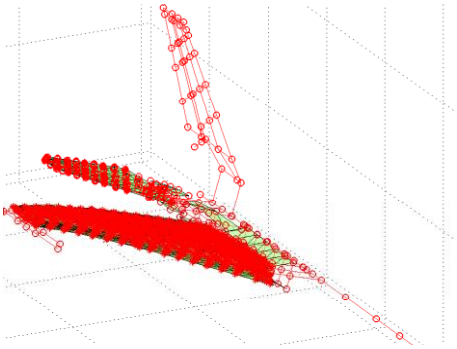

Figure 3.4. Rigid body roll mode

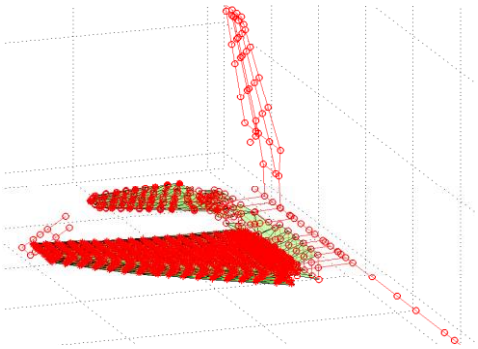

Figure 3.5. First structural mode

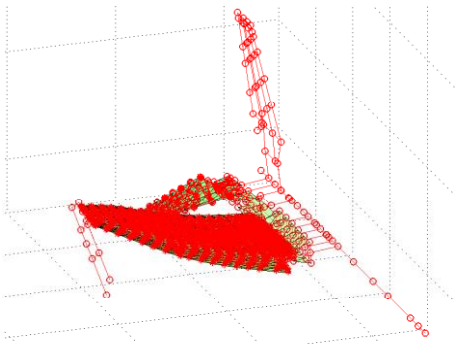

Figure 3.6. Second structural mode

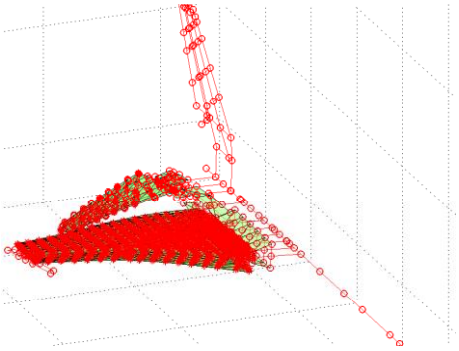

Figure 3.7. Third structural mode

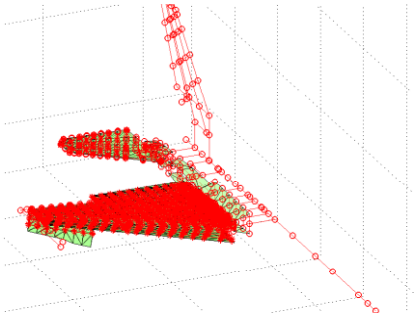

Figure 3.8. Control mode one

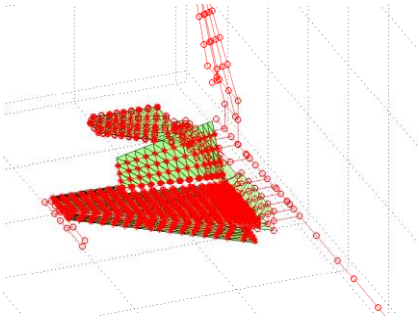

Figure 3.9. Control mode two

In the exploratory simulations reported here the aircraft is flown at a Mach number of 0.9 and the baseline (nominal) system stability is first evaluated by varying the flight altitude to seek a matched flutter solution. A detailed control system is provided in [43], to obtain a required aircraft roll rate performance subjected to control surface deflection limits and low frequency stability requirements. The nominal control block diagram for the AFA aircraft is shown in Fig. 3.10.

An eigenvalue sweep is used to find the stability of the baseline closed loop system, and the resulting root locus plot is shown in Fig. 3.11. Aeroservoelastic stability analysis has shown that flutter occurs at $q_F = 6.3429\,psi$ (43,732.76 Pa) with a frequency of 8.42 Hz. The ASE system is unstable at the baseline flight conditions point. A notch filter (taken from [43]) is added in order to solve the ASE instability problem by reducing the response around 52.9 rad/s (8.42 Hz). The

notch filter is located between the output of the sensor and the input of the control system, as shown in Fig. 3.12.

The Root Locus result of the baseline closed loop ASE system with notch filter is shown in Fig. 3.13 and indicates that no flutter occurs in the range of dynamic pressures covered.

A Nyquist diagram (Fig. 3.14) shown that the closed loop system has a minimum phase margin of 30 degree and a minimum gain margin of 9.26dB. A magnified view of the third quadrant of the Nyquist plot is shown on Fig. 3.14(b). Two branches cut the unit circle, one at a frequency of 7.5 Hz and the other at 12.8 Hz, corresponding to two potential flutter mechanisms. It also indicates a possible flutter mode switch when system's parameters change.

The robustness of the system, in general, can be evaluated using common control design robustness evaluation by studying its sensitivity function and complementary sensitivity function [44]. The singular values of these two functions with respect to frequency are shown in Fig. 3.15.

The singular value of sensitivity function (Fig. 3.15a) indicates that when process is subject to additive uncertainty ($P_p = P + \Delta$) or disturbance, the system may have stability problem around frequency 8.23Hz and 6.23Hz with its singular values equal to 17.4 (maximum) and 2.24 respectively.

Fig. 3.15b plots the singular value of the complementary sensitivity function of the closed loop AFA aeroservoelastic system. It can be seen, with noise or multiplicative uncertainties ($P_p = (1+\Delta)P$), at low frequencies, $T \approx 1$ and therefore the allowable multiplicative perturbations can be as large as the original process. The complementary sensitivity function reaches its maximum 17.1 at frequency 8.23 Hz which is approximately equal to the flutter frequency without notch filter. Hence, this gives the minimum allowable multiplicative process uncertainty less than 5% ($|\delta(i\omega)| < 1/|T(i\omega)|$). Finally, at high frequencies, $T \to 0$ and thus the

relative allowable bound can get very large. Other robustness requirements and characteristics with sensitivity function can be found in [44], pp. 115.

Since not all the system's parameter uncertainty can be categorized into either additive, disturbance, noise or multiplicative, with the help of general understanding of the robustness of the system, assess the ASE system robustness, determine the probability of control system design failure and what parameter's variation in the mathematical model of the system would have the largest effects on its stability. Beginning with a gradual approach, in which uncertainty in parameters representing different disciplines is systematically added up to study the resulting effect. The chapter later presents an approach by which uncertainty sources are covered by the Monte Carlo simulations, with global sensitivity analysis then used to identify those selected element uncertainties that are most important.

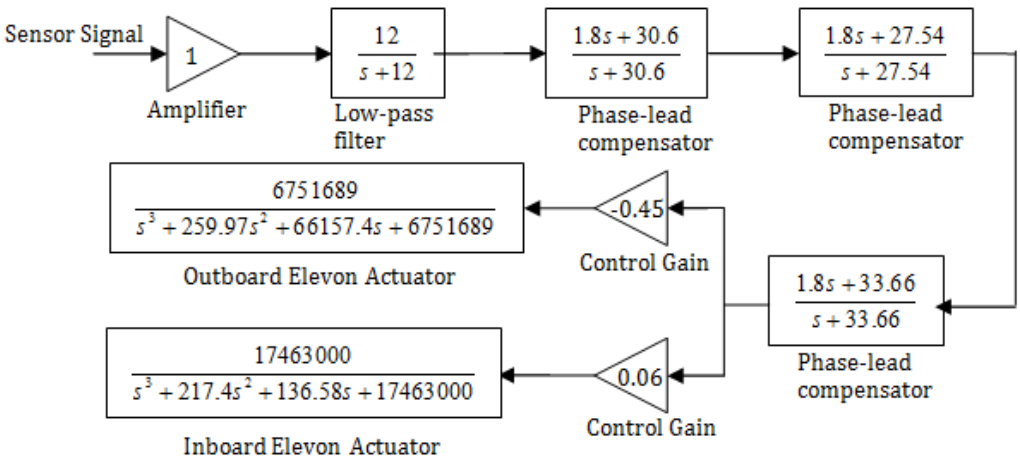

Figure 3.10. Nominal roll rate control block for AFA

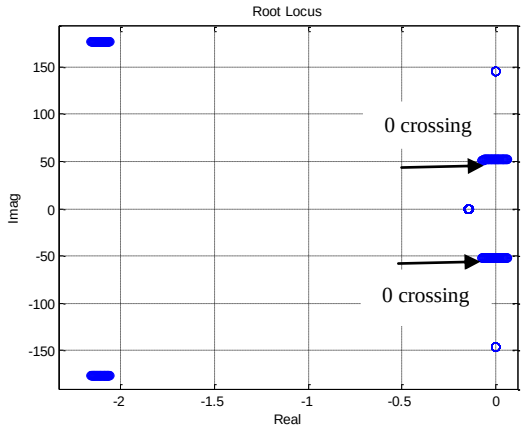

Figure 3.11. Root locus plot of the ASE system without notch filter

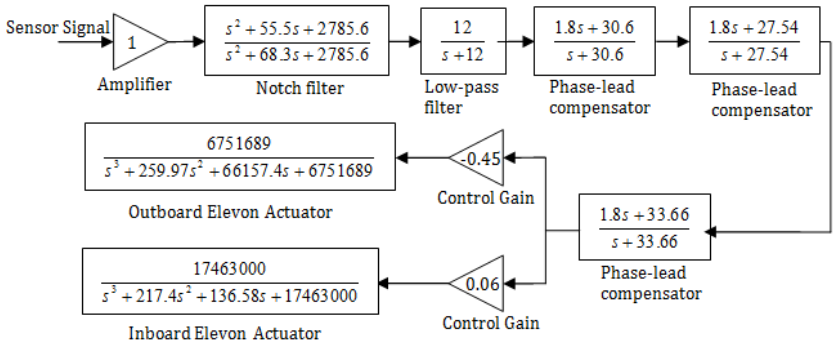

Figure 3.12. Roll rate control block with notch filter

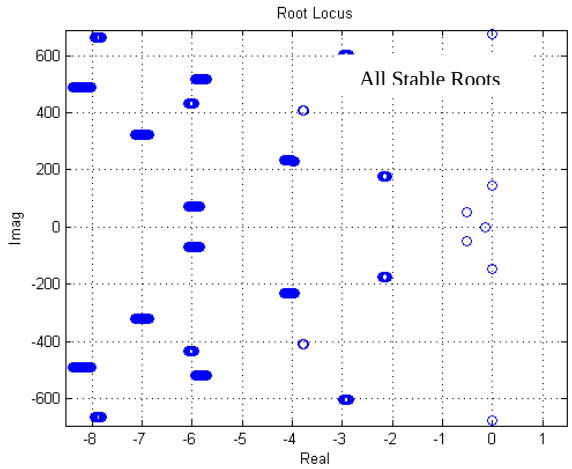

Figure 3.13. Root locus plot of the ASE system with notch filter

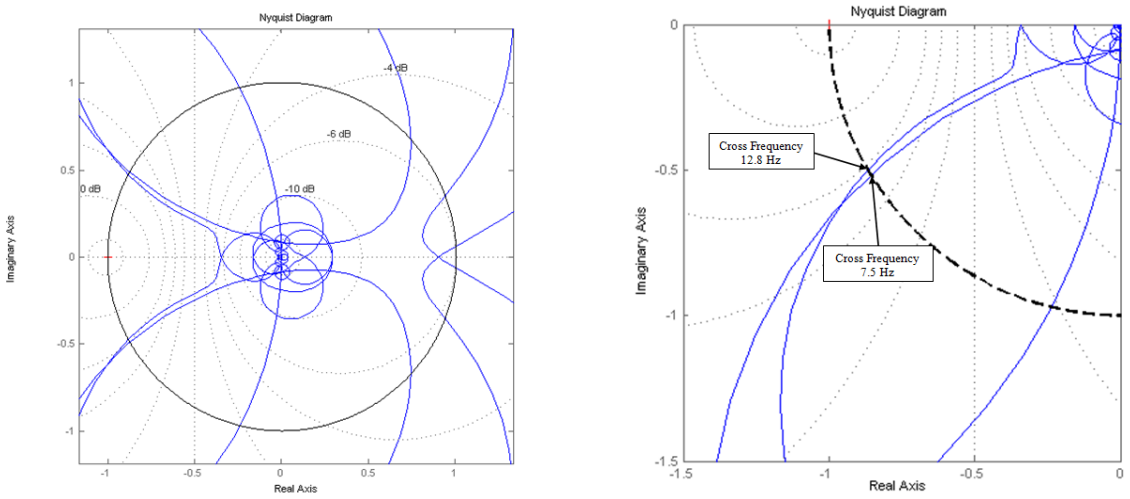

a) b)

Figure 3.14. Nyquist Plot of a) the closed loop AFA system b) third quadrant

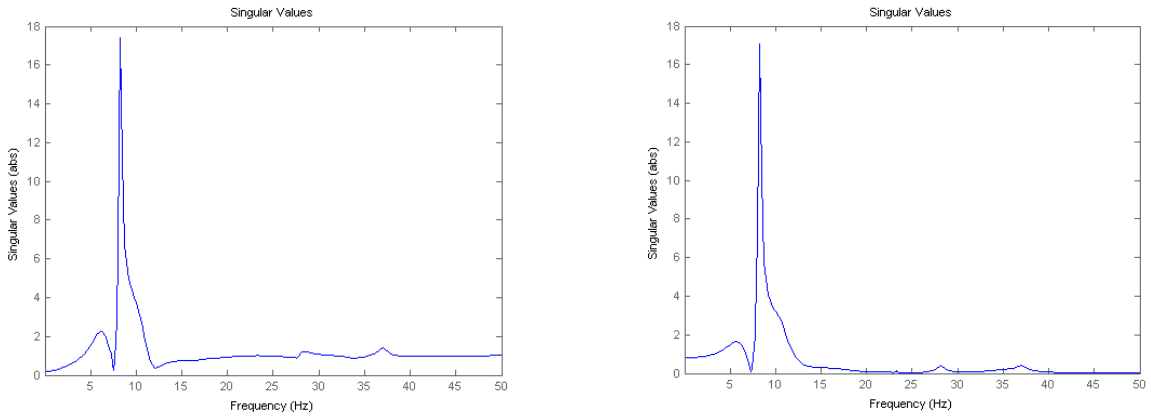

a) b)

Figure 3.15. Singular value of a) sensitivity function b) complimentary sensitivity function

Table 3.1. Nominal (baseline) values of actuator physical parameters

Parameter	Value	Parameter	Value
$A\ (in^2)$	4.71	f_c	0.0162
$V_t\ (in^3)$	20.63	L_c	0.0017
$M\ (slinch)$	31.31	$K_I * K_q\ (in^3/s/A)$	2642
$\beta\ (psi)$	481,626	$K_e * K_d\ (V/in)$	7.9
K_c	0.00108	$K_R\ (A/V)$	0.02303

3.5.2 *Uncertainty in the Actuator of the Outboard Elevon*

For an exploratory uncertainty study, a controls notch filter reliability analysis is performed first at Mach 0.9 and static pressure of 14.7 *psi* (sea level), with the uncertainty assigned to the physical parameters of the outboard elevon actuator. The nominal (baseline) values of the parameters of the outboard elevon actuator are listed in Table 3.1. The purpose of the reliability analysis is to evaluate the robustness of the notch filter and discover the probability and circumstances when the notch filter may become ineffective due to system's flutter frequency and associated flutter velocity moving out of the range of frequencies where the notch filter is effective.

Analysis has shown that no flutter will occur with the baseline notch filter at Mach 0.9 and a static pressure of 14.7 *psi*. Because of expected intricate dependency of notch filter effectiveness and flutter speeds on the variations in system parameters, and in order to avoid uncertainties introduced by approximate probabilistic analysis methods such as FORM and SORM techniques or other response surface based methods [45], the Monte Carlo simulation technique is used here. The motivation is to capture highly nonlinear system-parameter-to-output behavior such as critical aeroservoelastic mode switching and multi-modal probability distribution [6].

In order to increase computational efficiency, the approach selected here is as follows: Instead of calculating matched flutter velocities for each variation in parameters and studying the resulting flutter speed distributions, system stability with the notch filter is evaluated at the flight condition at which the system is unstable without a notch filter and at which the notch filter is effective. The approach to aeroservoelastic stability here is focused on stability or instability of aeroservoelastic poles at selected flight conditions [22,23,46,47,48]. When used for certification purposes, an aeroservoelastic poles-focused approach would cover, by simulations, flight

conditions throughout the flight envelope and on its boundaries, including flight conditions dictated by safety margins required to make sure that all aeroservoelastic poles are stable throughout the flight envelope and its boundaries [47,48].

The number of simulations for which the notch filter is effective and the system is stable are counted as well as the number for which the system with the notch filter is unstable. The reliability of the notch filter and the control system is measured by the probability of failure calculated as the number of unstable runs divided by the total number of simulation runs.

The Monte Carlo simulations are carried out using the following rules.

1. The bulk modulus of the hydraulic fluid is a thermodynamic quantity. Experience has shown that the bulk modulus for fluid could change significantly with operating temperature. Therefore, for an exploratory study, 10% and 30% of nominal value as standard deviation are modeled as distribution of bulk modulus.

2. Viscous friction between piston and cylinder and fluid leakage of the actuator can vary with manufacturing process and aircraft maintenance practices. However, with proper scheduled inspection, the variation of these parameters can be controlled within certain magnitude. Thus, the friction and leakage are assumed to have distributions with the nominal value as mean and 10% or 30% of mean value as standard deviation.

3. The convergence rate of the Monte Carlo analysis does not depend on the number of uncertain quantities or their variance [49]. The sample size of the estimation is calculated by Equation 38 below to ensure a less than 5% error of the system's probability of failure. Since the probability of failure of the system is not known in advance, a trial-and-error approach (Fig. 3.16) is used to determine the required number of MC simulations.

Table 3.2. Monte Carlo simulation results for the actuator-only uncertainty case

	Coefficient of Variation (COV)					
Actuator Bulk Modulus	0.3	0	0	0.1	0.2	0.3
Friction	0	0.3	0	0.1	0.2	0.3
Fluid Leakage	0	0	0.3	0.1	0.2	0.3
POF with Nominal Mode (>95% Confidence)	**0.0453**	**0.0***	**0.0***	**0.0***	**0.0073**	**0.0515**
POF with Fictitious Mass Mode (>95% Confidence)	**0.0516**	**0.0***	**0.0***	**0.0***	**0.0065**	**0.0493**

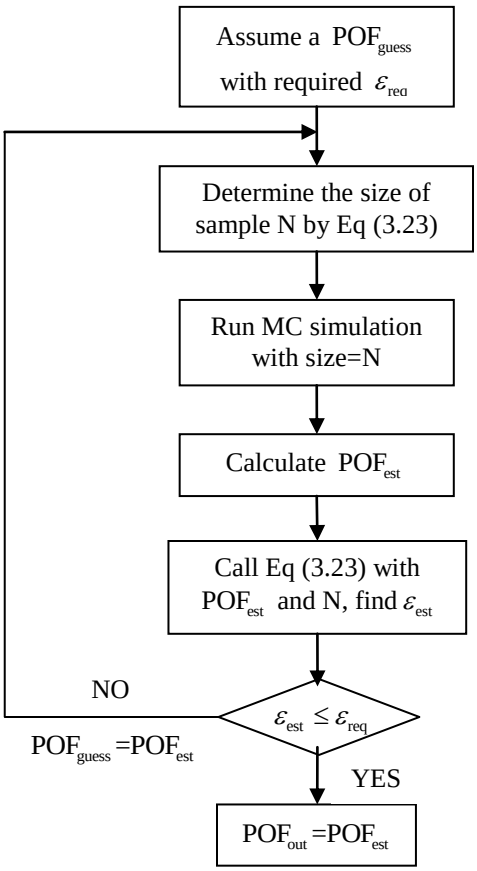

Figure 3.16. Flow chart of 'trial and error' procedure

4. The three actuator model random variables are assumed to be normally distributed but the distribution is truncated at ± 3 standard deviations to represent maintenance impact and rule out the unrealistic values. Other distributions can easily be handled by the capability described here.

The selected distribution is for demonstration of the capabilities of the uncertainty analysis system described here.

The simulation was performed using the University of Washington's William E. Boeing Department of Aeronautics and Astronautics 'Cerberus' high performance cluster with 12 cores for the parallel computing runs. It takes approximately 0.24 second for a single sample run. Table 3.2 shows the probability of failure calculated for the case of control actuator uncertainties with no other uncertainties.

Following ([45] p.135) the error (defined as the confidence interval of the estimated probability of failure into which the actual POF will fall with 95% chance) in the MC based probability of failure estimate can be found from

$$e\% = \sqrt{\frac{1-P_f}{N \times P_f}} \times 200\% \tag{3.23}$$

where

P_f is the probability of failure

N is the total number of Monte Carlo runs.

The inverse form of Equation (3.23) reveals that the number of runs required for MC simulation with pre-selected level of error increases dramatically with smaller POF. For the results of the exploratory Monte Carlo simulation process presented here the maximum number of runs is constrained to be up to 200,000 even though the new capability described here can be used to run millions of simulations on widely available clusters in practical clock-times. Sample runs in which no unstable poles are found, or cases when the number of samples is found to be too low to satisfy the designated confidence level in the case investigated are marked with an asterisk "*" in Table 3.2 and subsequent tables.

While a “variable modes” approach that requires solving the full order structural eigenvalue problem during each sampling can be used with the capability described here, a “fixed-modes” approach [46, 50] is used for the results presented here. In a “fixed-modes” approach a carefully-selected fixed set of modes is used and new modes do not need to be provided with every structural variation. The key to the success of a fixed modes approach in ASE simulations requiring repetitive analyses, whether in uncertainty analysis or design optimization, is the capacity of the mode shapes basis used to capture local effects in areas where design variables or uncertain system properties vary. The ASE simulations with actuator uncertainty are run again using, instead of a subset of low-frequency modes of the airframe a set of low frequency “fictitious mass” modes [51], generated to emphasize local action at the elevon to airframe actuator attachment region. Fictitious Mass modes, properly selected, are used as a set of fixed modes in all studies reported here. Results based on Fictitious Mass modes are also shown in Table 3.2.

Overall, the results clearly show that the notch filter in the example AFA case fails due to a combination of uncertainties in the actuator which can decrease the flutter velocity significantly. Similar reliability problems with notch filter performance as a cure to aeroelastic plant / flight control system coupling can be expected due to uncertainties in the structural and aerodynamic models of the aeroelastic plant.

3.5.3 *Uncertainty in the Actuator of the Outboard Elevon and the Structure*

Results of Monte Carlo simulation runs accounting for both structural and actuator variations are shown in Table 3.3. The uncertain structural parameters are selected to represent the mass of the elevon as well as thickness and Young’s modulus of its skins. Mass elements represent the total mass distribution in the elevon, and are modeled as lumped masses, based on the AFA model.

Each lumped mass has its own distribution, but it is correlated with nearby mass elements. Skin thickness and Skin panel's Young's Modulus are also modeled as uncertain and are correlated with nearby panel elements [6]. Statistical independence is assumed between upper and lower surface. The uncertain lumped mass, skin thickness and skin panel's Young's Modulus are all normally distributed with mean value equal to their corresponding nominal value and are truncated at ± 3 standard deviations to represent maintenance impact and rule out the unrealistic values.

The stiffness of the hinge attachment is also treated as a random variable. The ASE reliability capability presented here allows local updates of the structural FEM's mass and stiffness to account only for the uncertainties affecting the elements involved. With commercial FE codes used for massive simulations in an automated input/output mode the whole mass and stiffness matrices would be calculated with every change in the structure.

It is interesting to learn from the results (Table 3.3) of the cases studied here, which are by no means general and are limited to the configuration and assumptions used, that the probability of failure due to structural uncertainties with COVs up to 30% with the notch filter in the loop is relatively low. Once actuator uncertainties are introduced, the probability of failure became more significant.

3.5.4 *Added Unsteady Aerodynamic Uncertainty*

Both actuator and structural dynamic uncertainties can be evaluated by ground testing of the systems involved and can be reduced, although not eliminated, using proper updating of actuator and structural dynamic math models. Unsteady aerodynamic uncertainties are much more difficult to assess. Wind tunnel tests suffer from significant limitations on adequate scaling of the physical mechanisms involved as well the range of static and dynamic motions possible, not to

mention interference with walls and balance mounts. Accurate unsteady aerodynamic flight test data are even more difficult to obtain. It is not surprising, thus, that significant attention has been paid over the years to the issue of modeling and quantifying unsteady aerodynamic uncertainty for comprehensive aeroservoelastic uncertainty evaluation [2, 3, 7, 11, 13, 14, 15, 52, 53]. The ASE uncertainty evaluation capability developed and used for the work described here allows for a number of unsteady aerodynamic uncertainty modeling approaches, including uncertainty of the Aerodynamic Influence Coefficients (AICs), uncertainty in generalized aerodynamic influence coefficients (in a fixed-base modal approach), uncertainty in flight conditions, and additional approached that are beyond the scope of the present results.

To obtain exploratory results for the studies reported here, unsteady aerodynamic uncertainty is accounted for by making uncertain the elements of the $[P]$ matrices independently in the Roger approximation [48,54] of the unsteady generalized forces associated with the modal basis used:

$$\left[Q(jk)\right] \approx [P_0] + Jk[P_1] + (Jk)^2[P_2] + \frac{Jk}{Jk+\gamma_1}[P_3] + \frac{Jk}{Jk+\gamma_2}[P_4] + \ldots\ldots \tag{3.24}$$

Treating elements of the Roger $[P]$ matrices as uncertain variables allows separate accounting for uncertainty in the aerodynamic stiffness, damping, and inertia, as well as the contributions by aerodynamic time lag behavior. Uncertainty of the $[P]$ matrices also covered the combined effects of aerodynamic uncertainties in the theory and model geometry and discretizations used, the effect of interpolation uncertainty, and the uncertainties introduced by the conversion of unsteady aerodynamic loads from the frequency to the time domain (The Roger series fitting process). The uncertainty due to Mach number effects and variations is also included.

Table 3.4 presents the Monte Carlo simulation results with aerodynamic uncertainty only. The significant effects of aerodynamic stiffness and lag terms are evident in this case. Note the significant probability of failure of the AFA system stabilized by the notch filter to lag term uncertainty of only 0.002 COV. It is interesting that in this particular case the effect of uncertainty in aerodynamic damping terms is small. This, of course, should not be taken to be a general phenomenon. Unsteady aerodynamic damping can play a significant role in flutter mechanisms in many cases and uncertainty in its modeling would lead in such cases to uncertainty in the resultant ASE behavior.

Representative results of Monte Carlo ASE stability simulations covering uncertainty in all types of elements of the system, including structure, aerodynamics, and control system hardware, for the closed-loop ASE system with the notch filter at the reference flight conditions are shown in Table 3.5. All probability distribution functions for actuator and elevon structural properties are taken to be Gaussian and truncated within the $\pm 3\sigma$ range. Following [7], a uniform distribution is selected for the uncertain aerodynamic parameters. Generally, to emphasize it again, the ASE uncertainty capability developed and used for the studies reported here can accommodate any probability density function (PDF) for each of the uncertain variables in any particular uncertainty analysis case.

Not surprisingly, in the AFA cases studied here the major contributor to aeroservoelastic stability uncertainty is the unsteady aerodynamic uncertainty, although, the actuator uncertainty is important too.

Histograms for the unstable poles in all ASE stability runs and the associated frequencies are shown in Fig. 3.17 and Fig. 3.18. Fig. 3.17 shows the existence of more than one flutter mechanism. Uncertainties in the system studied here can lead to flutter mechanism switching,

similar to the results of the study presented in [6]. Depending on how system responses are defined, instability mechanism switching may be a challenge to commonly used FORM and SORM methods.

Although a relatively high probability of failure (POF) has been shown in the studies reported here when uncertainties in all involved disciplines interact and combine to lead the overall uncertainty, overall aeroservoelastic uncertainty in actual aircraft is lower, since uncertainty reduction via Ground Vibration Tests (fine tuning the structural dynamic models), wind tunnel tests (fine tuning aerodynamic models), and flight tests (reducing uncertainty in the integrated ASE model), as well as actuator tests, is used in any certification process. However, uncertainty would always exist, and would be affected by service life and maintenance processes. The simulation tools developed here can be used to analyze uncertainty due to all sources and in the presence of all test procedures and uncertainty reduction processes.

Table 3.3. Monte Carlo simulation results with structural and actuator variations

	Coefficient of Variation (COV)			
Actuator Bulk Modulus	0	0	0.2	0.3
Friction	0	0	0.2	0.3
Fluid Leakage	0	0	0.2	0.3
Mass	0.2	0.3	0.2	0.3
Young's Modulus	0.2	0.3	0.2	0.3
Thickness	0.2	0.3	0.2	0.3
Hinge Spring Stiffness	0.2	0.3	0.2	0.3
POF (>95% Confidence)	0.0*	3.8×10^{-4}	0.0067	0.0503

Table 3.4. Monte Carlo simulation results with unsteady aerodynamic uncertainty

	Coefficient of Variation (COV)				
Aerodynamic Stiffness $[P_0]$	0.1	0	0	0	0.1
Aerodynamic Damping $[P_1]$	0	0.1	0	0	0.1
Aerodynamic Mass $[P_2]$	0	0	0.1	0	0.1
$[P_3]$,$[P_4]$...$\left[P_{(N_\beta+2)}\right]$	0	0	0	0.002	0.001
POF (>95% Confidence)	**0.0128**	**0.0**	**0.0**	**0.0967**	**0.0356**

Table 3.5. Monte Carlo simulation results with variations of actuator, structural, and aerodynamic parameters.

	Coefficient of Variation (COV)
Aerodynamic Stiffness $[P_0]$	0.1
Aerodynamic Damping $[P_1]$	0.1
Aerodynamic Mass $[P_2]$	0.1
Aerodynamic Coefficient Matrices $[P_3],[P_4]...[P_{(N_\beta+2)}]$	0.001
Aileron Structure Young's Modulus (E)	0.3
Aileron Structure Skin Thickness	0.3
Aileron Structure Mass Distribution	0.3
Aileron Structure Hinge Spring Stiffness	0.3
Actuator Fluid Bulk Modulus	0.3
Actuator Fluid Friction	0.3
Actuator Fluid Leakage	0.3
POF (>95% Confidence)	**0.1138**

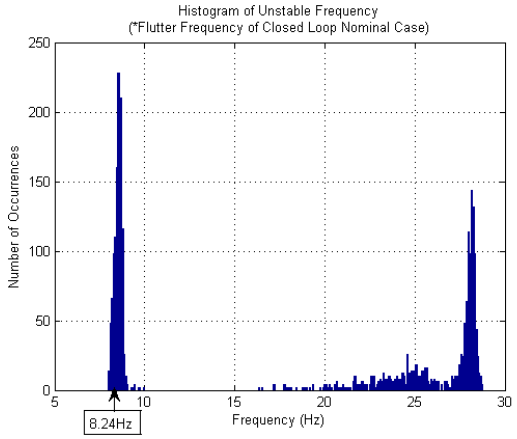

Figure 3.17. Histogram of unstable frequency

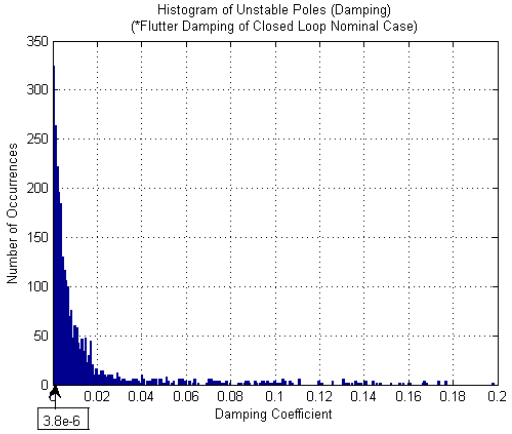

Figure 3.18. Histogram of unstable pole (damping coefficient)

3.6 APPLICATION OF UNCERTAINTY MITIGATION

Monte Carlo simulation has shown in the case investigated here that there is a considerable probability that the notch filter would fail to stabilize the AFA configuration in some cases due to actuator uncertainty, which in turn causes the failure of control law. Structural uncertainty and unsteady aerodynamic uncertainties aggravate the situation. Once sources of the uncertainty and their respective impacts are identified, as has been done by the Monte Carlo simulation, the system probability of failure of the system can be reduced in a number of ways. The structural dynamic uncertainty can be reduced with the help of ground vibration test (GVT) [55,56,57]. Unsteady aerodynamic uncertainty can be reduced by using high order computational methods, such as advanced CFD, as well as flight tests [58]. And, of course, more robust control laws may be developed ([59] for example) in consideration of possible tradeoffs between the level of conservatism in the controls design and the resulting cost, weight, and performance. This research, for an example of one reliability improvement approach, focuses on control actuator parameters to show how statistical sensitivity analysis together with Bayesian updating can be used to reduce failure risks.

3.6.1 *Parameter Prioritization*

Consider the closed loop aeroservoelastic stability problem with control actuator parameter uncertainty. The design parameters with uncertainty of the system are actuator bulk modulus, friction and fluid leakage with the nominal value of 481,626 *psi* (3,320,690,863.5 *Pa*), 0.0162 and 0.0017 respectively. As stated earlier, the three uncertain design parameters are normally distributed with COVs of 15% respectively. The output of the system, in global sensitivity analysis, is defined as the maximum real part of the system's eigenvalues.

As a summary, the random variables are defined as $\Lambda_1 \sim N(481626, 72243.9) psi$, $\Lambda_2 \sim N(0.0162, 0.00243)$ and $\Lambda_3 \sim N(0.0017, 2.55\times10^{-4})$ to represent the distributions of actuator's fluid bulk modulus, friction and fluid leakage. The output is denoted as

$$Y = f(\Lambda_1, \Lambda_2, \Lambda_3) = max\left(real\left\{eig\left[A_{SYS}(\Lambda_1, \Lambda_2, \Lambda_3)\right]\right\}\right) \tag{3.25}$$

where A_{SYS} is calculated using equation (2.11).

The global sensitivity index of the ASE system is calculated by Equation (3.12) with 50,000 runs of Monte Carlo simulation and is plotted in Fig. 3.19. The pie chart shows that the fluid bulk modulus Λ_1 dominates (92.7%) the variance of the output Y while the fluid leakage Λ_3 contributes to around 7% of the variance. The friction Λ_2 has almost no influence on the variation of output.

The global sensitivity analysis confirms the inference based on Table 3.2. However, the global sensitivity analysis identifies and quantitatively ranks the priority of the uncertain design parameters, while the reliability results above are generated by adding uncertainty contributions of different elements of the aeroservoelastic uncertainty "puzzle" by isolating and then combining them. For this particular example, the sensitivity analysis guides us to focus a redesign process that would increase reliability of the system on the fluid bulk modulus of the control actuator, as will be shown in the next section.

3.6.2 *Risk Reduction*

The risk reduction technique used here to increase reliability with improvement in actuator properties modeling can be broken into steps as follows:

Step 1. Find the most influential system parameter from statistical sensitivity analysis - In this particular case: the actuator bulk modulus β.

Step 2. A redesign process is used for the parameter identified in Step 1 and *n* iid new measurements of this redesigned parameter are either provided by the manufacturer of the new component or performed by the user (Fig. 3.20). A Bayesian update procedure is then used to estimate the distributions of the coefficients that define the distribution-shape of the redesigned parameter.

Step 3. The likelihood function is calculated by Equation (3.17). The posterior distribution of variance σ^2 can be calculated by Equation (3.20).

Step 4. Using the auxiliary variable method, *r* is randomly selected from a uniform distribution $\Re$ (0,1) and the variance σ^2 is randomly generated from the posterior distribution calculated in Step 3. For each pair of *r* and σ^2, use Equation (3.22) to calculate the sample β_i. Repeat until the required number of samples is satisfied.

Step 5. Run Monte Carlo simulation with samples generated from step 4 and calculate the probability of failure.

Fig. 3.21 shows the updated actuator fluid bulk modulus distribution compared to the original design. It can be observed that using the measurements in Fig. 3.20 the variance of the distribution is reduced. Since the nominal value (equals to the mean value of the distribution) is used in the notch filter design, it is expected that the probability of failure of the notch filter control law would be reduced with a reduction of variance. This, indeed, is shown by a new Monte Carlo simulation, Table 3.6. The updated actuator bulk modulus has reduced the POF of the system by about 75%.

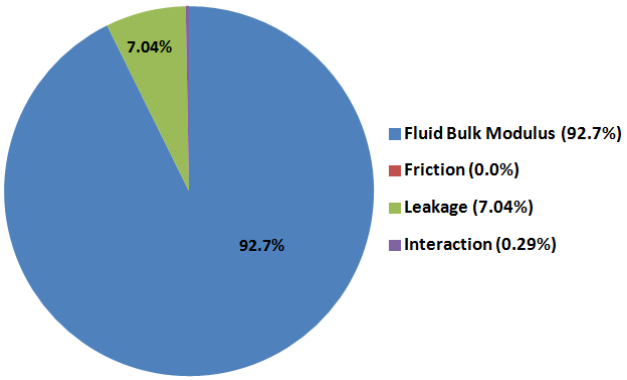

Figure 3.19. Results of the analysis of system sensitivity to servo-actuator parameters

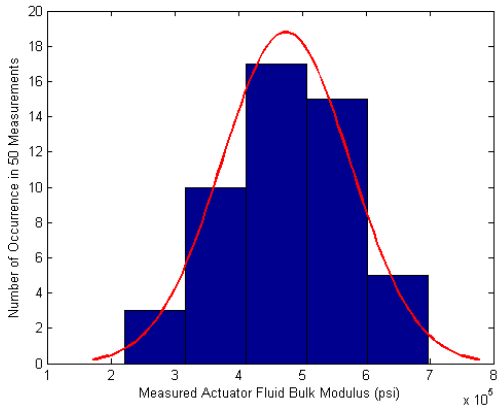

Figure 3.20. Fifty new measurements of actuator fluid bulk modulus

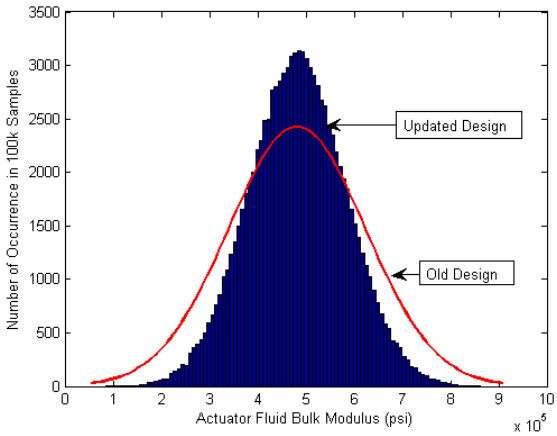

Figure 3.21. Comparison of original and updated actuator fluid bulk modulus

Table 3.6. POF of ASE stability between old and updated actuator design

	Coefficient of Variation (COV)	
Actuator Bulk Modulus	0.3	Updated by Eq (34)
Friction	0	0
Fluid Leakage	0	0
Probability of Failure	**0.0453**	**0.0111**

The computational cost for the parameter distribution modification plus the Monte Carlo simulations (100,000 sample size) is 6.71 hours, with 4.8 minutes on the cluster described above to generate the random variable using the auxiliary variable method. The use of global sensitivity analysis and Bayesian statistical tools provides a mechanism for identification of parameters of importance and the estimation of their distributions using directed new measurements during the design and certification process for reducing the level of uncertainty as well as the risk associated with the closed loop ASE system.

3.7 SUMMARY

An exploratory aeroelastic / aeroservoelastic reliability analysis using a mathematical model of a realistic aircraft configuration is performed by considering uncertainties of a control system actuator as well as structural dynamic and unsteady aerodynamic uncertainties. Detailed modeling of the electrohydraulic servo actuator made it possible to associate uncertainty with the actuator's physical parameters and gain insight about their effects. Aerodynamic uncertainty modeling allowed the evaluation of the effects of uncertainty in aerodynamic stiffness, damping, inertia, and lag contributions.

A roll rate control law design of a widely used AFA model with a notch filter is evaluated, accounting for the variability of hydraulic fluid bulk modulus, viscous friction, and fluid leakage of the outboard elevon actuator. Thus, assessment of the effects of uncertainty in each of the parameters representing physical detail of the dynamics of the actuator became possible.

Monte Carlo simulations have shown that in the particular case studied here, with the measures of uncertainty assumed for the parameters involved, there is a considerable probability that the notch filter would fail to stabilize the configuration in some cases due to actuator uncertainty, which in turn causes the failure of control law. Unsteady aerodynamic uncertainties

aggravate the situation. It becomes clear, therefore, that in addition to structural and aerodynamic uncertainties, uncertainties in the dynamics of key control system components and the uncertainty in the associated physical parameters must be considered in any aeroservoelastic reliability analysis together with already considered structural dynamics, aerodynamics, and flight conditions parameters.

To demonstrate a reliability improvement procedure and reduce the system's probability of failure, statistical global sensitivity analysis is performed with respect to actuator uncertainties to identify quantitatively the actuator parameter with the highest effect on overall system stability. The same parameter, the actuator fluid bulk modulus, was earlier identified by a gradual uncertainty parameter build-up approach in which the effects of various parameters, according to the disciplines and physical phenomena they represent, were added systematically. A redesign process is performed with new measurements added with a focus on the fluid bulk modulus, and by using Bayesian updating together with the auxiliary variable method, flutter failure reduction is achieved in a practical efficient way.

The example case studies investigated here are limited and the results are case dependent, though the case studied here is important because of its central role in validating aeroservoelastic codes and its capture of the issues raised by notch-filter design for aeroservoelastic purposes. What is general is that Aeroservoelastic stability depends on the structural, aerodynamic, flight, and control parameters that affect it in a complex and highly nonlinear way, and that the ASE uncertainty analysis simulation capability described here, which is developed to tackle general problems of aeroservoelastic uncertainty in real flight vehicles, demonstrates that with current ASE modeling methods as well as current and emerging computer hardware, a general Monte Carlo ASE simulation approach is becoming rapidly practical as a tool that would allow studies

of particular configurations as well as general theories and modeling techniques. New insights based on studies made possible by this new capability will be reported in future publications.

Chapter 4. ALTERNATIVE AERODYNAMIC UNCERTAINTY MODELING APPROACHES FOR FLUTTER RELIABILITY ANALYSIS§

4.1 OVERVIEW

A newly developed Monte Carlo simulation based computational capability for uncertain aeroelastic and aeroservoelastic systems is used to study flutter prediction statistics accounting for aerodynamic and structural uncertainties. In the aerodynamic area a physically based aerodynamic influence coefficients element by element correction uncertainty scheme is introduced and applied to the historical AGARD 445.6 wing test configurations at a sequence of transonic Mach numbers. The relative importance to the flutter velocity and frequency uncertainties of contribution of uncertainties associated with defined Mach number zones on the wing is ranked by using global sensitivity analysis. An alternative approach to aerodynamic uncertainty modeling, focusing on rational function approximation matrix uncertainties, allows examination of the relative impact of uncertainty in aerodynamic stiffness, damping, inertia, or lag terms. With the inclusion of structural uncertainties, the contributions of structural and aerodynamic variation to the uncertainty of system's outputs are compared and ranked.

4.2 INTRODUCTION

The importance of accounting for the variations in system characteristics and the uncertainty in aeroservoelastic design and certification has long been widely recognized [2]. Numerous basic-research papers, focused on simple, representative, problems of low computational costs have added to the understanding and insight in this area. Reliability and uncertainty analysis of full-scale aircraft, represented by industry-level mathematical models is more demanding and

---

§Content of this chapter is published in [120], [121]

difficult due to the modeling challenges and computational costs involved. Common practice in such cases, regarding the analysis required, has been to cover uncertainty and configuration variations by well-planned parametric studies that drive a large but manageable number of computer simulations [60,61]. The growing power in recent years of computer hardware and parallel-processing plus advancements in aeroservoelastic modeling and order reduction techniques have made comprehensive probabilistic approaches to the reliability / uncertainty evaluation of real aeroservoelastic systems more within reach. References [6,25,62] describe new aeroservoelastic simulation capabilities for full-scale systems of industry complexity and scale and for the associated reliability and uncertainty analyses that they make possible.

Significant work to date has been dedicated to the accounting in aeroelastic uncertainty analysis of uncertainty in the structural dynamic modeling of the system: stiffness and inertia variations due to manufacturing uncertainties, degradation during service, maintenance quality and procedures, damage and repair, etc. [6]. The difficulty in modeling structural damping and its possible variation with time and motion is still a challenge, although the effect depends on the type of flutter mechanisms present, whether explosive or mild (also known as hard and soft flutter, [63] p. 177-178). Similar difficulties are encountered when structural nonlinearities are present.

But structural dynamic uncertainty in the models can be reduced via ground vibration tests and static loads tests. Aerodynamic uncertainty, on the other side, and in particular unsteady aerodynamic uncertainty, more difficult to capture by analysis or mitigated by testing in the wind tunnel or in flight, is still extremely important and a major challenge. Recent efforts to harness Computational Fluid Dynamic (CFD) modeling technology or flight flutter test results for the task of evaluating unsteady aerodynamic uncertainties and their effects on aeroelastic instability

are described in [7,11,64-70]. Although major progress has been made on CFD-based unsteady aerodynamic order reduction, CFD based aerodynamic uncertainty quantification still faces major challenges due to the substantial computational efforts needed and difficulties of state of the art CFD modeling methods in capturing accurately unsteady flow behavior such as shock induced separation, shock - boundary layer interaction, and, in the case of separated flows, separation and vortex dynamics and burst. Modern CFD technology, while significantly ahead of the linear panel methods [71-79] that have been the backbone of aeroelastic analysis, design, and certification for years in its capability to capture nonlinear flow mechanisms (especially in the transonic regime), still encounters uncertainty due to its own limitations [49,80].

The results of attempts to adapt methods for robust design developed by the controls community have been reported in [13-14,15-17,52,53]. The work reported in this chapter, adopting the approach to aeroelastic and aeroservoelastic reliability reported in [6, 25, 81], is probabilistic and Monte Carlo simulation based.

A common practice in aeroelastic analysis and certification is to linearize the equations of motion relative to key steady state conditions. Linear unsteady aerodynamic panel methods have proven themselves to be reliable and quite accurate for aircraft in the low angle-of-attack (AOA) subsonic and supersonic flow regimes where theory based on linear potential aerodynamics works well. To account for deviations from linear unsteady aerodynamic theory, due to viscous effects or transonic compressibility effects, correction factors [65] are commonly used, based on wind tunnel loads measurements and CFD analysis, to fine-tune the predictions of the linear theory. When linearized CFD results are the basis for the unsteady aerodynamic math modeling, they are used to calculate matrices of generalized aerodynamic forces corresponding to selected

reduced bases (in the form of structural mode shapes). Uncertainty may be assigned to the elements of the generalized force matrices.

Whether unsteady aerodynamic loads in linear aeroelastic analysis are CFD-based, or panel-code based, corrected by CFD or by wind tunnel and flight tests, it is desirable from an engineering perspective, when uncertainties have to be accounted for, to assign uncertainties to entities of some clear physical meaning.

CFD-based unsteady aerodynamic modeling may address uncertainty in a physically-meaningful way by calculating unsteady aerodynamic loads for configurations with uncertain surface shapes. Uncertainty, in such a case, would cover 3D surface shape uncertainty plus uncertainty, possibly, in the capacity of any reduced structural bases to capture actual structural motion. Variation in Mach number, viscosity, turbulence models, and reduced frequency can be added – all representing physically-meaningful entities well. But the creation of uncertain CFD-based unsteady aerodynamic models this way is still prohibitive computationally, given current computing power, and even if all these effects are covered by the uncertain CFD analysis used, still uncertainty due to inherent deficiencies in CFD models that may miss important physical behavior would require careful attention.

Aerodynamic panel models are based on covering the surface of a configuration with small panels and establishing aerodynamic influence coefficients (AICs): Boundary conditions (upwash) and pressures (loads) relations between all pairs of panels. When uncertainties are assigned to elements of the AIC matrix, they can be considered “pure” aerodynamic uncertainties, since AICs are functions of the configuration, Mach number, and reduced frequency, but not the structural mode shapes that would be used for aeroelastic analysis.

On the other hand, unsteady aerodynamic effects never act alone in aeroelasticity since it is their integrated effect, weighted by structural motions, that determines aeroelastic behavior. Resulting generalized aerodynamic forces also have a certain physical meaning when the effects of their aerodynamic inertia, damping, stiffness, or lag terms are examined.

The goal of the present chapter is to contribute to uncertainty modeling of unsteady aerodynamic forces in the context of aeroelastic and aeroservoelastic uncertainty analysis by studying ways that would link uncertainties to mathematical entities of physical significance using current panel and CFD modeling methods. Assigning uncertainties to such physical entities may allow the engineer to have more insight regarding the relative importance, in reliability analysis, of key physical parameters, and the interactions of uncertainties in such physical parameters as they propagate through the aeroelastic system.

4.3 AICs BY LINEAR PANEL METHODS

Aerodynamic influence coefficients in an aerodynamic panel method establish relations between normal-wash on a panel and the corresponding loads on all other panels. In a typical lifting surface panel method, for example, a lifting surface is placed in its local (*x*,*y*) plane and divided into trapezoidal boxes. Each box has an area S_i, an upwash point $\left(x_{Di}, y_{Di}\right)$ and a load point $\left(x_{Li}, y_{Li}\right)$ (Fig. 4.1). A pressure differential (lower surface pressure minus upper surface pressure) $\Delta p\left(\varsigma,\eta\right)$ at point $\left(\varsigma,\eta\right)$ on the lifting surface is associated with upwash $w\left(x, y\right)$ at point $\left(x, y\right)$ according to:

$$\frac{w(x,y)}{U_\infty} = \frac{1}{8\pi} K\left(\frac{x-\varsigma}{b}, \frac{y-\eta}{b}, k, M_\infty\right) \frac{\Delta p(\varsigma,\eta)}{q_D} \tag{4.1}$$

where U_∞, q_D are the flight speed and dynamic pressure, respectively. $k = \dfrac{\omega b}{U_\infty}$ is the reduced frequency, b is a reference semi-chord, and M_∞ is the Mach number of the incoming flow.

The integral equation relating upwash to pressures over the lifting surface can be written as

$$w(x,y) = \frac{1}{4\pi\rho U_\infty} \iint_s K\left((x-\xi),(y-\eta)\right)\Delta p(\xi,\eta)\, d\xi d\eta \tag{4.2}$$

The kernel function of the integral equation $K\left(\dfrac{(x-\xi)}{b}, \dfrac{(y-\eta)}{b}, k, M_\infty\right)$ determines upwash/pressure relations for all pairs of panels over the lifting surface. Extension to configurations made of lifting surfaces in 3D and interacting with one another is straightforward.

Discretization of the integral equation in a panel method leads to a set of linear algebraic equations relating pressures at all boxes to upwash at all boxes in the matrix form:

$$\{w\} = [A]\{\Delta p\} \tag{4.3}$$

where $\{w\} = \{w_1 \quad w_2 \quad \ldots \quad w_n\}^T$ is the vector of upwash values at the upwash points of all boxes and $\{\Delta p\} = \{\Delta p_1 \quad \Delta p_2 \quad \ldots \quad \Delta p_n\}^T$ is the vector of pressures differences (lower surface minus upper surface at each box) located at the load point.

If a relationship between upwash at boxes at their upwash points and lift forces at boxes, L_i, is desired with the lift forces acting at the load point of each box,

$$\{\Delta p\} = [A]^{-1}\{w\} \tag{4.4}$$

Then the lift force can be written as

$$\{L\} = \begin{Bmatrix} L_1 \\ L_2 \\ \vdots \\ L_n \end{Bmatrix} = \begin{bmatrix} S_1 & & & \\ & S_2 & & \\ & & \ddots & \\ & & & S_n \end{bmatrix} \{\Delta p\} = \begin{bmatrix} S_1 & & & \\ & S_2 & & \\ & & \ddots & \\ & & & S_n \end{bmatrix} [A]^{-1}\{w\} \tag{4.5}$$

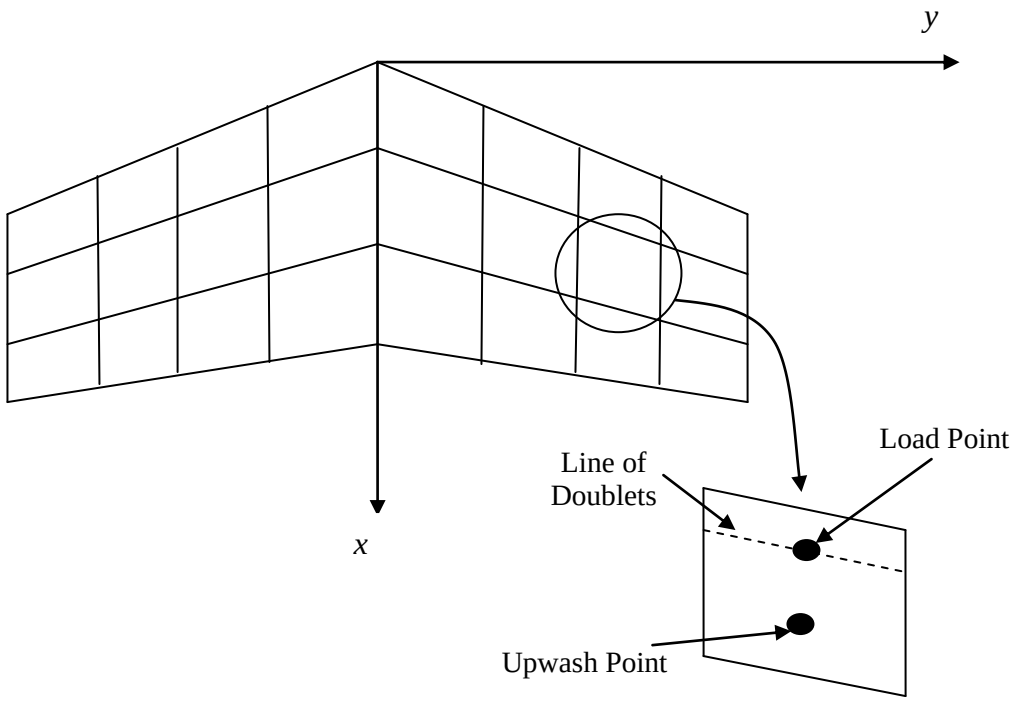

Figure 4.1. DLM mesh definition of upwash and load points

The entries S_i in Eq. 4.5 are the areas of the boxes. The formulation above assumes constant pressures over panels, but can be generalized, using integration matrices, to represent higher order approximations of downwash and pressure distributions over panels. A general Boundary Element approach to unsteady aerodynamic modeling would lead to normal-wash / load relations among all nodes used to define elements on the surface of the configuration.

Depending on the way selected, the aerodynamic influence coefficient (AICs) matrix may be defined by:

$$\{\Delta p\} = [AIC]\{w\} \tag{4.6}$$

Or, in non-dimensional form, by:

$$\left\{\frac{\Delta p}{q_D}\right\} = [AIC]\left\{\frac{w}{U_\infty}\right\} \tag{4.7}$$

Or, relating normal-wash to loads:

$$\{L\} = [AIC]\{w\} \tag{4.8}$$

which , in non-dimensional form, leads to:

$$\left\{\frac{L}{q_D S}\right\} = [AIC]\left\{\frac{w}{U_\infty}\right\} \tag{4.9}$$

For linear or linearized small-perturbation flow the AICs are purely aerodynamic, dependent on flight conditions and on configuration reference shape but not its small-perturbation motions.

$$[AIC] = [AIC(M_\infty, k, \mathrm{Re}, ReferenceShape)] \tag{4.10}$$

For the whole configuration at the same angle of attack (adopting Eq. 4.7)

$$\{\Delta c_p\} = \left\{\frac{\Delta p}{q_D}\right\} = [AIC]\left\{\{\alpha_0\} + \begin{Bmatrix}1\\ \vdots \\ 1\end{Bmatrix}\alpha\right\} \tag{4.11}$$

Where the $\{\alpha_0\}$ vector contains local geometric angles of attack of different panels when the AOA of the configuration, α, is zero. Each column *j* of the AIC matrix is, thus, the pressure distributions due to unit total AOA at a box *j* with total AOAs at all other boxes being zero. For a unit total AOA at box *j* and zero total AOA at all other boxes the pressure distribution over the wing is

$$\{\Delta c_p\}_j = \left\{\frac{\Delta p}{q_D}\right\}_j = \{\text{column } j \text{ of [AIC]}\} \tag{4.12}$$

An examination of AICs at given reduced frequency, Mach, and Reynolds (Re) numbers can be insightful regarding the way different aerodynamic boxes "communicate" with each other. In supersonic flow, for example, aerodynamic boxes affect only the boxes within their Mach cones ([82], for example). Uncertainty in flight Mach number and in local Mach numbers can determine whether boxes on the boundary of a certain Mach cone may move in or out of it, thus affecting or not affecting other boxes or being or not being affected by other boxes.

In addition to the spatial inter-connections of AIC elements and the way each single box is related to all others, the frequency dependency of AICs can provide important insight. In general AICs are transcendental functions of the reduced frequency. But when rational function approximations are used to convert unsteady aerodynamic AICs or generalized forces from the frequency to the Laplace and time domains (in the form of Roger, [54], and Minimum State approximations, [83] and [84], for example), their distinct aerodynamic stiffness, damping, inertia, and time lag contributions can be identified and the effects of uncertainties in each of those can be studied.

In the case of using a Roger Approximation to express the dependency of generalized aerodynamic forces (or full AICs) on reduced frequency:

$$[Q] \approx [P_0] + Jk[P_1] + (Jk)^2[P_2] + \frac{Jk}{Jk+\gamma_1}[P_3] + \frac{Jk}{Jk+\gamma_2}[P_4] + ... \tag{4.13}$$

Finding the relative contributions to aeroelastic uncertainty by the different $[P_l]$ matrices may provide useful insights regarding the relative effects of aerodynamic inertia, damping, stiffness, and time-lag on both the physical behavior and the quality of the fitting expressed by Eq. 4.13. Different flutter mechanisms may be sensitive in different ways to uncertainties in aerodynamic inertia, damping, stiffness, and lag, as aeroservoelastic uncertainty studies of such effects using fixed-base generalized aerodynamic matrices have shown in [25]. A particular flutter mechanism may be more sensitive to aerodynamic damping or aerodynamic stiffness or aerodynamic lag. Insight regarding such sensitivity can guide unsteady aerodynamic modeling and related uncertainty analysis.

4.4 ACCOUNTING FOR THE AERODYNAMIC UNCERTAINTY

The availability of AICs obtained directly from CFD after linearization – another way of obtaining AICs in cases where linear panel based AICs do not work well – offers an opportunity for evaluation of modeling errors and uncertainty at the local, panel by panel mesh.

Considering the uncertainty of numerical simulation only (both methods used and numerical capture of the geometry studied), one possibility is to calculate CFD-based AICs using different CFD codes and different CFD models (mesh size, turbulence models, etc.) and to use differences in the AICs between different simulations to guide assignment of uncertainty to the AICs relating different mesh points or aerodynamic boxes. Such comparison of box to box aerodynamic communication by different mathematical models can be expected to identify areas on the configurations to which AICs are more sensitive regarding simulation accuracy: regions of large pressure gradients, separation, boundaries between subsonic and supersonic flows, etc.

For the exploratory studies reported here the field-panel approach to AIC generation based on CFD simulations has been used in its ZTRAN implementation [85], which can generate CFD-based AICs on an aerodynamic panel method mesh. ZTRAN is based on small disturbance transonic flow theory and full reference steady state CFD solutions and it leads to AICs that capture transonic effects such as shocks. More advanced CFD-based simulation capabilities can be used to generate AICs. Conceivably, similar to the many simulations using different CFD capabilities for the same configurations in aerodynamic prediction workshops [66-68], enough different CFD simulations of the unsteady aerodynamic load distributions as well as linear predictions on a configuration of interest can be produced to guide the assignment of uncertainty to the various elements of the resulting AICs.

Comparison of ZTRAN AICs calculated by using a number of CFD models as bases and assigning uncertainties based on these AICs can account the uncertainties due to different CFD modeling techniques, discretization and convergence criteria, etc. Similarly, comparing the CFD based AICs with AICs created by a compressible subsonic method such as the Doublet Lattice Method (DLM, [71-72]), Doublet Point Method [76-77] and ZAERO [78-79] can teach us where differences between potential flow based theory and theory based on nonlinear CFD are more pronounced and guide uncertainty modeling of the related AICs.

One possible approach to the AICs uncertainty problem, when wind tunnel or flight test results, are available, is to select from among the unsteady aerodynamic simulations used (including the case where AIC matrices had been already corrected by steady or unsteady aerodynamic information using correction factors, [65]) a simulation that leads to predictions that are close to the measured flutter results. This unsteady aerodynamic simulation then becomes the baseline simulation used as a reference against which all other aerodynamic predictions would be measured. A column to column comparison can now be made between the baseline AICs and all the other AICs (on the same panel model) at a reduced frequency close to the predicted baseline flutter reduced frequency calculated by different CFD simulations and/or linear panel methods.

Eq (4.14) defines ratios of elements of the AIC matrices to the baseline AIC simulation using MATLAB notation,

$$\left[\varepsilon_n(:, j)\right] = \left[\mathrm{AIC}_n(:, j)\right] ./ \left[\mathrm{AIC}_{\mathrm{base}}(:, j)\right] \tag{4.14}$$

where $\left[\mathrm{AIC}_n(:, j)\right]$ is the jth column of AIC that calculated by nth method / model

$\left[\mathrm{AIC}_{\mathrm{base}}(:, j)\right]$ is the jth column of AIC that calculated by the baseline method / model

./ represent column element by element division.

For each element *i* in the *j*th column comparison, uncertainties can be established by comparison of the ratios $\left[\varepsilon_1(i,j)\right],\left[\varepsilon_2(i,j)\right],\ldots,\left[\varepsilon_n(i,j)\right]$. Development of a probability distribution, denoted as $\left[\tilde{\varepsilon}(i,j)\right]$, can be then guided by using the mean and variance of the set $\left[\varepsilon_1(i,j)\right],\left[\varepsilon_2(i,j)\right],\ldots,\left[\varepsilon_n(i,j)\right]$. A uniform distribution of $\left[\tilde{\varepsilon}(i,j)\right]$, converting the mean and variance to the upper and lower bounds, would represent a conservative approach to aeroelastic uncertainty analysis. When an element i,j of the $\left[\mathrm{AIC}_{\mathrm{base}}\right]$ matrix is close to zero an additional check is performed on the corresponding i,j element in the $\left[\mathrm{AIC}_n\right]$ matrix. If the i,j element in both $\left[\mathrm{AIC}_{\mathrm{base}}\right]$ and $\left[\mathrm{AIC}_n\right]$ matrices are close to zero, no uncertainty is associated with this element and $\left[\varepsilon_n(i,j)\right]=1$.

If element i,j is very close to zero in the baseline AICs but not in some of the AIC matrices obtained by other aerodynamic simulations, a distribution for that element is determined by the i,j elements directly or by ratios with respect to the mean of the sample of i,j elements.

In the absence of test results the baseline AIC matrix can be selected to be the mean of all AIC matrices or an AIC matrix produced by experience-based analysis processes used by an organization for flutter analysis. If multiple flutter mechanisms are involved, added samples of AICs created by different simulation models at a number of reduced frequencies close to the predicted flutter reduced frequencies can be used.

Physically, note that uncertainty assigned to a whole column reflects, depending on the Mach number at the associated box, accuracy regarding the way that motion of that box is aerodynamically "communicated" to all other boxes in the form of pressures or forces at those boxes. Uncertainty assigned to a whole row accounts for the accuracy in modeling of the

capacity, in the math model, of the associated box to aerodynamically “respond” accurately to motions of all other boxes. The assignment of uncertainty to different elements of the AIC matrix described above is based on physical interpretation of the differences between different CFD-predicted AICs or panel code-predicted and CFD-predicted AICs on the same aerodynamic box mesh. Availability of steady and unsteady aerodynamic loads distributions from wind tunnel or flight tests would enrich the sample space of AICs used in aeroelastic uncertainty analysis. Also note, that the distributions of AIC elements from different CFD simulations can be taken as starting points and guides for the distributions that would actually be used in the ASE simulations, where those AIC element uncertainty distributions may have shifted means and larger spreads relative to the distributions from the CFD samples.

Schematically, the Monte Carlo simulations of flutter speed and frequency uncertainty (if flutter prediction is the focus on the aeroelastic uncertainty analysis) proceed as follows:

For any given Mach number, carry out flutter analysis using frequency domain tabulated AIC matrices and corresponding generalized aerodynamic matrices based on as rich a selection of different linear-panel and linearized CFD-based unsteady aerodynamic simulations and aerodynamic tests as possible. Select a tabulated reduced frequency close to the flutter reduced frequency. If flutter test results are available, select the unsteady aerodynamic AICs that lead to flutter predictions close to the measured result and make them the baseline AICs. Otherwise, select the baseline AICs based on engineering experience.

Next, for the reduced frequency selected, sweep over all AIC matrices available, find the relative differences between different AIC prediction methods column by column and assign uncertainty Probability Distribution Functions (PDFs) for both real and imaginary parts of the elements in this column of the AIC matrix. If flutter mechanisms involving more than one

reduced frequency are present, add samples of the AIC matrices at those reduced frequencies to the AIC sample based on which the AIC PDFS are created.

Using the AIC PDFs and the baseline AICs tabulated matrices, now proceed to run Monte Carlo flutter-solution simulations, accounting for unsteady aerodynamic uncertainty in both real and imaginary parts (with added structural uncertainties, when both aerodynamic and structural uncertainty is accounted for). Use the resulting samples of flutter speed and flutter frequency to study uncertainty in flutter prediction.

Results produced by the proposed methodology will be presented in the next section for one of the most well known transonic aeroelastic systems – the AGARD 445.6 wing [86, 87], for which wind tunnel flutter test results are available.

4.5 NUMERICAL EXAMPLE

The AGARD 445.6 weakened wing [86-87] is considered here for subsonic and transonic flutter simulation. The structural finite element method (FEM) model and aerodynamic panel model are shown in Fig. 4.2 and 4.3. The structure FEM of the wing is made of composite plate elements with varied thickness. The FE model has 200 elements and the first five structural mode shapes (Fig. 4.4-4.8) are used in the flutter analysis.

The aerodynamic model has 100 panels. A reference chord of 22.0 inches is used with a 30 inches semi-span length. Unsteady aerodynamic analysis is performed at reduced frequencies ranging from 0.0 to 0.8. Three Mach numbers, 0.678, 0.901 and 0.954, are selected for numerical studies. Linear subsonic panel methods cannot capture the physics of the flow deep into the transonic regime with geometries that lead to transonic effects that cannot be neglected. CFD based panel-field simulations are used here to capture transonic effects because of their built-in

capability to convert CFD results to aerodynamic AICs on a panel grid. More advanced CFD methods would, of course, capture more of the flow physics involved.

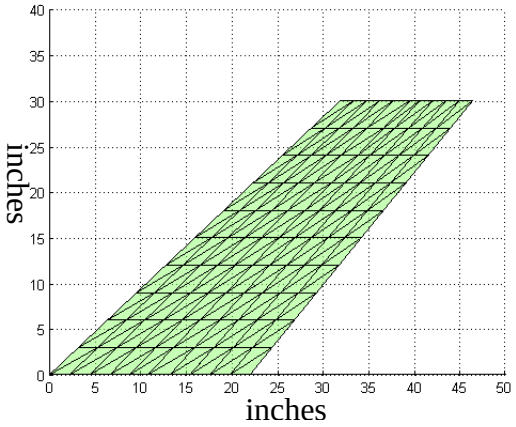

Figure 4.2. Structure FEM model

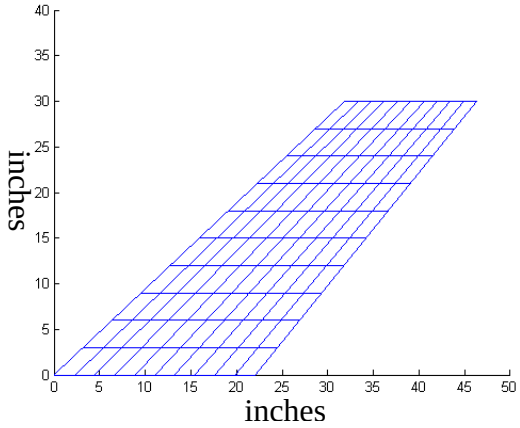

Figure 4.3. Aerodynamic panel model

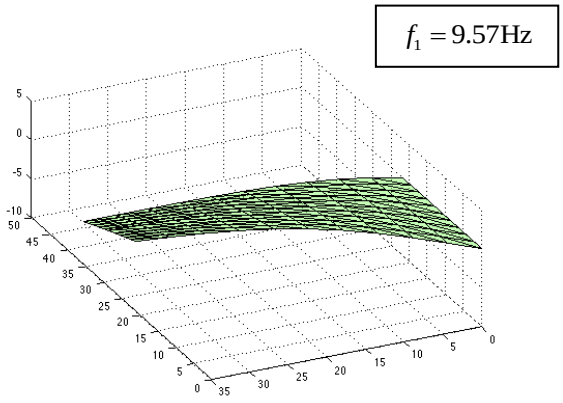

Figure 4.4. Structure mode 1

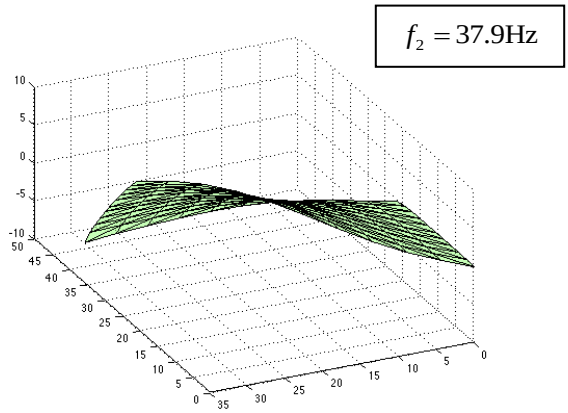

Figure 4.5. Structure mode 2

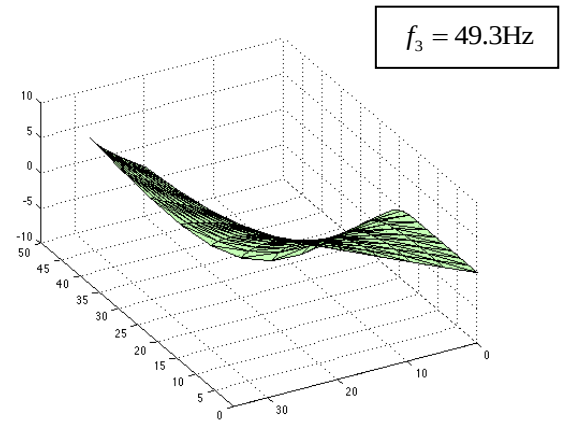

Figure 4.6. Structure mode 3

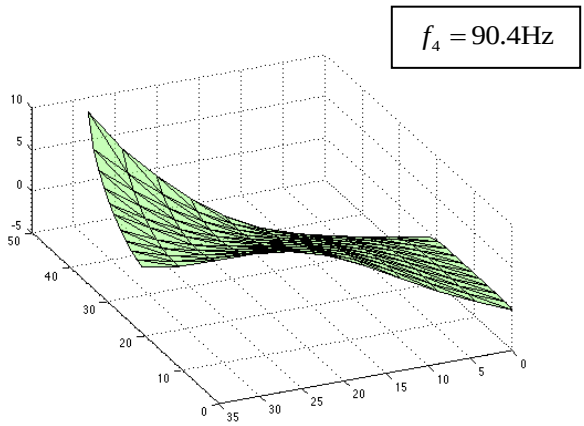

Figure 4.7. Structure mode 4

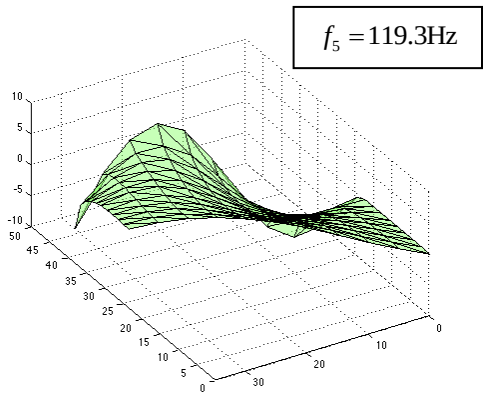

Figure 4.8. Structure mode 5

4.5.1 *Nominal Flutter Analysis*

A flutter analysis is performed first with the baseline model without uncertainties using a University of Washington developed aeroservoelastic simulation capability [25]. Four unsteady aerodynamic calculation techniques are used to calculate the flutter velocity index

$$U\Big/\left(b\omega_\alpha\sqrt{\tau}\right) \tag{4.15}$$

and flutter frequency ratio ω/ω_α. Where $\sqrt{\tau} = m/\rho v$ is the mass fraction, m is the mass of wing, ρ is the density of the fluid, v is the volume of the wing, b is the half chord at the wing root and ω_α is the nature frequency of the first uncoupled torsional mode.

The Doublet Lattice Method (DLM, [71-73]) and ZAERO (ZONA 6, [78, 79, 88]) are linear panel based unsteady aerodynamic codes which solve the small disturbance potential equation, while ZTRAN [85] is an unsteady field–panel method that solves the linearized transonic small disturbance equations using steady background flow from the high-fidelity CFD simulations. Two CFD steady states solutions are used for ZTRAN: CFL3D, a NASA code that solves the Navier- Stokes equations [89] and ZEUS [90-91] that solves the Euler equations with interactive boundary layer simulation. Those are denoted in the following: ZTRAN-CFL3D and ZTRAN-

ZEUS. As stated in the previous section, all the four methods used here can generate AIC matrices on the same aerodynamic panel mesh.

The nominal flutter index and flutter frequency ratio are calculated first without consideration of uncertainty. The numerical results are shown in Table 4.1 together with the experimental results. Figures 4.9-4.11 are the V-g and V-ω plots for the nominal cases using a DLM unsteady aerodynamic model. They offer insight about the type and severity of the flutter mechanisms. It can be seen from the V-g plot that at M = 0.678 (Fig. 4.9) the flutter mechanism is more moderate than those at M=0.901 (Fig. 4.10) and 0.954 (Fig. 4.11). The flutter behavior at M=0.901 and 0.954 are relatively mild and that may make the flutter index / velocity more sensitive to model uncertainty. Figures 4.12 and 4.13 show correlation of the flutter predictions by the various methods used here with experimental results and differences between the various predictions. Recent papers on the subject report thorough correlation studies between analysis and tests using different aerodynamic simulation methods, [87] and [92]. The following brief discussion of AGARD 445.6 flutter predictions results by the methods used here is aimed at highlighting major features of the flutter behavior of this system that would guide and help interpret the uncertainty analysis presented here.

Table 4.1. Summary of flutter solutions with difference unsteady aerodynamic models

	M=0.678		M=0.901		M=0.954	
Aerodynamic Model	$\frac{U}{b\omega_\alpha\sqrt{\tau}}$	$\frac{\omega}{\omega_\alpha}$	$\frac{U}{b\omega_\alpha\sqrt{\tau}}$	$\frac{\omega}{\omega_\alpha}$	$\frac{U}{b\omega_\alpha\sqrt{\tau}}$	$\frac{\omega}{\omega_\alpha}$
Experiment	0.4174	0.4722	0.3700	0.4225	0.3059	0.3807
Doublet Lattice Method (DLM)	0.4305	0.5516	0.3693	0.4408	0.3357	0.3989
ZONA 6	0.4279	0.5494	0.3655	0.4374	0.3317	0.3956
ZTRAN - CFL3D	0.4251	0.5468	0.3535	0.4252	0.2942	0.3628
ZTRAN - ZEUS	0.4254	0.5472	0.3549	0.4265	0.2972	0.3656

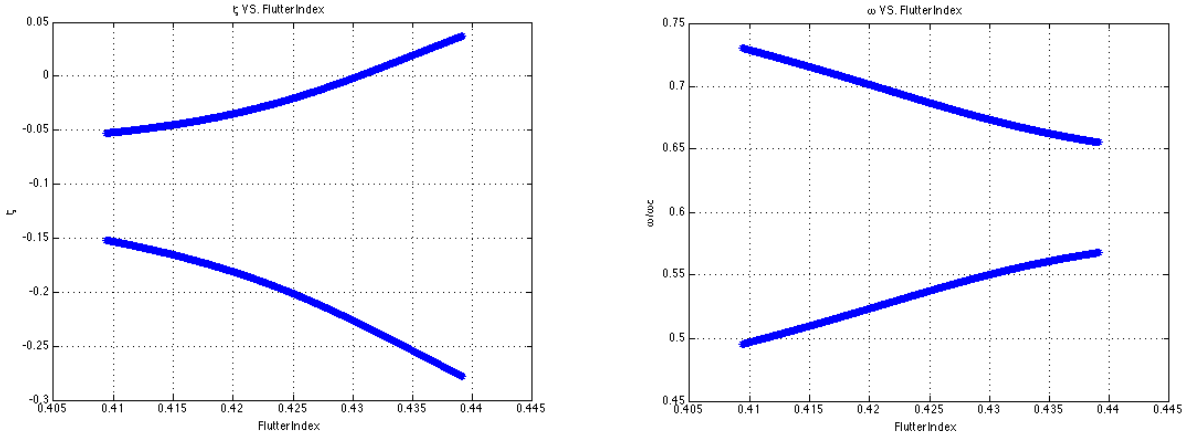

Figure 4.9. v-g and v-ω plots at M = 0.567

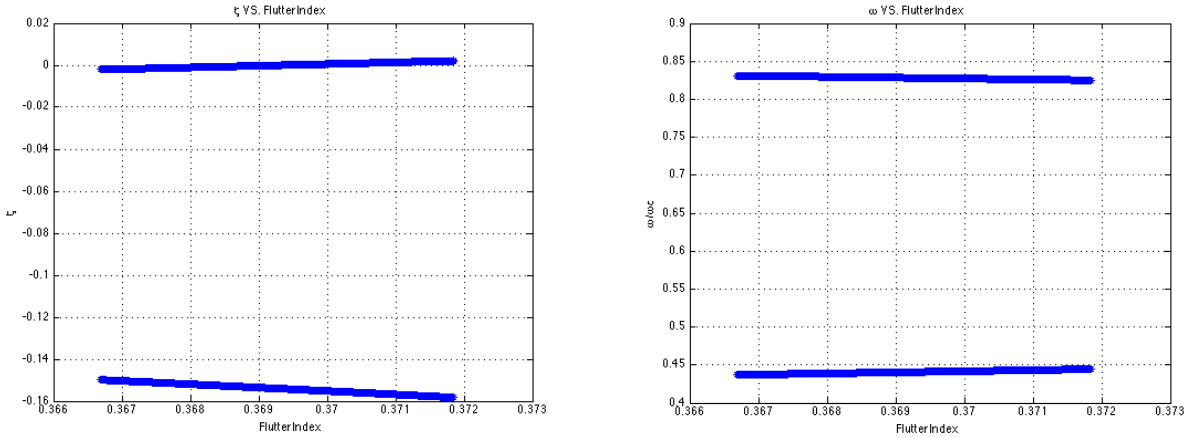

Figure 4.10. v-g and v-ω plots at M = 0.901

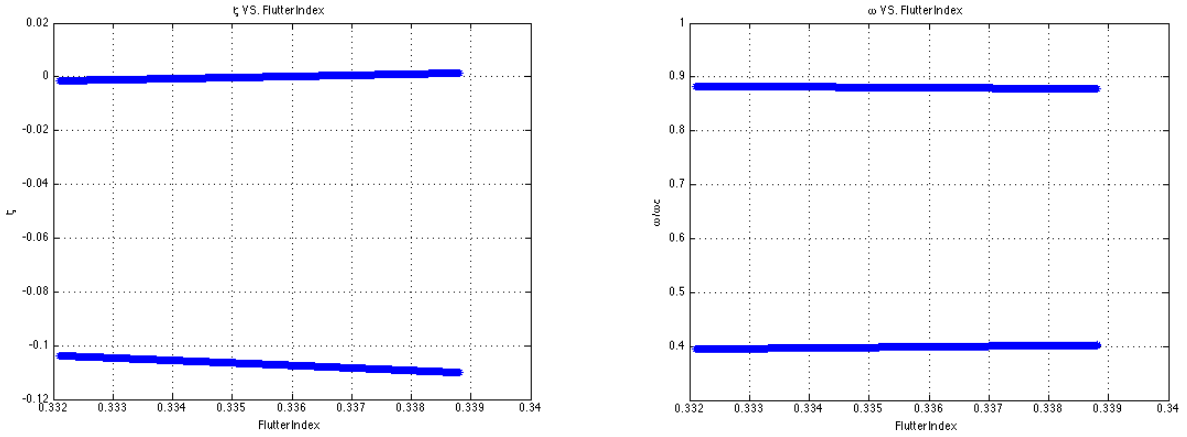

Figure 4.11. v-g and v-ω plots at M = 0.954

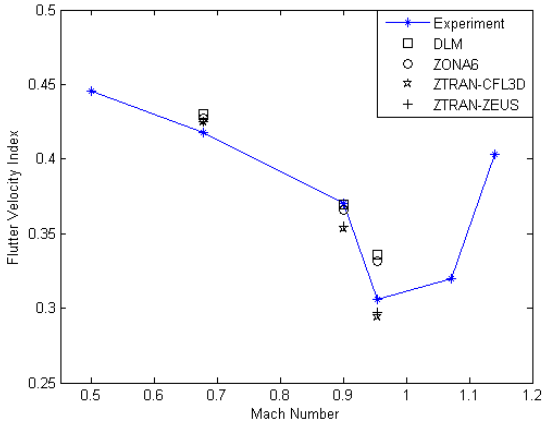

Figure 4.12. Mach number vs. flutter velocity index

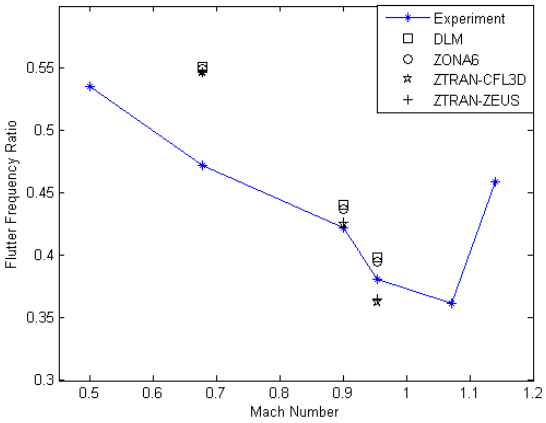

Figure 4.13. Mach number vs flutter frequency ratio

Comparing the numerical simulation with the experiment measurements at Mach = 0.678, it can be seen that although all of the methods predict the flutter index / velocity and flutter frequency higher than the experiment results, all predict flutter index reasonably well (<4% difference). However, for flutter frequency, at least 15% difference is observed. Comparing the numerical simulations with the four unsteady aerodynamic modeling to one another, all these simulations show very close results for both flutter velocity and flutter frequency. Since the flow is expected to be fully subsonic, it is not surprising that all these four numerical methods show similar results. These four unsteady aerodynamic modeling techniques are all well-studied and validated in the subsonic flow regime. The large differences between predicted and experimental flutter frequency are puzzling and may indicate other nonlinear effects (See, for example, [87], Figure 4.5).

When the Mach number increases to 0.901 all four unsteady aerodynamic modeling methods still show a reasonably good correlation with the experiment results, with difference of less than 5% for both flutter velocity and flutter frequency. The subsonic panel methods, DLM and ZONA6, show better correlation with experiment than transonic panel method in terms of flutter index / velocity. The two transonic unsteady aerodynamic models predict the flutter frequency

better than DLM and ZONA6. It seems that when the Mach number is 0.901 the nonlinear transonic effects, to the extent that they exist, on the flutter boundary are still not significant.

A large difference between DLM and ZONA6 predictions and experimental results can be seen when the Mach number increases further to 0.954. Differences of about 10% are observed with both DLM and ZONA6 aerodynamic model. The two transonic aerodynamic panel models, ZTRAN-CFL3D and ZTRAN-ZEUS, show good correlation with experiment results with differences of less than 4%. All four aerodynamic models predict a less than 5% difference in flutter frequency relative to experiment.

Note that the two field-panels aerodynamic models used here to represent CFD-based unsteady aerodynamic prediction use steady state "background flow" CFD results [85] to develop AICs, and, therefore, it is possible that they do not benefit from the full dynamic response simulation available from time domain or linearized frequency-domain CFD field simulation codes. AICs based on such codes may better capture the unsteadiness of the flow over the range of reduced-frequencies of interest, and, when AICs based on such codes would be included in the AICs samples reflecting the results of many simulation methods, such samples would contain more statistical information regarding the uncertainty of the AICs.

It can be seen, as expected, that aerodynamic modeling techniques can play a significant role in accurately predicting the flutter behavior, especially in the deep transonic region. In the following section the system predicted uncertainty, especially due to numerical unsteady aerodynamic uncertainty, will be considered and several statistical aeroelastic simulations will be performed and compared with the deterministic simulations and test results.

4.5.2 *Aeroelastic Simulation Subject to Aerodynamic Uncertainty*

Following the steps in the approach presented earlier, the unsteady aerodynamic AIC uncertainty is modeled using uniformly distributed multipliers $\left[\tilde{\varepsilon}(i, j)\right]$. The baseline model is selected to be the ZTRAN-ZEUS model since this model predicts the flutter index / velocity and flutter frequency reasonably well in both the subsonic and transonic flow regions. For exploratory studies, ZONA6 and ZTRAN-CFL3D unsteady aerodynamic models are also selected and compared with the ZTRAN-ZEUS model to guide the uncertainty estimation. The Monte Carlo simulations are performed on the William E. Boeing Department of Aeronautics and Astronautics computer cluster at University of Washington with 16 cores for parallel computing.

4.5.2.1 *Mach = 0.678*

Following the method introduced in section 4.4**,** a Monte Carlo simulation with 10,000 runs were performed at Mach = 0.678 first. The histograms of the distributions of the flutter velocity and flutter frequency are shown in Fig. 4.14 and Fig. 4.15. Although the aerodynamic uncertainties are assumed uniformly distributed multipliers, the distributions of flutter velocity and flutter frequency show a normal distributions trend. The mean value of the distributed flutter index / velocity is 0.4258 with Coefficient of Variation (COV) equal to 0.0004 while for flutter frequency ratio the mean value is 0.5476 and COV= 0.00038. The distributions also reveal that at subsonic flow field, the COV of the resulting flutter velocity and flutter frequency based on the proposed approach presented here are extremely small. However, this observation is expected since the nominal flutter simulation at M=0.678 shows that all the three unsteady aerodynamic models predict relatively close flutter results. As noted earlier, additional CFD based AIC unsteady aerodynamic models can be added to the sample of unsteady aerodynamic methods to

capture the uncertainty levels better. Or, inversely, based on the resulting uncertainty distributions here and the experimental results, other sources of uncertainties, such as structural or experimental, may be found to have a more significant effect on flutter behavior.

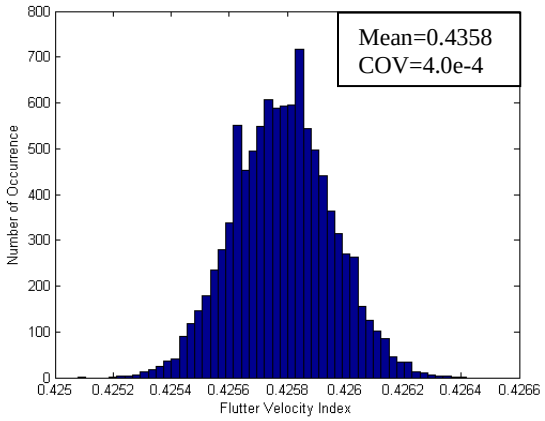

Figure 4.14. Histogram of Vf index with M=0.678

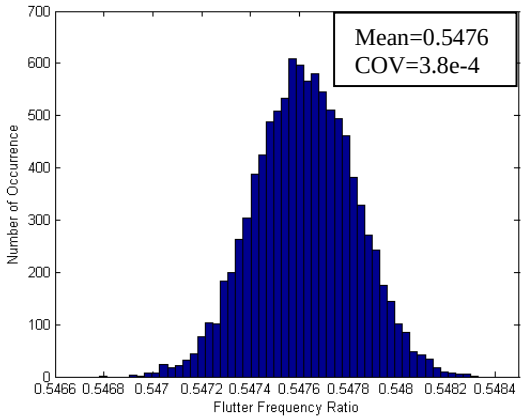

Figure 4.15. Histogram of freq ratio with M=0.678

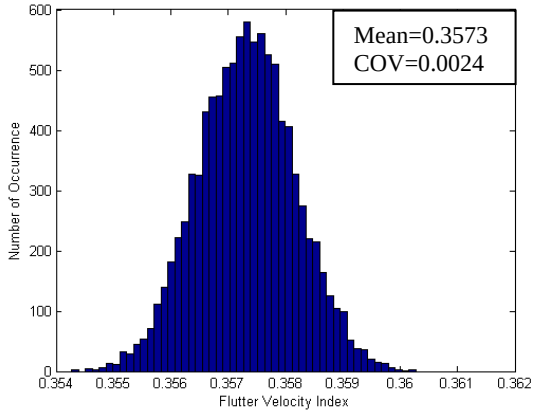

Figure 4.16. Histogram of Vf index with M=0.901

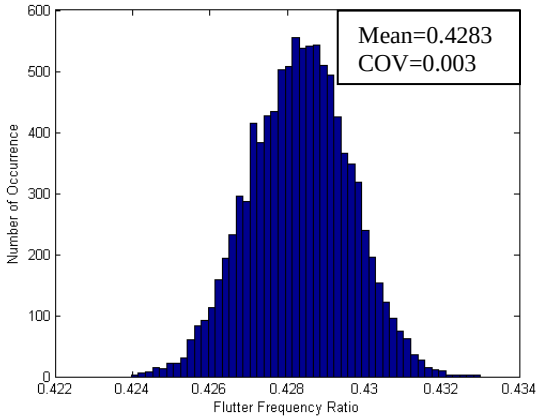

Figure 4.17. Histogram of freq ratio with M=0.901

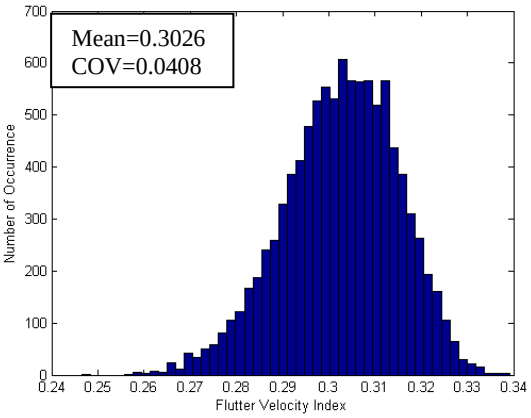

Figure 4.18. Histogram of Vf index with M=0.954

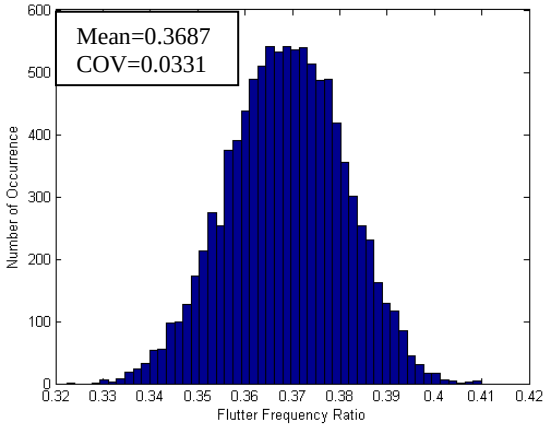

Figure 4.19. Histogram of freq ratio with M=0.954

4.5.2.2 *Mach = 0.901*

The Mach number of the simulation is increased to 0.901, where some transonic and supersonic effects are expected. With the same set up as in Mach = 0.678 case, a Monte Carlo simulation with 10,000 runs is performed with the uncertainties defined in section III.

The histograms of the distribution of the flutter index and frequency ratio in the Mach = 0.901 case are shown in Fig. 4.16 and Fig. 4.17. Distributions similar to normal are again observed. The mean value of the distributed flutter index is 0.3573 with COV equal to 0.0024 while for flutter frequency the mean value is 0.4283 with COV=0.003. Similar to the Mach=0.678 case, since all these three aerodynamic models predict very close nominal flutter index and flutter frequency ratio, the COVs of the distributed results are small again.

4.5.2.3 *Mach = 0.954*

The Mach number of the simulation is increased to 0.954 where more transonic and supersonic flow can be seen.

The histograms of the distribution of the flutter index and flutter frequency ratio at Mach = 0.954 are shown in Fig. 4.18 and Fig. 4.19. The mean value of the distributed flutter index is 0.3026 with COV equal to 0.0408, while for flutter frequency the mean value is 0.3687 with COV= 0.0331. Since the subsonic ZONA6 unsteady aerodynamic model shows significant deviation from the experiment and transonic aerodynamic model predicted flutter behavior in the nominal flutter simulation, the COV of the flutter index and flutter frequency in the statistical uncertainty simulation increased significantly (almost 100 times comparing with M=0.678 case).

Comparing the two subsonic cases with the deep transonic case at M=0.956, it can be seen that when transonic and supersonic effects became more dominant the probabilistic variations of the flutter velocity and flutter frequency become larger. When basing flutter analysis on ZTRAN-ZEUS transonic aerodynamic model, uncertainties due to areas on the wing in which linear theory does not apply and CFD analysis may face challenges can be identified and modeled and their effects on the distribution of flutter results may provide important insights.

Figure 4.20 and Fig. 4.21 show results of the uncertainty aeroelastic simulations at all three Mach numbers compared with the experimental and nominal results that have been showed in Fig. 4.12 and Fig. 4.13.

It is interesting, in any flutter uncertainty studies, to account, in addition to the uncertainty captured by uncertain flutter analysis, also for the uncertainty in experimental values, which is affected by uncertainty in flutter speed and frequency determination due to uncertainties in test flight conditions, wind tunnel flight or turbulence levels, and extrapolated flutter conditions based on subcritical testing. Refs. [58] and [93], among others, address this issue. Ref. [93] analyzed the uncertainty behavior of several flutter interpolation methodologies to determine the stochastic characteristic of experimental flutter velocity and flutter frequency determination and

showed that the COV of flutter velocity due to experimental data uncertainty can be as large as 0.047. Figures 4.22 and 4.23 (using the higher value of the COV for experimental uncertainty based on [93]) show the flutter index and flutter frequency distributions obtained by the Monte Carlo simulations alongside possible experimental flutter speed and frequency distributions plotted in the left side. Note the relative high overlap between the Monte Carlo based computational simulation and the assumed distributions, based on [93], of the experimental results except for the case of the flutter frequency at Mach=0.678. A better assignment of probability density functions to the real and imaginary parts of the AICs (using additional CFD-based AICs from additional CFD simulations) or the addition to the uncertainty modeling of uncertainty in structural dynamic parameters may better capture the uncertainty in flutter predictions in this case. This will be discussed in the following sections. In any case the results presented here, based on the limited CFD-based AICs samples used for this exploratory work, provide interesting insights.

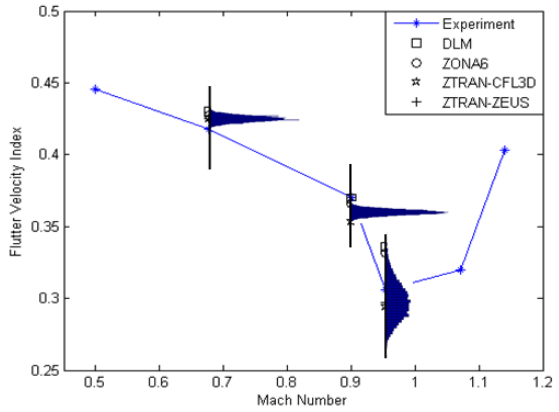

Figure 4.20. Mach number vs. flutter velocity index aero uncertainty included

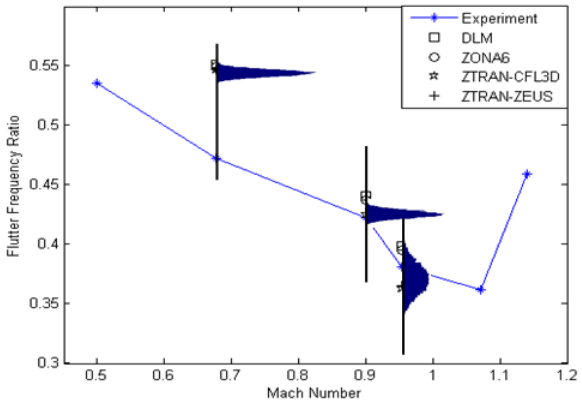

Figure 4.21. Mach number vs. flutter frequency ratio aero uncertainty included

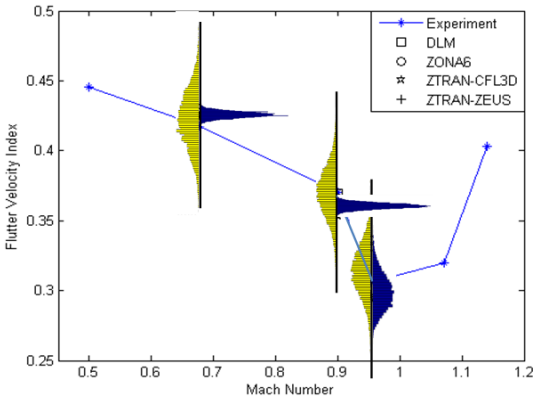

Figure 4.22. Mach number vs. flutter velocity index aero & experiment uncertainty included

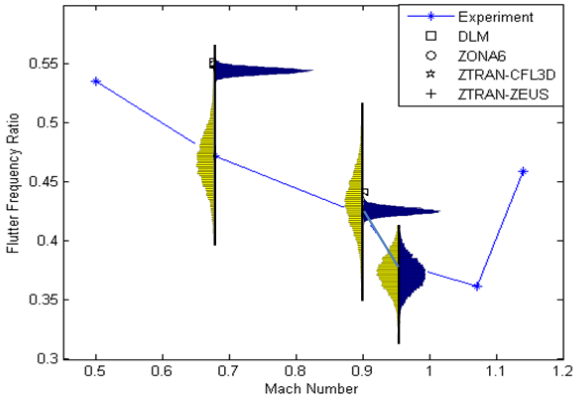

Figure 4.23. Mach number vs. flutter frequency ratio aero & experiment uncertainty included

4.5.3 *Wing Section Prioritization with Statistical Sensitivity Analysis*

A factor prioritization, often named sensitivity analysis, can be used to identify and quantitatively rank the importance of uncertain design parameters in affecting the flutter results. A variety of approaches can be utilized to perform statistical sensitivity analysis. In this work, the global sensitivity analysis of [35], which uses the variance as a measurement of uncertainty, was used.

When working with AICs on a panel aerodynamic mesh, and not with generalized AICs as in [94], insight regarding pure aerodynamic behavior and not aerodynamic behavior weighted by modal motions, may be gained. It was suggested in the early 1970s that accounting for Mach zones and local Mach numbers on a configuration might be used, heuristically, in some way to improve lifting surface predictions [95]. With CFD-based AICs, available in the cases studied here from a field-panel method, it is tempting to use stochastic sensitivity analysis in order to understand the relative importance (and contribution to aeroelastic uncertainty) of the aerodynamic "communication" between aerodynamic boxes as affected by the local Mach numbers involved. The flutter analysis and associated unsteady aerodynamics and AICs used for the present study are based on linearization with respect to a steady reference state.

In general a configuration panel model can be divided into surface zones in any selected way in order to study, by sensitivity analysis, the relative importance of uncertainty in the aerodynamic communication inside and among zones on the resulting aeroelastic uncertainty. Intrigued by the ideas presented in [95], a Mach zone surface division is studied in this work where the wing is divided into a number of zones based on CFD predicted surface Mach number distributions. For exploratory studies the sensitivity analysis is performed using the uncertainty scheme introduced above with 10,000 samples. The Sobol's [35] sequence of sampling is used to increase the rate of convergence.

4.5.3.1 *Mach = 0.678*

Fig.4.24 shows the division of the wing into zones based on the distribution of local upper-surface Mach numbers in the steady reference background flow for this case. Since the resulting variance of the flutter index and flutter frequency with the proposed aerodynamic uncertainty scheme are relatively small (Fig. 4.14, 4.15), the global sensitivity analysis here (which is based on comparison of variances) had convergence difficulty in this case. In order to examine the relative zone priority in affecting overall flutter uncertainty, the COV of the input aerodynamic uncertainties were amplified 10 times to obtain the results of the global sensitivity analysis for the flutter index / velocity and flutter frequency ratio as shown in the pie charts in Fig. 4.25.

The pie chart in this particular example shows that the aerodynamic uncertainties near the leading edge and mid wing section of the outer span area, represented in ZONE 1, ZONE2 and ZONE3, dominate the output variances for flutter velocity. This is not surprising given the thinness of the airfoil and the fact that most twisting and bending deformation in the case studied here are in the outboard area. The mid sections of the wing, in particular ZONE 4 and ZONE5, have more influence to the flutter frequency ratio than flutter index.

4.5.3.2 *Mach = 0.901*

The division of the wing surface into Mach zones in the Mach=0.901 case based on the steady background reference flow is shown in Fig. 4.26. It is interesting to see that even at M=0.901 at a zero angle of attack the flow is still subsonic on the entire test wing – a result of the thinness of the wing. The result of the global sensitivity analysis with respect to the AICs in the different Mach number zones is shown in Fig. 4.27. The pie chart indicates that the uncertainty in ZONE3 dominates more than 50% of the uncertainty in flutter behavior. Since the leading edge of the mid span area and middle section of the outer span area display the largest modal deformations in the modes contributing to flutter, it is not surprising to see again that these areas have the highest influence on the flutter behavior. A certain impact of the mode shapes involved – structural – on the uncertainty effects of AIC zones is inevitable when flutter results are studied, since it is the generalized force matrix that determines the aerodynamic contribution. Nevertheless, the zone-sensitivities identified here for the AGARD 445.6 wing case are not trivial and the approach may guide in other cases zone by zone instrumentation of wind tunnel and flight test articles and study of CFD results in ways that would lead to less uncertainty of aerodynamic prediction.

4.5.3.3 *Mach = 0.954*

Fig. 4.28 shows the discretization of wing at M=0.954. Now most of the area of the upper surface of the wing in the reference steady background flow “sees” supersonic flow mixed with the subsonic flow. The sensitivity analysis, shown in Fig. 4.29, indicates that the uncertainty in the supersonic region, mainly included in ZONE 5, now has more influence than uncertainty in the area that has the largest deformation on both the variation of flutter velocity and flutter

frequency. Since the supersonic region shows more influence on the flutter behavior, the sensitivity analysis also helps to explain the fact that two transonic unsteady aerodynamic models, ZTRAN-CFL3D and ZTRAN-ZEUS, matched the experimental flutter behavior better than subsonic models.

In conclusion, different aerodynamic models can be expected to lead to AIC element prediction differences that would be larger in areas involving shock wave fronts and mixed supersonic transonic flows. The effect of modal deformation in the critical modes would add relative weights to the different aerodynamic uncertainty contributions. The M=0.678 and M=0.901 cases have shown that the area that encounter the most deformation has the largest effect on the variance of the flutter index and flutter frequency. However, in the deeper transonic M=0.954 case, the contribution of aerodynamic transonic effects exceeds the structural modal motion effects on the overall uncertainty of flutter behavior.

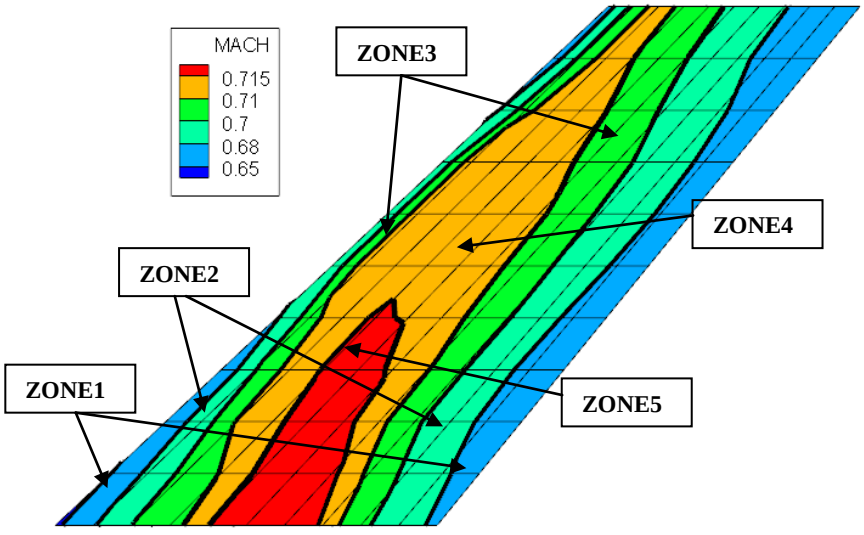

Figure 4.24. Mach zone definition for the M=0.678 case

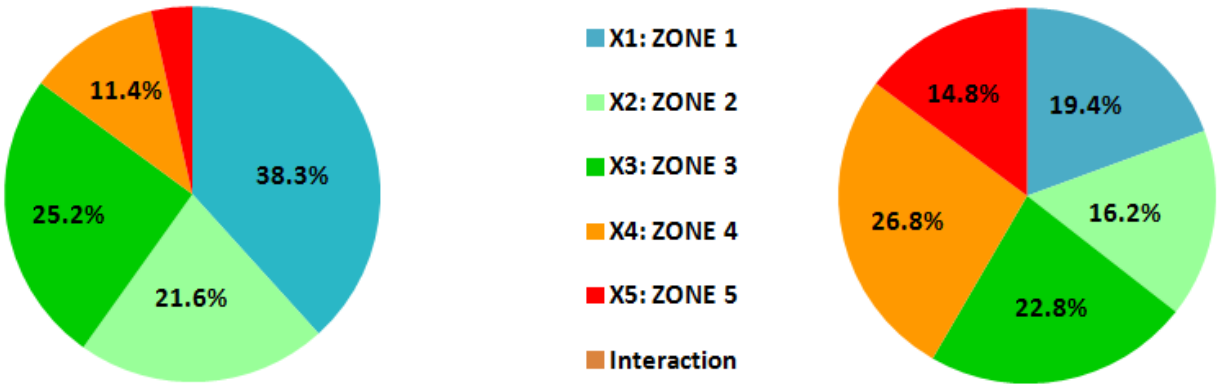

Figure 4.25. Flutter index and frequency sensitivity to zone discretization for the M=0.678 case

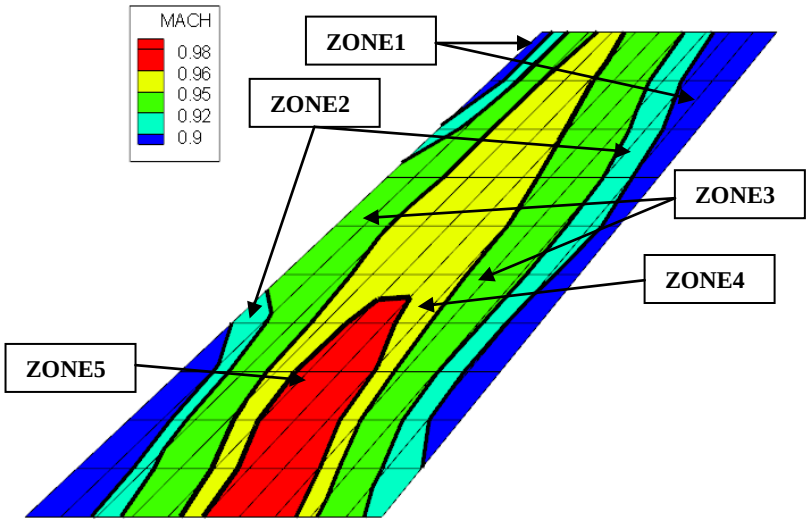

Figure 4.26. Surface Mach zone definition for the M=0.901 case

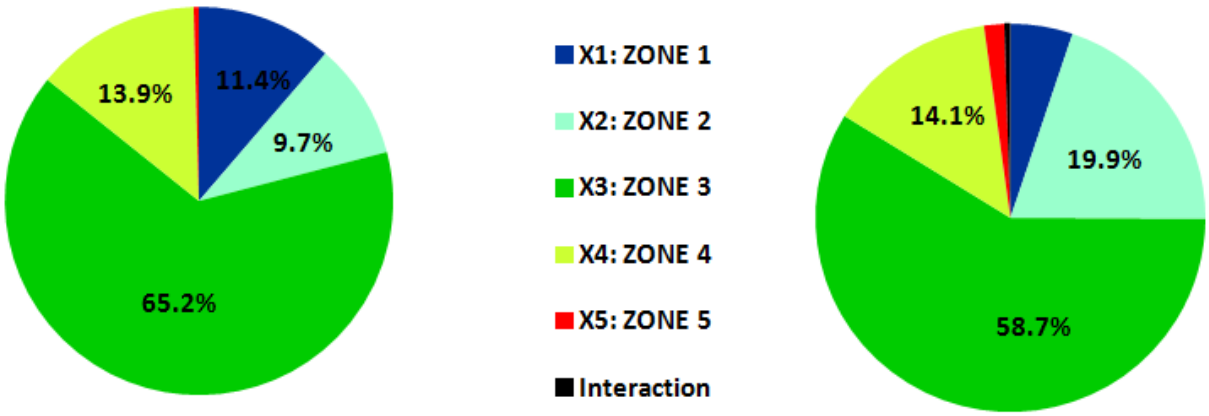

Figure 4.27. Flutter index and frequency sensitivity to zone discretization for the M=0.901 case

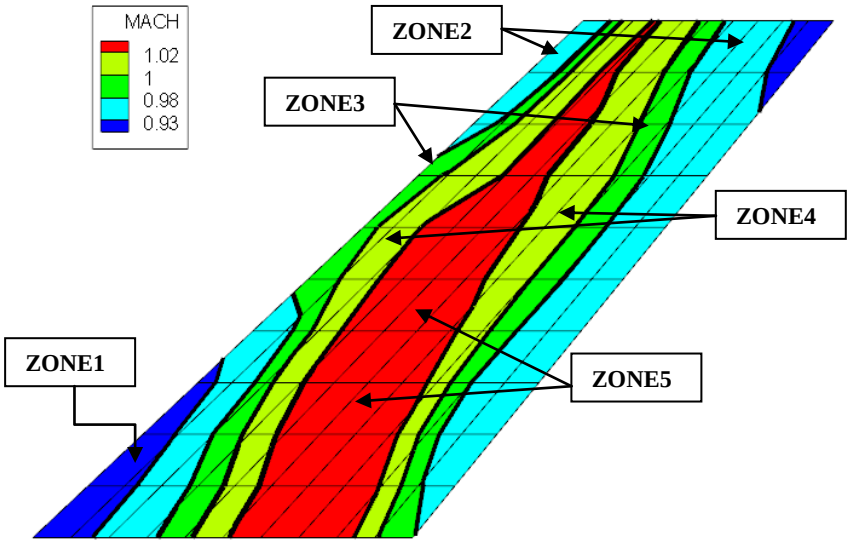

Figure 4.28. Surface zone definition at the M=0.954 case

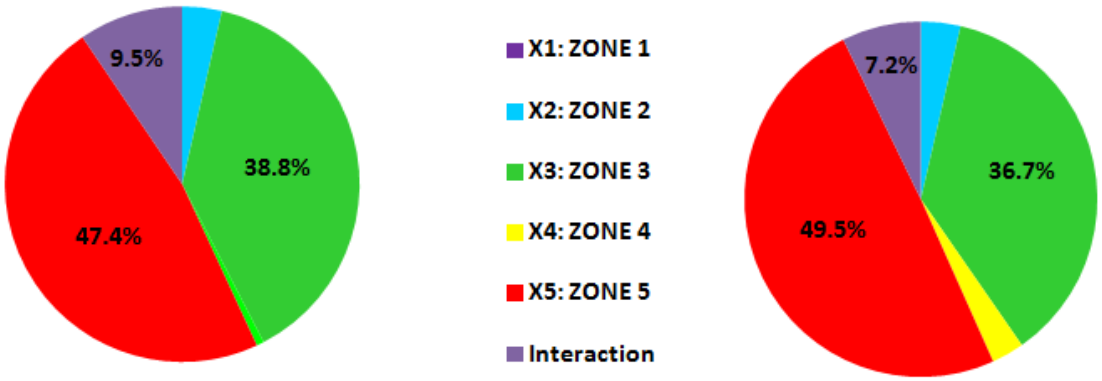

Figure 4.29. Flutter index and frequency sensitivity to zone discretization for the M=0.954 case

4.5.4 *Aerodynamic Uncertainty via Rational Function Approximation*

Assigning uncertainty distributions to the real and imaginary parts of frequency domain AICs (or generalized force matrices) is one way to model unsteady aerodynamic uncertainty in aeroelastic analysis. Another way is to examine the effects of uncertainties in rational function matrices used to model unsteady aerodynamic AIC matrices or generalized force matrices in the Laplace or time domains. Ref. [25] introduced an approach to aeroelastic unsteady aerodynamic uncertainty

in which the elements of the $[P_l]$ matrices in the Roger approximation (Eq. 4.13) of the unsteady generalized forces associated with the modal basis used are taken to be uncertain. The fixed-modes approach used in Ref. 5 is, practically, a generalized AIC approach. Treating elements of the Roger $[P_l]$ matrices as uncertain variables allows separate accounting for uncertainty in the aerodynamic stiffness, damping, and inertia, as well as the contributions by aerodynamic time lag terms – another way to gain insight regarding the aerodynamic uncertainty and how it affects different systems with different flutter mechanisms. This can also direct refining and improving unsteady aerodynamic modeling in a way that would improve flutter boundary predictions.

Uncertainty of the generalized-AIC $[P_l]$ matrices also covers the combined effects of aerodynamic uncertainties in the theory and model geometry and discretization used, the effect of interpolation uncertainty, and the uncertainties introduced by the conversion of unsteady aerodynamic loads from the frequency to the time domain (The Roger series fitting process). The uncertainty due to Mach number effects and variations is also included.

The uncertainty is added to the Roger $[P_l]$ matrices here by defining a sequence of diagonal correction matrices that multiply the $[P_l]$ matrices. For the exploratory studies presented here each element of the correction matrices is a separate uniformly distributed random variable with mean value equal to 1.0 and COV equal to 0.05. A Monte Carlo simulation with 10,000 runs was performed for the Mach = 0.954. The histograms of flutter index / velocity and flutter frequency are shown in Fig. 4.30 and Fig. 4.31.

Global sensitivity analysis is preformed with the Roger matrices uncertainty scheme to rank the relative importance of generalized aerodynamic stiffness, aerodynamic mass, aerodynamic damping and aerodynamic lags effect. The pie chart in Fig. 4.32 shows that the aerodynamic

damping has the largest influence to the variance of the flutter index and flutter frequency. This makes sense since the V-g plot for the nominal flutter simulation at M=0.954 (Fig. 4.11) shows that the flutter mechanism is relatively mild and thus the aerodynamic damping, that can shift g.vs.V branches up and down slightly, can affect the flutter speed significantly. The aerodynamic stiffness is ranked as the second parameter of importance influencing the flutter index, followed by the lag terms. In the flutter frequency case the aerodynamic lags ranked as the second parameter of influence. The pie charts for flutter index and flutter frequency both show that the aerodynamic mass has a very small influence in the AGARD 445.6 wing case.

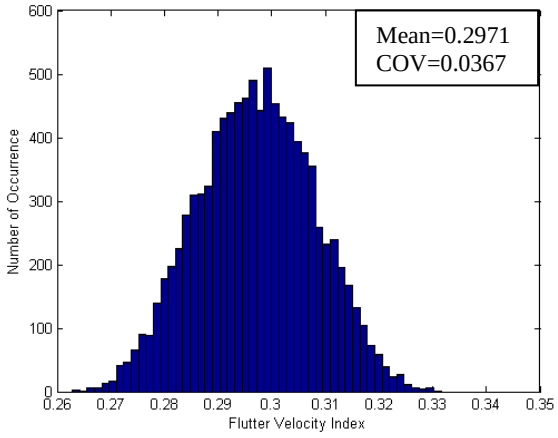

Figure 4.30. Histogram of Vf index with Roger approximation uncertainty

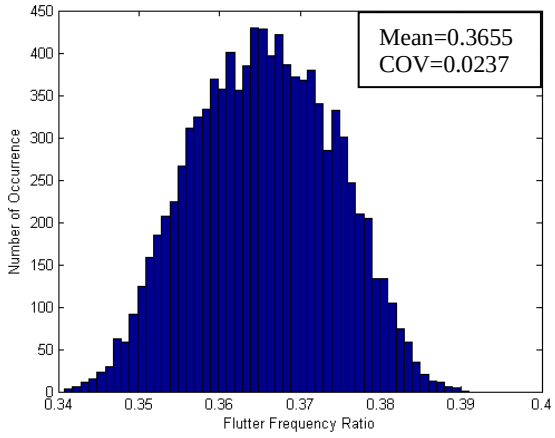

Figure 4.31. Histogram of freq ratio with Roger approximation uncertainty

Figure 4.32. Flutter index (left) and flutter frequency (right) sensitivity to Roger terms for the M=0.954 case

4.5.5 *The Addition of Structural Uncertainty*

With the Monte Carlo aeroelastic and aeroservoelastic simulation capability developed at the University of Washington, the final study that this chapter presents includes structural uncertainties in the flutter Monte Carlo simulations together with aerodynamic uncertainties modeled by the proposed AIC uncertainty approach.

The structural uncertainties here are first modeled at the fine level of detail: the plate thickness and material density spatial distributions that model the wing FEM are assumed to be normally distributed with COV equal to 0.2. A complete new FEM eigenvalue analysis was performed with each Monte Carlo run in order to obtain the most accurate structural behavior. For exploratory studies the transonic flow condition Mach=0.954 case is selected.

The histograms of the distribution of the flutter velocity and flutter frequency due to uncertainties in both structure and aerodynamic are shown in Fig. 4.33 and Fig. 4.34. The mean value of the distributed flutter index / velocity is 0.3029 with COV equal to 0.0411 while for flutter frequency, the mean value is 0.3691 with COV=0.0334. Comparing this with the aerodynamic-uncertainty-only cases, for which the COV equals to 0.0408 for flutter index and 0.0331 for flutter frequency, the structural uncertainty in this case has insignificant influence.

Following the modeling of structural uncertainty at the element by element detailed level, a structural dynamic uncertainty modeling approach in which the system's natural frequencies are treated as uncertain variables is tested [56]. A fixed-modes approach is used and the number of modes in the fixed-modes basis used are increased to 20 from 5. The uncertainties are added to the first five natural frequencies and modal damping ratios with the nominal values taken to be the mean and with 0.5 COV assumed. The histograms of the distribution of the flutter velocity and flutter frequency due to uncertainties in both structure and aerodynamic are shown in Fig.

4.35 and Fig. 4.36. It is also shows that the effects of structural dynamic uncertainty on the flutter behavior in the case here are very low.

The effects of structural damping uncertainty on the flutter index / velocity and flutter frequency ratio are also evaluated. The M=0.954 case is selected, again, since the v-g plot (Fig. 4.11) shows the flutter mechanism is relatively mild and the damping may have a large effect on the flutter behavior. The structural damping is added mode by mode, uniformly distributed between 0 and 0.08, and represented by a generalized diagonal damping matrix. As in the nominal analysis, five modes are included in the numerical simulations and, thus, five damping ratios are used. The distribution of flutter index and flutter ratio are shown in Fig. 4.35 and Fig. 4.36. It can be seen that, the influence of the structural modal damping on the flutter boundary behavior is still relatively small (COV=0.0014 and 0.001) compared with the influence of aerodynamic uncertainty (COV=0.0408 and 0.0331). Although the structural modal damping has insignificant influence on the flutter behavior in our case when the flutter mechanism is mild, the aerodynamic damping affects it dramatically (Fig. 4.30). The distribution shape of flutter index and frequency is found to be a uniform distribution rather than the normal distribution shown in the aerodynamic uncertainty cases. However, these results are limited and case dependent.

A global sensitivity analysis is performed with the structural modal damping uncertainty to find the most influential structural modes regarding flutter index and frequency. The pie chart in Fig. 4.39 shows that mode 1 completely dominates the flutter index and flutter frequency. All the other modes, as well as modal interactions, have total influence of less than 2%. The results indicate that the first structural mode is the primary mode that contributes to the flutter mechanism.

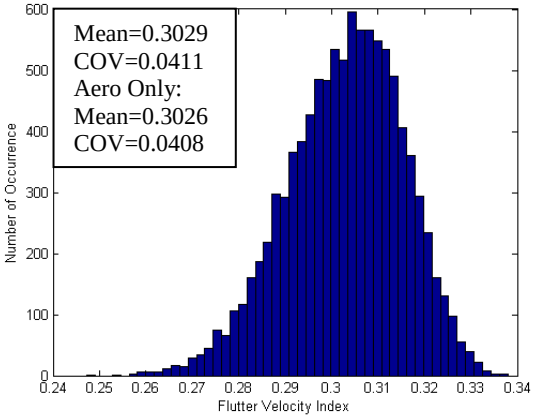

Figure 4.33. Histogram of Vf index with aero + structural uncertainty at the detailed level

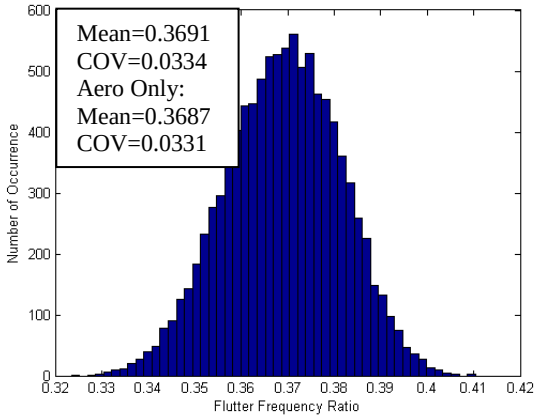

Figure 4.34. Histogram of flutter frequency ratio with aero + structural uncertainty at the detailed level

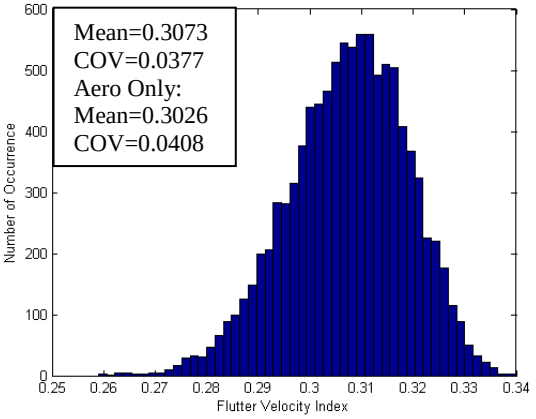

Figure 4.35. Histogram of Vf index with aero + structural uncertainty at higher level

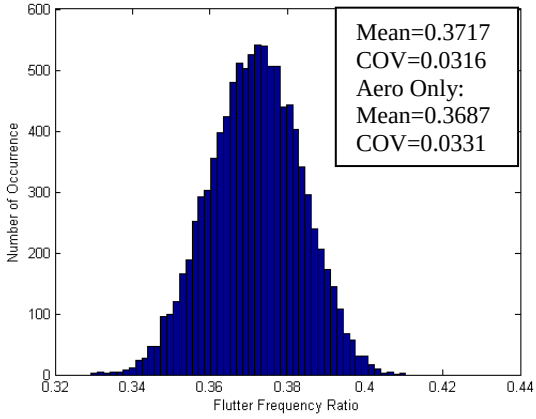

Figure 4.36. Histogram of frequency ratio with aero + structural uncertainty at high level

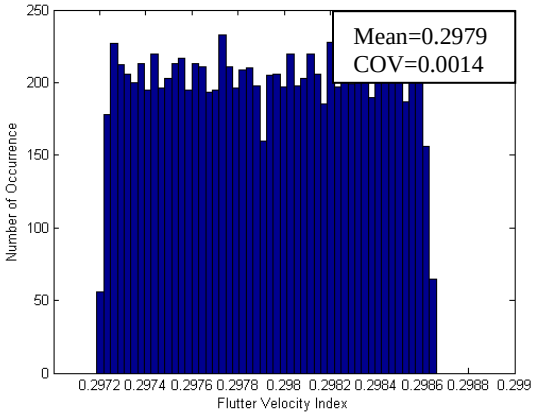

Figure 4.37. Histogram of Vf index with damping uncertainty

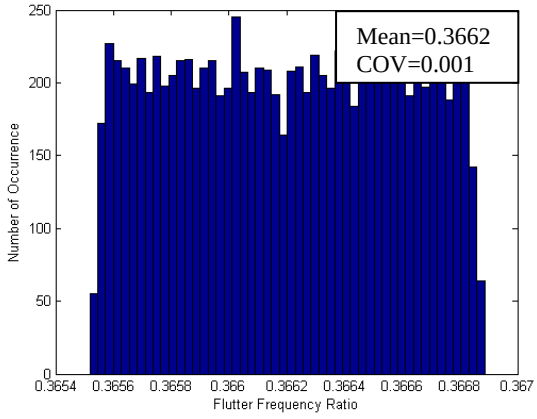

Figure 4.38. Histogram of freq ratio with damping uncertainty

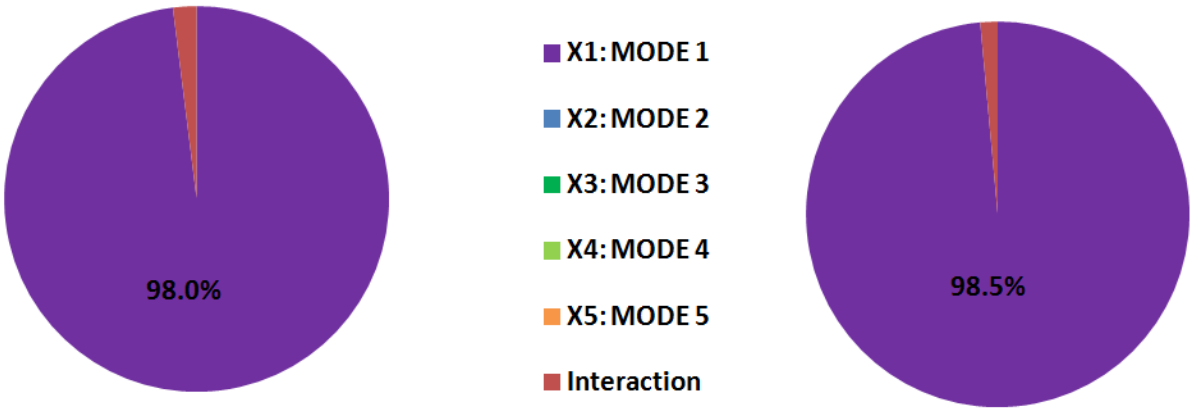

Figure 4.39. Flutter index and frequency sensitivity to structural modal damping for the M=0.954 case

4.6 CONCLUSION

Two aerodynamic uncertainty modeling approaches for flutter analysis are described. In one, differences between CFD-based and linear unsteady aerodynamic based AIC elements, or difference between several CFD-based AICs using different steady CFD models, guide the assignment of uncertainty to all AIC matrix elements column by column. The approach can be automated, based on the magnitude of such differences or the corrections needed to transform linear-theory AIC matrices to CFD-based AIC matrices. When modeling uncertainties are applied at AIC matrix element levels on panel aerodynamic meshes they are purely aerodynamic and, thus, the structural uncertainties and aerodynamic uncertainties in flutter prediction can be separated. In a second approach to unsteady aerodynamic uncertainty modeling, the rational function approximation aerodynamic stiffness, damping, inertia, and lag matrices are treated as uncertain. Insights regarding the relative importance of such aerodynamic uncertainty effects can be gained. Identification of AIC elements or AIC surface zones to whose influence the uncertainty of flutter boundary predictions is more sensitive, or the more important among the

aerodynamic stiffness, damping, inertia, and lag effects can guide improved modeling and testing that would lead to reduced flutter prediction uncertainty.

In the exploratory studies reported here the effect on the flutter boundary prediction of AIC uncertainty in the case of the historical AGARD 445.6 weakened wing model was evaluated as a function of Mach number. The results suggest that the largest uncertainty in flutter velocity and frequency predictions exists in the transonic flow domain where the difference between subsonic and transonic aerodynamic simulation methods and between different CFD-based simulations can be significant. While the approach is just one of a number of approaches to the modeling of aerodynamic uncertainties in flutter calculations, it offers physical insights that add to other insights and perspectives that other approaches offer. When aerodynamic uncertainty was accounted for by variation of Roger matrices, global sensitivity analysis showed that in the AGARD 445.6 case the aerodynamic damping uncertainty dominates the uncertainty in flutter predictions. A case involving both structural uncertainty and aerodynamic uncertainties was presented at transonic M=0.954 in which, limited to this case, structural uncertainties were found to be much less important than aerodynamic AIC uncertainties. This is interesting because of the capability of the suggested approach to separate contributions of aerodynamic and structural terms into pure structural and pure aerodynamic terms compared with approaches that assign uncertainty to terms of generalized aerodynamic matrices which reflect structural and aerodynamic contributions, coupled in the expression of generalized aerodynamic terms, which are not separable.

No matter how unsteady aerodynamic uncertainty or structural uncertainty are modeled (AIC or rational function approximation matrices in the aerodynamic case, and detailed element by element modeling or modal characteristics uncertainty modeling in the structural dynamics

case), global sensitivity analysis can be used with the Monte Carlo simulations possible now to identify the most important aerodynamic and structural dynamic uncertainty contributions to the uncertainty of the predicted flutter boundary and to direct more careful mathematical modeling and tests to improve modeling accuracy and reduce modeling uncertainty.

The work is expected to make a contribution to the understanding of the propagation of aerodynamic uncertainty and the resulting reliability of realistic integrated aeroservoelastic system models of the detail and complexity that allow modeling real modern aircraft.

Chapter 5. PROBABILISTIC GUST LOADS ANALYSIS ACCOUNTING FOR AEROSERVOELASTIC SYSTEM UNCERTAINTY‡

5.1 OVERVIEW

A newly developed computational capability for Monte-Carlo simulations of uncertain aeroelastic and aeroservoelastic systems is used to obtain gust response statistics accounting for uncertainties in both aircraft aeroservoelastic model and the discrete & continuous gusts exciting it. Gust response is evaluated in both the frequency and time domains. Root-mean-square values based on power spectral density analysis as well as maximum and minimum loads predicted by time domain analyses are selected for study and compared with common gust loads prediction approaches. Statistical sensitivity analysis is performed to rank the relative importance of the parameter to the system output of interests. A numerical example of the gust response of a generic transport aircraft model shows a significant increase of the critical loads when uncertainty in system's parameters is accounted for and leads to a quantitative evaluation of probability distributions of all output quantities of interest.

5.2 INTRODUCTION

The accuracy and reliability of calculating unsteady loads, especially gust loads, play a significant role in the design, analysis, and certification of aircraft. These loads determine extreme stresses as well as stress time histories that influence the strength, fatigue, and passenger comfort characteristics of aircraft. The way dynamic loads due to atmospheric gusts have to be accounted for in the design and certification of commercial aircraft has been specified in federal regulations, such as FAR-25, for large commercial transports. Two main complementary

---

‡Content of this chapter is published in [81]

approaches are used: In the time domain the response to gusts of given profiles is analyzed in a way that would cover a range of gust amplitudes and durations that would ensure capturing worst case scenarios, regarding aeroelastic and aeroservoelastic dynamic response; In the frequency domain a Power Spectral Density (PSD) approach may be used, based on frequency-domain statistics of atmospheric turbulence collected and analyzed over many years of research and flight operations for all atmospheric weather conditions. Key information on the subject of aeroelastic and aeroservoelastic gust response and the methods used for gust loads certification can be found in [61, 63, 96-112].

Atmospheric gusts are naturally random. Therefore, in any discrete-gust response analysis subject to gust inputs of pre-set shapes (such as the commonly used 1-cosine gust profile), large numbers of gust inputs are required in analysis to make sure that all aeroelastic frequencies and modes of behavior would be excited in the most critical way (within certain probabilities). This may mean, in an industry setting focused on an aircraft model of given aeroelastic characteristics, tens of thousands if not hundreds of thousands of time domain gust response simulations [113]. Meanwhile, in the continuous-turbulence approach, atmospheric turbulence statistics can be captured effectively by power spectral density analysis. The approach has certain limitations, however, including cases involving aeroservoelastic nonlinearities.

In both cases variations of aircraft characteristics must be covered by any design and certification process. This is usually done by parametric studies in which critical configurations are selected for analysis, e.g. full-fuel wing, empty wing, different fuel and payload weights and weight distributions, etc. Addressing variations in flight vehicle dynamic characteristics we should distinguish between those variations that are planned and known (such as mass and flight condition variations) and those due the uncertain nature of the system, its elements, and its

operation. The emergence of powerful computers capable of running multiple aeroservoelastic simulations within practical time and computer resource limitation has led to a growing number of efforts to develop new methods for addressing the aeroelastic uncertainty problem. A brief list of publications on aeroelastic and aeroservoelastic uncertainty can be found in [6] and [25]. The focus to date seems to have been on aeroelastic and aeroservoelastic stability. In most aeroelastic and aeroservoelastic uncertainty studies published so far, adding the uncertainty in systems parameters to the uncertainty in gust inputs has been quite limited, if present at all.

Following the work presented in [25, 119, 120, 121], and expanding it, the purpose of the work reported here is to explore the effects of uncertainty in aeroelastic and aeroservoelastic system characteristics, when combined with the uncertainty of atmospheric gust inputs, on the resulting uncertainty of internal gust loads. The relative importance of system parameters to the overall system's output of interest is ranked by using global sensitivity analysis [35].

A brief introduction to the models for dynamic loads in integrated aeroelastic plant / sensors / actuators / control laws systems excited by gust inputs is presented first in this chapter. Random aeroservoelastic gust response models are considered and evaluated in both frequency and time domains, accounting for, in addition to the intensity and dynamics of gust inputs, also uncertainties in the airframe. A representative Generic Transport Aircraft (GTA) model is selected for the studies described here using the new MATLAB based Monte Carlo aeroservoelastic simulation capabilities developed at the University of Washington for such studies.

5.3 MODEL DERIVATION

5.3.1 *Aeroelastic System with Gust Excitation*

A complete aeroservoelastic (ASE) mathematical model includes the aeroelastic plant, a sensor block, an actuator block, control laws, and a gust dynamic model. The aeroelastic plant includes flexible aircraft structural dynamics, unsteady aerodynamics, and gust input dynamics. The focus of the study here is on aeroservoelastic systems simulated by linear time invariant state space models for small perturbation motions relative to steady equilibrium flight conditions. Noise in all channels can be introduced following common practices in control systems theory, including uncertainty in excitation when gust response or other dynamic response phenomena are simulated. A summary of the key equations that model the aeroservoelastic gust response model can be found in Chapter 2.4.

5.3.2 *Gust Input Uncertainty in the Time Domain*

Discrete one-dimensional gusts are commonly represented for design purposes by a so-called '1-cosine' gust, where the variation in the velocity of the air normal to the path of the aircraft is shown in Fig. 5.1.

The spatial mathematical expression of the '1-cosine' gust profile is defined as

$$w_G(t) = \begin{cases} 0 & t < 0 \text{ or } t > \dfrac{2H}{V} \\ \dfrac{W_G}{2}\left(1 - \cos\dfrac{\pi V t}{H}\right) & 0 \le t \le \dfrac{2H}{V} \end{cases} \tag{5.1}$$

where W_G is the magnitude of gust velocity, H is the gust gradient and V is the airplane's flight velocity.

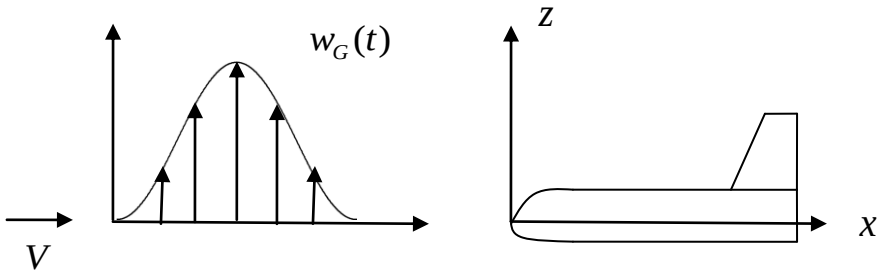

Figure 5.1. Excitation by the discrete gust 1-cosine profile

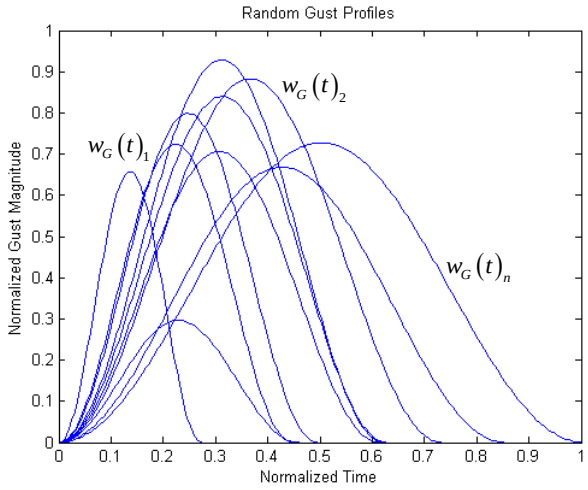

Figure 5.2. '1-cosine' gust profiles with combination of gust velocity and gradient

A common practice for addressing gust profile uncertainty while finding the most critical internal loads induced in the airframe is to define a family of gust profiles with a random combination of the gust velocity magnitude and gradient (Fig. 5.2). One of the particular interests of the discrete gust response is the gust gradient *H* that produces the maximum and minimum response of particular outputs $\{y\}$ in Equation (2.27). At particular wing and fuselage cross sections internal stresses would be associated with internal sectional loads, and the most critical combinations of internal loads (or different stresses for particular elements) must be covered by the design process. Such correlated responses can be plotted against each other to create hulls in 2D or 3D spaces (depending on the number of interacting loads and stresses).

"Extreme" points on such hulls are used to define the critical load cases ([61], Chapter 6, [117]). Such plots are usually referred to as 'potato' plots.

5.3.3 *Gust Input Uncertainty in the Frequency Domain*

Atmospheric turbulence is continuous and irregular. It can be represented by a random variation in velocity of the air normal or parallel to the flight path of the aircraft. Although not fully Gaussian, it has been common in the simulation of the response of flexible aircraft to gust inputs to use zero-mean Gaussian distributions described mainly by two Power Spectral Density (PSD) functions: the Dryden continuous gust model and the von-Karman model ([61]).

For the vertical gust velocity Dryden model the PSD function is

$$\Phi_w(\omega) = \frac{\sigma_w^2 L}{\pi V} \frac{1+3(\omega L/V)^2}{\left[1+(\omega L/V)^2\right]^2} \tag{5.2}$$

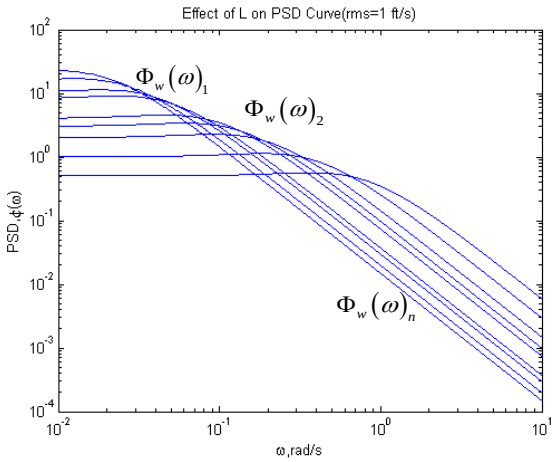

Figure 5.3. PSD of the Dryden model with different scales L

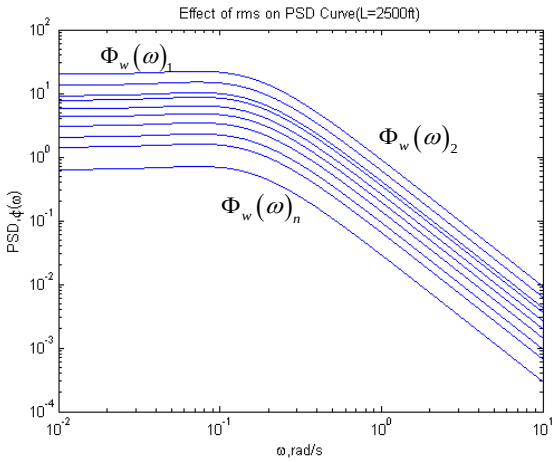

Figure 5.4. PSD of Dryden model with different rms value

The von-Karman turbulence PSD function is

$$\Phi_w(\omega) = \frac{\sigma_w^2 L}{\pi V} \frac{1 + \frac{3}{8}\left(1.339\,\omega L/V\right)^2}{\left[1 + \left(1.339\,\omega L/V\right)^2\right]^{11/6}} \tag{5.3}$$

where σ_w is the root-mean-square (rms) gust velocity, L is the "scale of turbulence" ([61], p. 42-51), and V is the flight velocity.

The rms value can be calculated from the PSD of the gust input by:

$$\sigma_w^2 = \int_0^\infty \Phi_w(\omega) d\omega \tag{5.4}$$

Based on a significant data collection and analysis efforts over years, [61] shows that the parameter L in the PSD functions varies over a considerable range from one turbulence patch to another in the atmosphere (Fig. 5.3). Gust input rms values also vary significantly in the atmosphere and as functions of weather conditions (Fig. 5.4). These two parameters should be considered, therefore, as random variables in both the Dryden and von-Karman PSD turbulence models, especially if the low frequency gust responses are of interest.

The power spectral density of the response for a linear single-input / single-output dynamic system due to random excitation can be written as

$$PSD_{out}(\omega) = \left|H(j\omega)\right|^2 PSD_{in}(\omega) \tag{5.5}$$

where $H(j\omega)$, a function of frequency, is the transfer function between the input and output of the dynamic system.

As was stated earlier, the new integrated aeroservoelastic simulation capability used for the present work can be used for gust response analysis in either the frequency domain or the time domain. Beginning with the frequency domain power spectral density (PSD) approach to gust response, the effects of random variations in the physical parameters of the system are studies in addition to the effects of uncertainty of the gust inputs.

The state space model for a flexible airplane can be presented in the multi-input / multi-output (MIMO) transfer function form by:

$$\{y(j\omega)\} = \left\{\left[C_{output}\right]\left[j\omega[I] - [A_{SYS}]\right]^{-1}\left[B_{GSYS}\right] + \left[D_{output}\right]\right\}\{u_G(j\omega)\} \tag{5.6}$$

In the case of a single gust velocity input, perpendicular to the flight path (vertical or lateral):

$$\{u_G(j\omega)\} = \begin{Bmatrix} w_G(j\omega) \\ j\omega w_G(j\omega) \end{Bmatrix} = \begin{Bmatrix} 1 \\ j\omega \end{Bmatrix} w_G(j\omega) \tag{5.7}$$

The transfer function of the plant system becomes:

$$H(j\omega) = \left\{\left[C_{output}\right]\left[j\omega[I] - [A_{SYS}]\right]^{-1}\left[B_{GSYS}\right] + \left[D_{output}\right]\right\}\begin{Bmatrix} 1 \\ j\omega \end{Bmatrix} \tag{5.8}$$

By introducing variations in structure, aerodynamics, and control system components we can generate samples of $[A_{SYS}]$ and $[B_{GSYS}]$ matrices subject to uncertainty. The uncertain transfer function $H(j\omega)$ can then be evaluated over a range of frequencies of interest. Together with the Power Spectral Density of gust velocity inputs (which in itself have uncertain parameters such as the scale of turbulence and the rms) we can now find the sample of PSD functions for the uncertain aeroelastic system output affected by the uncertain gust field it flies through.

5.3.4 *The Addition of a Gust "Filter" to the Math Model of the System*

To take advantage of mathematical and computational techniques for the analysis and simulation of the response of dynamic systems to white noise, integrated aeroservoelastic models are usually augmented by adding a dynamic model of gust inputs as a filter (a dedicated dynamic system) that converts white noise inputs to the gust inputs of the desired intensity and frequency content that excite the structure.

The transfer function of a filter that produces the Dryden turbulence PSD can be obtained exactly [61]:

$$\frac{w_G}{\eta} = \sigma_w \sqrt{\frac{\tau}{\pi}} \frac{1+\sqrt{3}\tau s}{(1+\tau s)^2} \tag{5.9}$$

The filter that would describe the von-Karman model can be approximated by a rational function that would lead to a linear time-invariant state-space model. An excellent approximation [61] is available in the range $0 \le \tau\omega \le 200$

$$\frac{w_G}{\eta} = \sigma_w \sqrt{\frac{\tau}{\pi}} \frac{(1+2.187\tau s)(1+0.1833\tau s)(1+0.021\tau s)}{(1+1.339\tau s)(1+1.118\tau s)(1+0.1277\tau s)(1+0.0146\tau s)} \tag{5.10}$$

where η is a white-noise input magnitude with constant unit PSD over the frequency range of interest, s, is the Laplace variable, and $\tau = L/V$.

Converting the rational gust input transfer functions to state space form leads to:

$$s\{x_G\} = [A_G]\{x_G\} + [B_G]\{\eta\} \tag{5.11}$$

$$\{y_G\} = [C_G]\{x_G\} + [D_G]\{\eta\} \tag{5.12}$$

where the input to the gust filter is a white noise of given RMS value and the output $\{y_G\} = \{u_G\} = \{w_G \quad \dot{w}_G\}^T$ is the gust velocity and acceleration inputs that excite the structure.

With the assumption that the control actuator's transfer function has denominator that are higher in order than the numerator by least 2, combining Equation (5.11) and Equation (5.12) with Equation (2.21) and Equation (2.27), a complete aeroelastic model with an atmospheric turbulence filter can be presented by:

$$s\begin{Bmatrix}\{x_{SYS}\}\\ \{x_G\}\end{Bmatrix} = \begin{bmatrix}[A_{SYS}] & [B_{GSYS}][C_G]\\ [0] & [A_G]\end{bmatrix}\begin{Bmatrix}\{x_{SYS}\}\\ \{x_G\}\end{Bmatrix} + \begin{bmatrix}[B_{GSYS}][D_G]\\ [B_G]\end{bmatrix}\{\eta\} \tag{5.13}$$

$$\{Y\} = \begin{bmatrix}[C_{output}] & [D_{output}][C_G]\end{bmatrix}\begin{Bmatrix}\{x_{SYS}\}\\ \{x_G\}\end{Bmatrix} + [D_{output}][D_G]\{\eta\} \tag{5.14}$$

When uncertainties affect both aeroelastic system (structure, aerodynamics, actuators, sensors) and gust model, the statistical distribution of loads and any other outputs of interest can be evaluated by using Equation 5.13 and 5.14 through Monte Carlo simulations.

Revisiting an issue already mentioned briefly earlier: A distinction can be made between parametric studies (modeling variations that we may denote as "large") of gust response that account for large, but mainly well modeled, system variations, such as major configuration mass / shape / flight conditions changes together with major gust intensity changes due to different weather conditions, and the analysis of the effect of "small" uncertainties in such different configuration and flight operation cases. The terms "large" and "small" are used here only qualitatively, of course.

In essence all variations in system parameters can be accounted for by the Monte Carlo simulation capabilities described here, including (subject to their probability distributions) "large" variations due to the way the aircraft is operated and "small" variations due to inherent uncertainty in modeled aircraft dynamics whatever the configuration and flight condition is. The nature of the probability distributions involved in the "large" and "small" variation cases is different, with the "large" variations reflecting operation procedures and uncertainties and the "small" variations representing uncertainties due to manufacturing, environmental, and maintenance procedure effects as well as uncertainties due to aircraft not being operated precisely in the way they are planned to be. Uncertainty due to damage can fall into the "small" or "large" variation categories. The number of cases required for Monte Carlo simulations that would cover all types of system variations is very large but still practical, we believe, using the capability described here on current high power computing hardware.

Still, with the vast experience today regarding configuration and operation variations over the service-life of different families of aircraft, it is more practical to address the gust response uncertainty problem by combining critical pre-selected configuration and flight condition combinations and carry out Monte Carlo simulations only for uncertainty in system dynamics and its inputs with respect to such configurations. The study case selected here, to demonstrate the new capability and gain insight regarding the impact of uncertainties on gust response, is focused on a given configuration and flight operation case.

5.4 Numerical Example of Gust Response with Uncertainty

The Generic Transport Aircraft model (GTA, [28]) is available in the open literature and is widely used for the validation of analysis methods and for studies in the areas of loads, flutter, and gust alleviation control law design. The weight of the model is 7203.7 kg. The wing span is 19.0 m and the chord length is uniformly equal to 2.3 m. The length and height of the aircraft are 22.0 m and 6.0 m, respectively. Since the aircraft and gust condition are symmetric in this research, half of the airplane was modeled to speed up the simulation. The structural stick finite element model of the aircraft is shown in Fig. 5.5 and the aerodynamic model is shown in Figure 5.6. The FE model includes 93 nodes and 158 structural elements while the aerodynamic model has 155 Double Lattice Method (DLM) panels. The two models are coupled by interpolation using the infinite surface spline method. All modeling was done using the University of Washington developed integrated aeroservoelastic simulation capability which covers all disciplines involved at all levels of detail.

The nominal discrete and continuous gust response analysis of the GTA model is performed at Mach number 0.3 and altitude equals to 5000 m. A first check shows there is no flutter at the

flight conditions of interest, Fig. 5.7. Simulations based on a cantilevered model are presented first. The new capability can simulate aircraft in free-free motion too [118].

5.4.1 *Discrete Gust Response with System Uncertainty*

The profile of the discrete gust is described in Equation (5.14). The flight velocity corresponding to the Mach number at which the model is evaluated is V= 96.2 m/s. The magnitude of gust vertical velocity is w_G =30.48 m/s and the gust gradient H equals to 15 m.

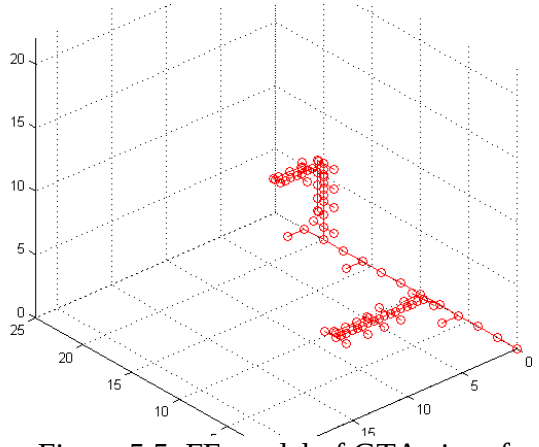

Figure 5.5. FE model of GTA aircraft

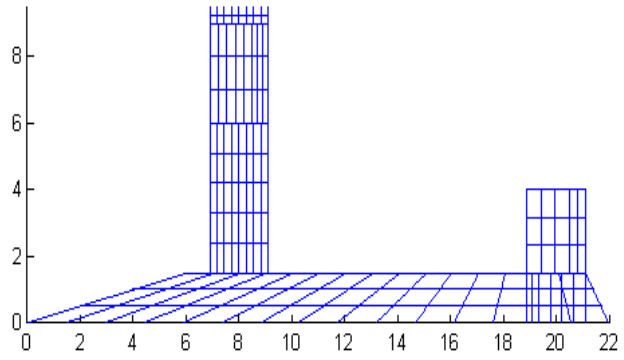

Figure 5.6. DLM aerodynamic model

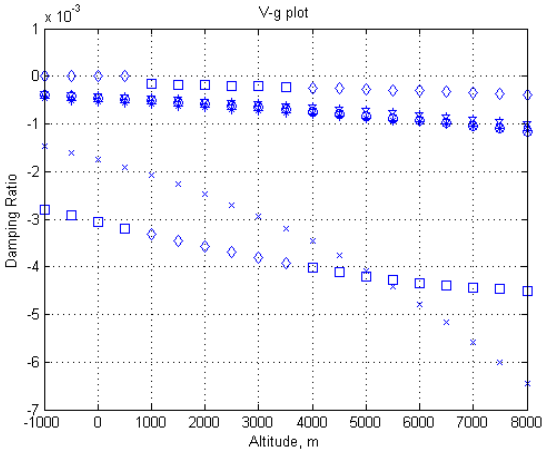

Figure 5.7. V-g plot of nominal GTA model

Nominal discrete gust response analysis was performed first and the maximum / minimum wing tip acceleration, wing root shear force, and wing root bending moment were captured via time domain simulation.

Following the nominal case, the gust properties, magnitude of gust velocity and gradient, together with flight velocity are treated as random variables. Uniform distribution is assumed. With the structural properties such as mass and stiffness matrices kept fixed, this simulates the tuning of gust input parameters – the process commonly carried out as part of the gust load evaluation process for aircraft ([61], p. 16-18 and [100]).

In order to evaluate the effects of aircraft's plant variation on the maximum load distribution, the Monte Carlo simulations were carried out with additional uncertainties in the FE model. Randomly-varied structural parameters were selected to represent the mass and stiffness uncertainties of the stick FE model. Mass elements represent the mass distribution in the aircraft, and are modeled as lumped masses in the GTA model. Each lumped mass and stick / beam stiffness has its own statistical distribution of properties, assumed as normally distributed, and correlated with nearby elements.

The new capability used here allows for any statistical variation of gust input parameters (correlated or independent) together with variations in system parameters. In general the simulation capability here can be used with any probability distribution for any of the physical system parameters involved.

While hundreds of thousands of ASE simulations can be run efficiently with the capability used here [25], 50,000 simulations with 15% COV of its nominal value were preformed to find the critical gust loads with both fixed and varied / uncertain aircraft structural model with '1-cosine' gust whose parameters are also subject to variation. The structure random parameters,

mass and stiffness, are distributed using truncated normal distributions while the gust properties are uniformly distributed which will give the maximum entropy. The comparisons of histograms of the maximum and minimum wing tip acceleration and root shear force together with the nominal values (shown in box) are plotted in Fig. 5.8, Fig. 5.9. Since the wing root bending moment and torsion moment have a similar trend as wing root shear force, they are not listed and plotted in the report. It can be seen that, when uncertainty exists, the most critical loads can significantly increase compared to the nominal loads. This is routinely addressed by parametric studies during the design and certification of aircraft to make sure the worst-case gust inputs and resulting loads are captured. It can be also visualized that in the present case structural uncertainties play relatively insignificant role, with the assumed level of uncertainty studied here, in determining the most critical combination of the gust loads when compared with the case of the fixed structural model. The relative importance of uncertainty in gust and speed inputs and structural parameters depends, of course, on the relative magnitude of uncertainty in such parameters.

A statistical sensitivity analysis was performed to rank the relative importance of random input parameters to the system's overall outputs of interest. A variety of approaches can be utilized to perform the sensitivity analysis. However, in the work reported here, the global sensitivity analysis [35] method using the variance as a measurement of uncertainty was selected to evaluate factor prioritization.

The global sensitivity indices of these system two outputs are calculated with another 50,000 runs of simulation and are plotted in Fig. 5.10 and Fig. 5.11. The pie charts show that the w_G, H and flight velocity variables dominate the variance of the output. The structural mass and stiffness have the least influence on the variation of output in the cases studied here. Only the

first order indices [35] of the sensitivity function were necessary and been calculated to rank the relative importance of the random parameter and, thus, the higher order indices and numerical error effects are shown in the pie chart with the term ‘other and interaction’.

As expected from Fig. 5.8 and Fig. 5.9, the maximum wing tip acceleration and wing root bending moment may increase by small amounts when the structure is subjected to variation. The sensitivity indices show the significant effect of flight velocity uncertainty on gust loads relative to any structural uncertainties of the same relative magnitude. When structural reliability of flight vehicles is considered for a vehicle of the type considered here, the way airplanes are actually operated [6], thus, is as important, if not more important, than the uncertainty of their airframes.

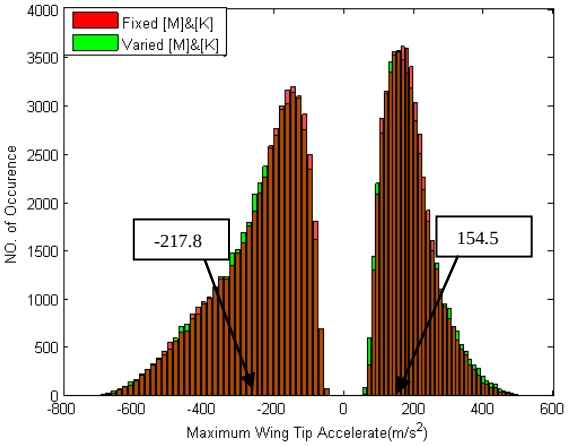

Figure 5.8. Hist of max/min wing tip acceleration

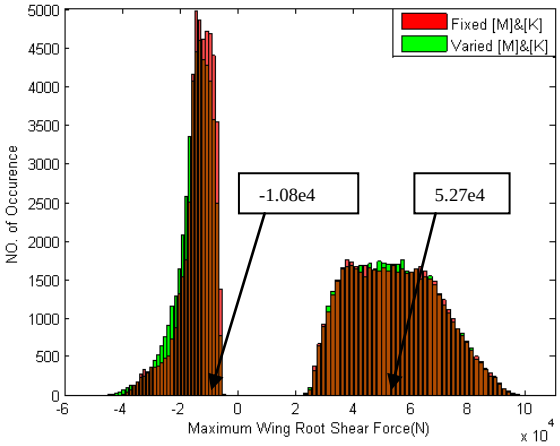

Figure 5.9. Hist of max/min wing root shear force

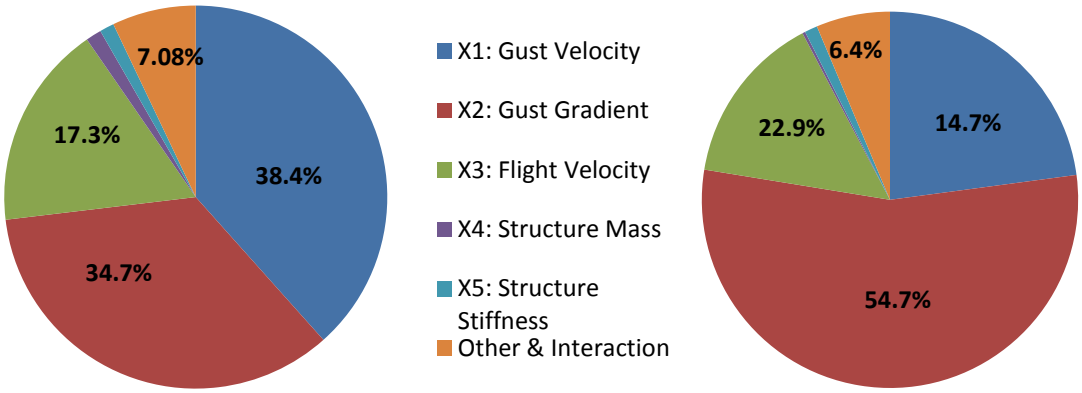

Figure 5.10. Sensitivity indices of max (left) and min (right) wing tip acceleration in pie chart

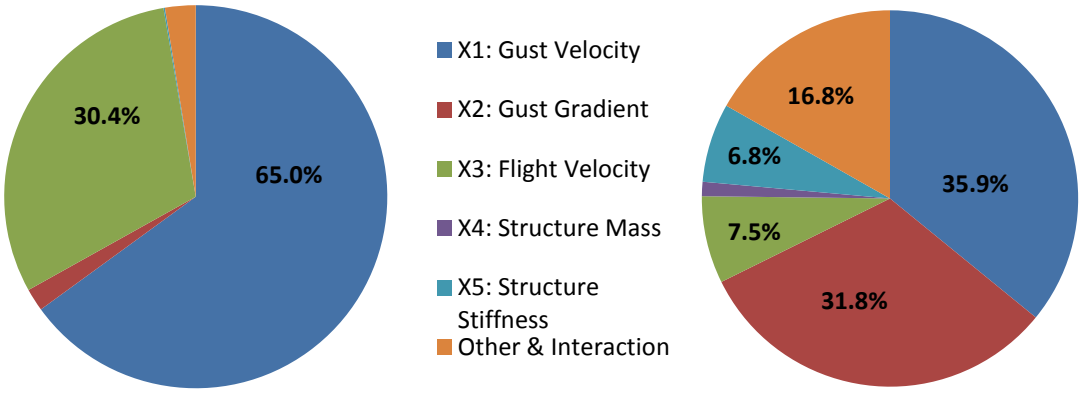

Figure 5.11. Sensitivity indices of max (left) and min (right) wing root shear force in pie chart

5.4.2 *Frequency Domain Gust Response Accounting for System Uncertainty*

To study gust response uncertainty from the PSD analysis perspective, PSD analysis of the Generic Transport Aircraft Model subject to Dryden turbulence inputs was performed for the exploratory studies presented here. According to [28], the measurement error in the coefficient of variation (COV) for gust spectrum parameters is at least 10%. Thus, to be conservative, a 15% turbulence model uncertainty is assumed in this exploratory study at given weather conditions. For the numerical example, the mean value of the scale of turbulence L is 761.5m (2500ft) and the rms value of the turbulence velocities is 30.4 m/s (100 ft/s). While the simulation capability

developed here can assign any probability distribution to any of the system's parameters, the statistical distributions of both are taken, for the results shown here, to be uniform. Structural uncertainties here are the same as in the discrete gust analysis. PSD based gust response simulations are carried out and compared with and without structural uncertainties.

50,000 simulations were performed to find the PSD of the loads when the turbulence mathematical model is subject to uncertainty. The root-mean-square (rms) value of wing tip acceleration and wing root shear force are calculated in the Monte Carlo simulations and are plotted in histogram form in Fig. 5.12, 5.13 (nominal value is shown in box), excluding and including structural uncertainty. It can be observed that whether uncertainty in the structure is modeled or not, the distributions of the rms value of the wing root shear force are similar. However, the simulations show that when uncertainty in the structure is modeled (in addition to uncertainty in the gust inputs and flight speed only), the mean value of the rms wing tip accelerations is reduced from 7855.7 to 7318.2 while the variance is doubled. This would increase the probability of wing tip acceleration reaching extreme values significantly.

Statistical sensitivity analysis was performed to rank the relative importance of system random variable to the system's output variance. The pie chart of the sensitivity indices is shown in Fig. 5.14. As expected, based on Fig. 5.12 and 5.13, the uncertainty of structural mass and stiffness have a very small influence, in the case here, on the wing root shear force. The wing tip acceleration, however, is much more affected by structural uncertainties. Fig. 5.14 supports the conclusion that regardless of structural properties the dynamic gust loads in conventional aircraft are not very sensitive, within the bounds and details of the cases studied here, to the turbulence scale. This statistical-based result is in agreement with the experimental conclusion stated in [61] p. 46-50.

Still, the present capability allows for the introduction of uncertainty that would include the scale of turbulence as one uncertain parameter among any other selection of parameters defining any continuous turbulence excitation model. The effect of statistical variation of the scale of turbulence on dynamic gust loads can, thus, be evaluated for any flexible aircraft at any flight conditions modeled by the state space models used here, and this should be useful for the analysis and design of new unconventional configurations.

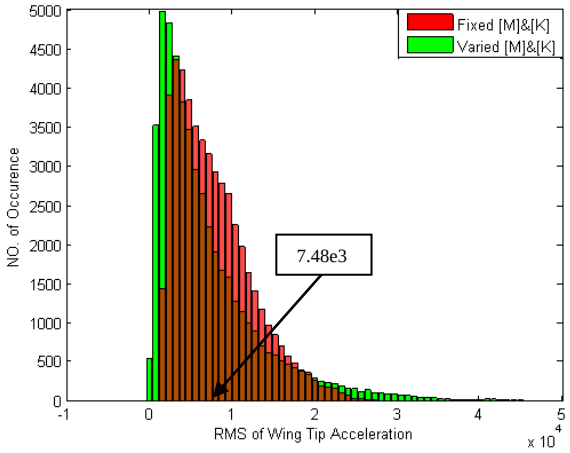

Figure 5.12. Hist of rms of wing tip acceleration in the PSD-based gust response simulation case

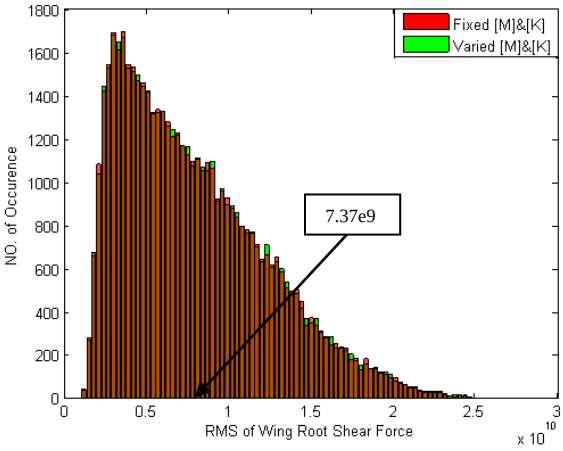

Figure 5.13. Hist of rms of wing root shear force in the PSD-based gust response simulation case

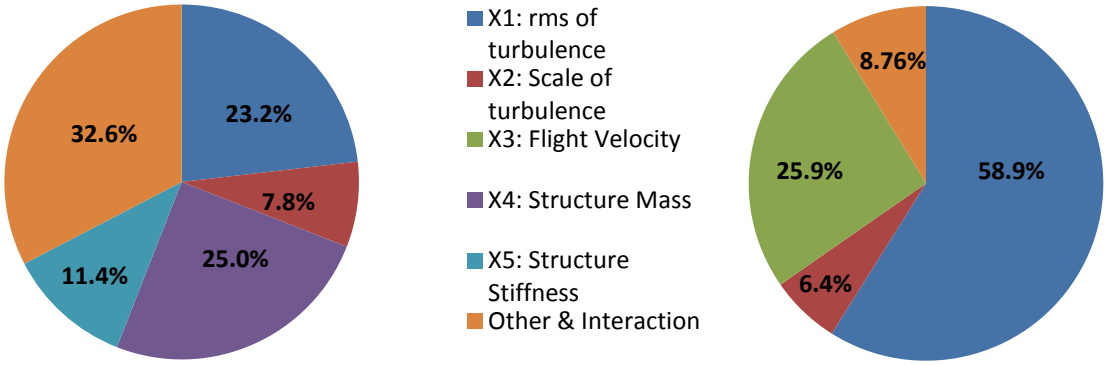

Figure 5.14. Sensitivity indices of wing tip acceleration (left) and wing root shear force (right) in the PSD-based gust response simulations

5.4.3 *Time Domain Turbulence Response with System Uncertainty*

There are two main differences between time domain and frequency domain gust response simulations. First, frequency domain turbulence simulation is based on the power distribution of the gust and airplane's response. In contrast, time domain simulation emphasizes the peak value and time evolution of the response and, therefore, a combination of critical gust-excited loads as well as structural damage tolerance or fatigue characteristic can be sought. Secondly, PSD functions in the frequency domain do not contain phase information, which indeed is a random variable in describing the response to atmospheric turbulence. The phase information may also play a significant role in controller design such as gust alleviation.

The statistical results of Monte Carlo simulations based on a discrete-gust (1-cosine) time domain approach to the gust response problem were presented earlier in the 5.4.1. To study the statistics of time domain responses to random gust inputs in the time domain, frequency domain gust models can be used to generate random gust input time series of desired statistical and PSD characteristics. The equations of motion of the deformable airplane can then be integrated in time to simulate the aeroelastic time response to such stochastic time series inputs.

In a way similar to the case of the previous examples, 15% coefficient of variation (COV) for both structure and gust spectrum parameters uncertainty were assumed. The structure random parameters were normally distributed while the gust properties were uniformly distributed. Fig. 5.15 to 5.16 show the histogram of the maximum and minimum wing tip acceleration, wing root shear force and their nominal values (shown in boxes) in the cases with and without structural uncertainty. Note that the PSD frequency domain results above are studied using their rms values while the results of the time domain responses stochastic PSD-shaped time domain inputs are studied here using their max and min response values.

The results of the sensitivity analysis are similar to those based on the PSD frequency domain turbulence response. The uncertain airframe structural mass and stiffness have small effects on the wing root shear force and wing root bending moment. However, for wing tip acceleration, both the mean value and variance accounting for an uncertain structure are larger than the fixed-structural cases and the maximum wing tip accelerations are doubled.

Statistical sensitivity analysis was performed. The pie chart of the sensitivity indices are plotted in Fig. 5.17 and 5.18. As observed before, the magnitude of rms of turbulence plays the most significant role in the variance of the system's outputs, followed by the flight velocity and scale of turbulence. The structural mass and stiffness, in the cases studied here, have only small effects on shear force, but larger effects on acceleration levels.

A relatively large portion denoted "interaction and other" (shown in orange) is observed in the pie chart. See [35] for discussion of first order and higher order sensitivity indices. In the case here "interaction and other" effects may also include the uncertainty in generating the time domain equivalent of a signal of desired PSD function.

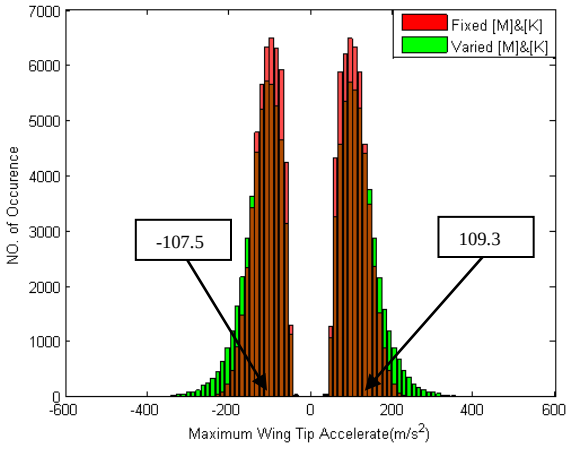

Figure 5.15. Hist of max/min wing tip acceleration. PSD-equivalent time domain approach

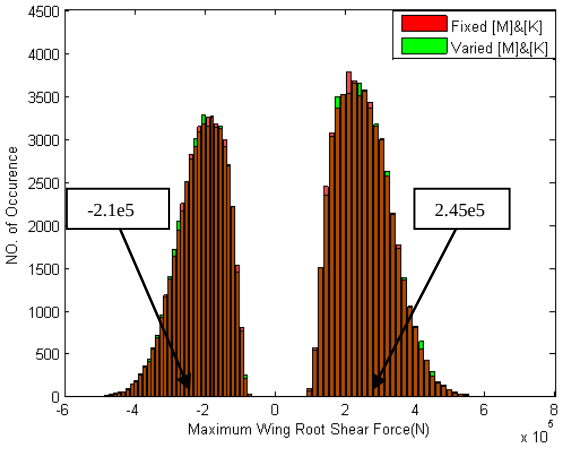

Figure 5.16. Hist of max/min wing root shear force PSD-equivalent time domain approach

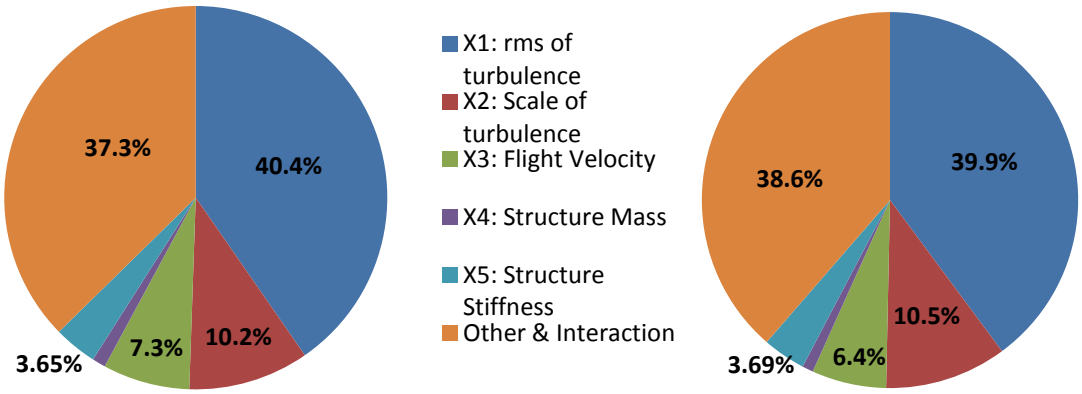

Figure 5.17. Sensitivity indices of max (left) and min (right) wing tip acceleration in pie chart PSD-equivalent time domain approach

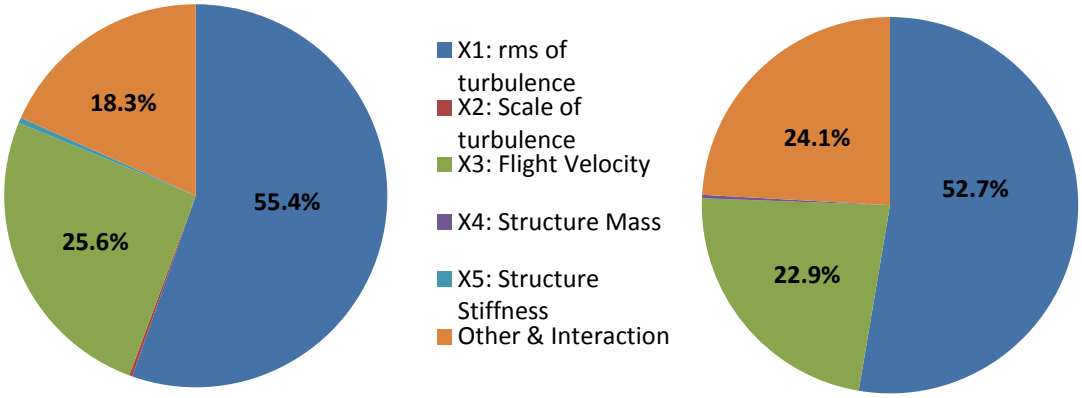

Figure 5.18. Sensitivity indices of max (left) and min (right) wing root shear force in pie chart

5.5 SUMMARY

Exploratory aeroelastic gust response Monte Carlo simulations using a mathematical model of a realistic transport airplane configuration were performed by considering uncertainties of discrete gust inputs, frequency and time domain atmospheric turbulence models, and airframe structural dynamic parameters. A University of Washington developed aeroelastic and aeroservoelastic

simulation capability for reliability analysis that allows accounting for uncertainties in all disciplines and discipline interactions affecting aeroservoelastic behavior is described and used.

Monte Carlo gust-load simulation results were obtained, using common procedures aimed at capturing worst-case load cases, with both fixed or given airframe and statistically-uncertain airframe structural dynamic properties, in simulations where the parameters that define the profile of the gust and turbulence model as well as flight speed are randomly distributed. All simulations show, in the particular case studied here, that, compared with a nominal analysis, the most critical loads are increased significantly when uncertainties are accounted for. Wing tip accelerations, on the other hand, could be doubled when structural dynamic uncertainties were included using the PSD gust loads approach. Such an increment has not been observed in the time-domain discrete 1-cosine gust analysis case.

Global sensitivity analyses are performed to rank the relative importance of input random variables to the variance of the system's output. As expected, the parameters that define the discrete gust profile have the largest influence on the internal wing-root loads, while in the case studied here – the combination of airframe type and amount of uncertainty in it - the structural uncertainty's effects are small. The structural dynamic uncertainty plays a more important role when the focus is on the wing tip acceleration in this case.

The case studies investigated here are limited and the results are not general. Aeroservoelastic response depends on the structural and aerodynamic properties of flight vehicles and external inputs that excite them in a complex and highly nonlinear way. The aeroservoelastic uncertainty analysis simulation capability described here, which was developed to tackle general problems of aeroservoelastic uncertainty in real flight vehicles, is a tool that

would allow studies of particular configurations as well as general theories and modeling techniques.

Chapter 6. CONCLUSION

The thesis presents the development of a self-contained, MATLAB based ASE simulation capability for aeroservoelastic uncertainty analysis that includes accounting for uncertainties in all disciplines and discipline interactions affecting aeroservoelastic behavior. This new capability, which can complete hundreds of thousands of aeroservoelastic Monte Carlo simulations of real aircraft within hours on commonly used, not particularly large, computer clusters, now allows probabilistic studies of such complex configuration at a scope and with depth not known before. Several statistical tools and methods have been utilized and integrated into the capability to guide the tasks such as parameter prioritization and risk mitigation. The mathematical derivations of parts of the capability are summarized in Chapter 2.

By using this capability, many innovative, novel and industrial complex aeroelasticity and aeroservoelasticity uncertainty problems have been evaluated and reported.

Chapter 3 describes a simulation-based approach to analyze the effects of uncertain component variables, emphasized on control components, on predictions of aeroservoelastic stability. The work considered the specific example of analyzing the robustness of the notch-filter aeroservoelastic approach. It showed that the component uncertainties can have considerable impact on the system stability. To demonstrate a reliability improvement procedure and reduce the system's probability of failure, statistical global sensitivity analysis was performed with respect to actuator uncertainties to identify quantitatively the actuator parameter with the highest effect on overall system stability. A redesign process was performed with new measurements added with a focus on the fluid bulk modulus, and by using Bayesian updating together with the auxiliary variable method, flutter failure reduction was achieved in a practical efficient way.

Chapter 4 introduced two aerodynamic uncertainty modeling approaches for flutter analysis: one by averaging the differences between several AIC based unsteady aerodynamic models to guide the assignment of uncertainty via the elements of the baseline AIC matrices and the other considers the flutter behavior statistics in terms of the effects of generalized aerodynamic mass, damping, stiffness and time lag uncertainty. A zonal approach, together with the global sensitivity analysis, was used to identify and rank the AIC elements that contribute to the randomness of the flutter behavior. The relative importance among the generalized aerodynamic stiffness, damping, inertia, and lag effects was also ranked.

Chapter 5 extended the reliability assessment to consider the aeroservoelastic gust response. Time domain gust response, frequency and time domain atmospheric turbulence response were included by considering the uncertainty in both gust profile and air frame. All simulations showed, in the particular case studied here that, compared with a nominal analysis the most critical loads were increased significantly when uncertainties were accounted for. Global sensitivity analyses were also performed to rank the importance of input random variable to the variance of the system's output.

The example cases investigated here were limited and the results are case dependent. What is general is the ASE uncertainty analysis simulation capability described here, which was developed to tackle general problems of aeroservoelastic uncertainty in real flight vehicles. It demonstrated that with current ASE modeling methods as well as current and emerging computer hardware, a general Monte Carlo ASE simulation approach is becoming rapidly practical as a tool that would allow studies of particular configurations as well as general theories and modeling techniques. The work is expected to make a contribution to the understanding of the propagation of uncertainty and the resulting reliability of realistic integrated aeroservoelastic

system models of the detail and complexity that allow modeling real modern aircraft. This work will, hopefully, motivate more research in the aeroservoelastic uncertainty area regarding both methods development in general and uncertainty and reliability studies of different configurations of interest.

BIBLOIOGRAPHY

[1] Livne, E., "Future of Airplane Aeroelasticity", Journal of Aircraft, Vol. 40, No. 6, November-December 2003, pp. 1066-1092, doi: 10.2514/2.7218

[2] Pettit, C.L., "Uncertainty Quantification in Aeroelasticity: Recent Results and Research Challenges", Journal of Aircraft, 2004, Vol.41, pp.1217-1229, doi: 10.2514/1.3961

[3] Dai, Y., and Yang, C., "Methods and advances in the study of aeroelasticity with uncertainties", Chinese Journal of Aeronautics, Volume 27, Issue 3, June 2014, Pages 461–474, doi:10.1016/j.cja.2014.04.016

[4] Bansal, P., Pitt, D. M., "Effects of Variations in Structural Properties of a Generic Wing on Flutter Prediction," AIAA Paper 2012-1795, , doi: 10.2514/6.2012-1795

[5] Pitt, D. M., Haudrich, D. P., Thomas M. J., Griffin, K. E., "Probabilistic Aeroelastic Analysis and Its Implications on Flutter Margin Requirements," AIAA Paper 2008-2198, doi: 10.2514/6.2008-2198

[6] Styuart, A. V., Livne, E., Demasi, L., Mor, M., "Flutter Failure Risk Assessment for Damage-Tolerant Composite Aircraft Structures," AIAA Journal, Vol. 49, No. 3, 2011, pp. 655-669, doi: 10.2514/1.J050862

[7] Bansal, P., Pitt, D. M., "Stochastic Variations in Aerodynamic Influence Coefficients (AICs): Effects on Flutter Prediction of a Generic Wing", AIAA Paper 2013-1841., doi: 10.2514/6.2013-1841

[8] Styuart, A. V., Demasi, L., Livne, E., Lin, K. Y., "Probabilistic Modeling of the Aeroelastic Life Cycle for Risk Evaluation of Composite Structures", AIAA paper 2008-2300, doi: 10.2514/6.2008-2300

[9] Millman, D.R., King, P.I., Maple, R.C., Beran, P.S., and Chilton, L.K., "Estimating the Probability of Failure of a Nonlinear Aeroelastic System", Jornal of Aircraft, Vol. 43, No. 2, March-April 2006, pp. 504-516, doi: /10.2514/1.13401

[10] Attar, P.J., and Dowell, E.H., "Stochastic Analysis of a Nonlinear Aeroelastic Model using the Response Surface Method", Journal of Aircraft, Vol. 43, No. 4, July-August 2006, pp. 1044-1052, doi: 10.2514/1.17525

[11] Danowsky, B.P., Chrstos, J. R., Klyde, D. H., Farhat, C., Brenner, M., "Evaluation of Aeroelastic Uncertainty Analysis Methods," Journal of Aircraft, Vol. 47, No. 4, 2010, pp1266-1273, doi: 10.2514/1.47118

[12] Verhoosel, C. V., Scholcz, T. P., Hulshoff, S. J., Gutierrez, M. A., "Uncertainty and Reliability Analysis of Fluid-Structure Stability Boundaries," AIAA Journal, Vol. 47, No. 1, 2009, pp. 91-104, doi: 10.2514/1.35770

[13] Borglund, D., “Robust Aeroelastic Stability Analysis Considering Frequency-Domain Aerodynamic Uncertainty,” Journal of Aircraft, Vol. 40, No. 1, 2003, pp189-193, doi: 10.2514/2.3074

[14] Moulin, B., “Modeling of Aeroservoelastic Systems with Structural and Aerodynamic Variations,” AIAA Journal, Vol. 43, No. 12, 2005, pp. 2503-2513, doi: 10.2514/1.15023

[15] Wu, Z., Dai, Y., Yang, Chao., Chen, Lei., “Aeroelastic Wind-Tunnel Test for Aerodynamic Uncertainty Model Validation”, Journal of Aircraft, Vol. 50, No. 1, 2013, pp. 47-55, doi: 10.2514/1.C031618

[16] Borglund, D., “The mu-k Method for Robust Flutter Solutions”, Journal of Aircraft, Vol. 41, No. 5, 2004, pp.1209-1216, doi: 10.2514/1.3062

[17] Borglund, D., “Robust Eigenvalue Analysis Using the Structured Singular Value: The mu-p Flutter Method,” AIAA Journal, Vol. 46, No. 11, 2008, pp. 2806-2813, doi: 10.2514/1.35859

[18] P. Mohan ‘Development and applications of a flat triangular element for thin laminated shells’ PhD Dissertation, 1997, Virginia Polytechnic Institute and State University

[19] Max Blair., A compilation of the mathematics leading to the doublet-lattice method, WL-TR-95-3022, November 1994.

[20] Britt, R.T., Jacobson, S.B., and Arthurs, T.D., "Aeroservoelastic Analysis of the B-2 Bomber", Journal of Aircraft, Vol. 37, No. 5, 2000, pp. 745-752, doi: 10.2514/2.2674

[21] Zeng, J., Wang, J., de Callafon, R., and Brenner, M., "Suppression of the Aeroelastic/Aeroservoelastic Interaction Using Adaptive Feedback Control Instead of Notching Filters", AIAA Paper 2011-6459, doi: 10.2514/6.2011-6459

[22] Livne, E., “Integrated Multidisciplinary Optimization of Actively Controlled Fiber Composite Wings”, PhD Dissertation, 1990, Department of Mechanical, Aerospace, and Nuclear Engineering, University of California, Los Angeles.

[23] Jackson, T., and Livne, E., “Integrated Aeroservoelastic Design Optimization of Actively Controlled Strain-Actuated Flight Vehicles”, AIAA Journal, Vol. 56, No. 6, 2014, pp. 1105-1123, doi: 10.2514/1.J050941

[24] Karpel, M., “Reduced-Order Models for Integrated Aeroservoelastic Optimization”, Journal of Aircraft, Vol. 36, No.1, January-February 1999, pp. 146-155

[25] Wu, S., Livne, E., “Aeroservoelastic Simulation Considering Control System Uncertainty”, AIAA Paper 2015-2056, doi. 10.2514/6.2015-2056.

[26] Karpel, M., "Procedures and Models for Aeroservoelastic Analysis and Design", ZAMM – Journal of Applied Mathematics and Mechanics / ZEITSCHRIFT FÜR ANGEWANDTE

MATHEMATIK UND MECHANIK, Volume 81, Issue 9, September 2001, Pages: 579–592.

[27] Pototzky, A., Perry, B., “New and Existing Techniques for Dynamic Loads Analyses of Flexible Airplanes”, Journal of Aircraft, Vol. 23, No. 4, 1986, pp. 340-347.

[28] Karpel, M., Moulin, B., Chen, P. C., “Dynamic Response of Aeroservoelastic Systems to Gust Excitation”, Journal of Aircraft, Vol. 42, No. 5, 2005, pp 1264-1272.

[29] Stringer, J., Hydraulic Systems Analysis, John Wiley & Sons, New York, 1976

[30] Edwards, J. W., Analysis of an Electrohydraulic Aircraft Control-Surface Servo and Comparisons with Test Results, NASA TN D-6928, August 1972.

[31] Stirling, R., "Linearized Model of the Jaguar Fly-by-Wire Actuation System," University of Bristol, Dept. of Aeronautical Engineering report no. RS/2/83, Oct. 1983.

[32] Stirling, R. and D.A. Cowling, "Implementation of Comprehensive Actuation System Models in Aeroservoelastic Analysis", Presented at the European Forum on Aeroservoelasticity and Structural Dynamics, Aachen, Germany, Report No. SDL 143, April 1989.

[33] Brenner, M.J., "Actuator and Aerodynamic Modeling for High-Angle-of-Attack Aeroservoelasticity", 1993, AIAA Paper AIAA-93-1419, doi: 10.2514/6.1993-1419

[34] Brenner, M.J., "Aeroservoelastic Modeling and Validation of a Thrust-Vectoring F/A- 18 Aircraft", NASA Technical Paper 3647, September 1996.

[35] Sobol, I.M, “Global sensitivity indices for nonlinear mathematical models and their Monte Carlo estimates”, Mathematics and Computers in Simulation, 55, 2001, pp.271-280.

[36] Allaire, D. L., Willcox, K. E., “A variance-based sensitivity index function for factor prioritization”, Reliability Engineering and System Safety, 107, 2012, pp.107-114

[37] Curran, Q. C., Willcox, K. E., “Sensitivity analysis methods for mitigating uncertainty in engineering system design”, AIAA paper 2015-0899, doi: 10.2514/6.2015-0899

[38] Lin, K.Y., Rusk, D.T., Du, J., “Equivalent Level of Safety Approach to Damage-Tolerant Aircraft Structural Design”. Journal of Aircraft, 2002, Vol.39, No. 1, pp. 167-174, doi: 10.2514/2.2911

[39] Rusk, D.T., Lin, K.Y., Swartz, D.D., Ridgeway, G.K., “Bayesian Updating of Damage Size Probabilities for Aircraft Structural Life-Cycle Management”. Journal of Aircraft, 2002, Vol.39, No. 4, pp. 689-696, doi: 10.2514/2.2983

[40] Sankararaman, S., Mahadevan, S., “Separating the contributions of variability and parameter uncertainty in probability distributions”, Reliability Engineering and System Safety, 112, 2013, pp. 187-199.

[41] Gelman, A., Garlin, J.J., Stern, H.S., Rubin, D.B., Bayesian Data Analysis, Chapman & Hall, 1995.

[42] Nannapaneni, S., Mahadevan, S., “Model and data uncertainty effects on reliability estimation”, 2015, AIAA Paper AIAA-2015-1813, doi 10.2514/6.2015-1813

[43] ZAERO Applications Manual Vol 1, Version 8.5, ZONA Technology, Inc., Scottsdale, AZ, 2008, page 3-23.

[44] Anderson, B., Moore, John., Optimal Control Linear Quadratic Methods, Dover Publications, Inc, Mineola, New York, 2007, pp 110-116

[45] Cruse, T. A., Reliability-based mechanical design, Marcel Dekker, inc. 1997

[46] Livne, E., “Integrated Aeroservoelastic Optimization: Status and Progress”, Journal of Aircraft, Vol. 36, No. 1, January-February 1999, pp. 122-145.

[47] Hajela, P., "A root locus-based flutter synthesis procedure", Journal of Aircraft, 1983, Vol. 20, No. 12, pp. 1021-1027, doi: 10.2514/3.48206

[48] Livne, E., Schmit, L.A., Friedmann, P.P., "Towards integrated multidisciplinary synthesis of actively controlled fiber composite wings", Journal of Aircraft, 1990, Vol.27, No. 12, pp. 979-992, doi: 10.2514/3.45972

[49] Oberkampf, W., and Roy, C., Verification and Validation in Scientific Computing, Cambridge University Press, 2010.

[50] Haftka, R.T., and Yates Jr., E.C., "Repetitive Flutter Calculations in Structural Design", Journal of Aircraft, Vol.13, No. 7, 1976, pp. 454-461, doi: 10.2514/3.58678

[51] Karpel, M., and Raveh, D., "Fictitious mass element in structural dynamics", AIAA Journal, Vol. 34, No. 3, 1996, pp. 607-613, doi: 10.2514/3.13111

[52] Borglund, D., Ringertz, U., "Solution of the Flutter Eigenvalue Problem with Mixed Structural/Aerodynamic uncertainty", Journal of Aircraft, 2012, Vol. 48, No. 1, pp. 343-348, doi 10.2514/1.C031204

[53] Qian, W., Huang, R., Hu, H., and Zhao, Y., "New Method of Modeling Uncertainty for Robust Flutter Suppression", Journal of Aircraft, Vol. 50, No. 3, 2013, pp. 994-999, doi: 10.2514/1.C031987

[54] Roger, K. L., "Airplane Math Modeling Methods for Active Control Design", Structural Aspects of Active Controls, AGARD-CP-228, August 1977, pp. 4-11.

[55] Potter, S., Lind, R., “Developing uncertainty models for robust flutter analysis using ground vibration test data”, AIAA Paper 2001-1585, doi: 10.2514/6.2001-1585

[56] Avalos, J., Swenson, E. D., Mignolet, M. P., and Lindsley, N. J., "Stochastic Modeling of Structural Uncertainty/Variability from Ground Vibration Modal Test Data", Journal of Aircraft, Vol. 49, No. 3, 2012. pp. 870-884

[57] Balmes, E., Wright, Jan., "GARTEUR Group on Ground Vibration Testing. Results from the Test of a Single Structure by 12 Laboratories in Europe ", 15th International Modal Analysis Conference (IMAC), 1997

[58] Zeng. J., Kukreja, S. L., "Flutter prediction for flight/wind – tunnel flutter test under atmospheric turbulence excitation", Journal of Aircraft, Vol. 50, No. 6, 2013. pp. 1696-1709

[59] Karpel, M., Moulin, B., Idan, M., "Aeroservoelastic design process using structural optimization and robust control methods", AIAA Paper 2000-4722, doi: 10.2514/6.2000-4722

[60] Federal Aviation Administration, "Aeroelastic Stability Substantiation of Transport Aircraft", Advisory Circular No. 25.629-1 B,October 27, 2014, http://www.faa.gov/documentLibrary/media/Advisory_Circular/AC_25_629-1B.pdf

[61] Hoblit, F.M., Gust Loads on Aircraft: Concepts and Applications, AIAA, Washington, D.C., 1988, ISBN 0-930403-45-2

[62] Wu, S., and Livne, E., "Probabilistic Gust Loads Analysis Accounting for Aeroservoelastic System Uncertainty", AIAA paper 2016-1483, doi: 10.2514/6.2016-1483.

[63] Wright, J.R., and Cooper, J.E., "Introduction to Aircraft Aeroelasticity and Loads", John Wiley & Sons, 2007, ISBN 978-0470-85840-0

[64] Jadic, L., Hermann, T., Hartley, D., Giri, J., "Generalized Aerodynamic Forces based on CFD and correction factor techniques for AGARD wing 445.6", AIAA paper 2001-1208, doi: 10.2514/6.2001-1208

[65] Silva, R. G. A., Mello, O. A. F., Azevedo, J. L. F., Chen, P. C., Liu, D. D., "Investigation on Transonic Correction Methods for Unsteady Aerodynamics and Aeroelastic Analyses", Journal of Aircraft, Vol. 45, No. 6 (2008), pp. 1890-1903.

[66] Pranata, B.B., Heeg, J., van Muijden, J., Eussen, B.J.G., and Wieseman, C., "Analysis of the First AIAA Aeroelastic Prediction Workshop Results of Oscillating HIRENASD Wing", NLR Report NLR-TP-2013-445, National Aerospace Laboratory, the Netherlands.

[67] Heeg, J., Chwalowski, P., Florance, J., Wiesman, C.D., Schuster, D., Perry II, B., "Overview of the Aeroelastic Prediction Workshop", AIAA Paper 2013-0783, doi: 10.2514/6.2013-783

[68] Heeg, J., Chwaloski, P., "Unsteady aerodynamic validation experiences from the Aeroelastic Prediction Workshop", AIAA Paper 2014-0203, doi: 10.2514/6.2014-0203.

[69] Pak, C.-G., "Unsteady Aerodynamic Model Tuning for Precise Flutter Prediction", Journal of Aircraft, Vol. 48, No. 6, 2011, , pp. 2178-2184, doi: 10.2514/1.C031495.

[70] Moreno, R., Knoblauch, F., Narisetti, Raj., Taylor, P. F., "A Modification to Enhanced Correction Factor Technique to Correlated With Experimental Data", AIAA paper 2015-1421, doi 10.2514/6.2015-1421

[71] Albano, E., Rodden, W. P., "A Doublet- Lattice Method for Calculating Lift Distributions on Oscillating Surfaces in Subsonic Flows", AIAA Journal, Vol. 7, No. 2, 1969, pp. 279-285.

[72] Rodden, W.P., Taylor, P.F., and McIntosh, S.C., "Further Refinement of the Subsonic Doublet Lattice Method", Journal of Aircraft, Vol. 35, No. 5, September-October 1998, pp. 720-727.

[73] Baker, M., and Rodden, W.P., "Improving the Convergence of the Doublet-Lattice Method Through Tip Corrections", Journal of Aircraft, 2001, Vol.38: 772-776, doi: 10.2514/2.2831

[74] Morino, L., "A general theory of unsteady compressible potential aerodynamics", NASA CR- 2464, December 1, 1974.

[75] Cunningham, H.J., "Steady and Unsteady Aerodynamic Forces From the SOUSSA Surface-Panel Method for a Fighter Wing With Tip Missile and Comparison With Experiment and PANAIR", NASA Technical Paper TP-2736, August 1987.

[76] Ueda, T., Dowell, E. H., "A new solution method for lifting surfaces in subsonic flow", AIAA Journal, Vol. 20, No. 3(1982), pp. 348-355, doi: 10.2514/3.7916

[77] Ueda, T., and and Dowell, E.H., "Doublet-Point Method for Supersonic Unsteady Lifting Surfaces." AIAA Journal, Vol. 22, No.2 (1984), pp. 179-186, doi: 10.2514/3.48437

[78] Chen, P. C., Lee, H.W., Liu, D. D., "Unsteady Subsonic Aerodynamics for Bodies and Wings with External Stores Including Wake Effect," Journal of Aircraft, Vol 30, No. 5, 1993, pp. 618- 628.

[79] Chen, P.C., and Liu, D., "Unsteady supersonic computations of arbitrary wing-body configurations including external stores", Journal of Aircraft, Vol. 27, No. 2 (1990), pp. 108-116, doi: 10.2514/3.45905

[80] Yurkovich, R., "Status of Unsteady Aerodynamic Prediction for Flutter of High-Performance Aircraft", Journal of Aircraft, Vol. 40, No. 5 (2003), pp. 832-842, doi: 10.2514/2.6874

[81] Wu, S., and Livne, E., "Probabilistic Gust Loads Analysis Accounting for Aeroservoelastic System Uncertainty", AIAA paper 2016-1483, doi: 10.2514/6.2016-1483.

[82] Li, W-L., and Livne, E., “Analytic Sensitivities and Approximations in Supersonic and Subsonic Wing / Control Surface Unsteady Aerodynamics”,Journal of Aircraft, Vol. 34, No. 3, pp. 370-379, May-June 1997.

[83] Karpel, M., "Design for Active Flutter Suppression and Gust Alleviation Using State Space Aeroelastic Modeling," Journal of Aircraft, Vol. 19, No. 3, 1982, pp. 221-227, doi: 10.2514/3.57379

[84] Karpel, M, "Time Domain Aeroservoelastic Weighted Unsteady Aerodynamic Forces," Journal of Guidance, Control, and Dynamics, Vol. 13, No. 1, 1990, pp. 30-37, doi: 10.2514/3.20514

[85] Chen, P.C., Gao, X., Tang, L., “Overset Field-Panel Method for Unsteady Transonic Aerodynamic Influence Coefficient Matrix Generation”, AIAA Journal, Vol. 42, No. 9 (2004), pp. 1775-1787.

[86] Yates, E. C., “AGARD Standard Aeroelastic Configurations for Dynamic Response I-Wing 445.6,” NASA TM 100492, Aug. 1987.

[87] Silva, W.A., Chwalowski, P., Perry, B.N., "Evaluation of Linear, Inviscid, Viscous, and Reduced-Order Modeling Aeroelastic Solutions of the AGARD 445.6 Wing Using Root Locus Analysis", AIAA Paper 2014-0496, doi: 10.2514/6.2014-0496.

[88] ZAERO Applications Manual Vol 1, Version 8.5, ZONA Technology, Inc., Scottsdale, AZ, page 2-1.

[89] Rumsey, C.L., Biedron, R.T., and Thomas, J.L., “CFL3D: Its History and Some Recent Applications”, NASA TM 112861, May 1997.

[90] Chen, P.C., Zhang, Z., Sengupta, A., and Liu, D.D., “Overset Euler/Boundary Layer Solver with Panel-based Aerodynamic Modeling for Aeroelastic Applications”, Journal of Aircraft, Vol. 46, No. 6, November-December 2009, pp. 2054-2068.

[91] Chen, P.C., Zhang, Z., and Livne, E., "Design Oriented Computational Fluid Dynamics Based Unsteady Aerodynamics for Flight Vehicle Shape Optimization", AIAA Journal, 2015, Vol. 53, No. 12, pp. 3603-3619. doi: 10.2514/1.J054024.

[92] Lechniak, J.A., Bhamidipati, K.K., Reasor, D.A., Margosian, K., and Pasiliao, C.L., "Comprehensive Simulation Evaluation of the AGARD 445.6 Weakened Model #3 from a Test and Evaluation Perspective", AIAA Paper 2015-0251, doi: 10.2514/6.2015-0251.

[93] Heeg, J., “Stochastic Characterization of Flutter using Historical Wind Tunnel Data”, AIAA Paper 2007-1769 doi. 10.2514/6.2007-1769.

[94] Chen, P.C., Sarhaddi, D., and Liu, D.D., "Transonic-Aerodynamic-Influence-Coefficient Approach for Aeroelastic and MDO Applications", Journal of Aircraft, Vol. 37, No. 1 (2000), pp. 85-94, doi: 10.2514/2.2565

[95] Cunningham, Jr., A., "An oscillatory kernel function method for lifting surfaces in mixed transonic flow", AIAA Paper 1974-359, do: 10.2514/6.1974-359.

[96] Mitchell, C.G.B., "Assessment of the accuracy of gust response calculations by comparison with experiments", Journal of Aircraft, 1970, Vol.7, pp. 117-125, doi: 10.2514/3.44133

[97] Coupry, G., "Effect of Spanwise Variation of Gust Velocity on Airplane Response to Turbulence", Journal of Aircraft, 1972, Vol.9, pp. 569-574, doi: 10.2514/3.59037

[98] Turner, E.J., "An Exposition on Aircraft Response to Atmospheric Turbulence Using Power Spectral Density Analysis Techniques", US Air Force Flight Dynamics Lab, AFFDL-TR-76-162, May 1977, US National Technical Information Service (NTIS) Accession Number AD-A046 108/7.

[99] Etkin, B., "Turbulent Wind and Its Effect on Flight", Journal of Aircraft, 1981, Vol.18, pp. 327-345, doi: 10.2514/3.57498

[100] Jones, J.G., "Statistical-discrete-gust method for predicting aircraft loads and dynamic response", Journal of Aircraft, 1989, Vol.26, pp. 382-392, doi: 10.2514/3.45771

[101] Perry, B., III, Woods, J.A., and Pototzky, A.S., "NASA investigation of a claimed 'overlap' between two gust response analysis methods", Journal of Aircraft, 1990, Vol.27, pp. 605-611, doi: 10.2514/3.25329

[102] Etkin, B., "Comment on 'NASA investigation of a claimed 'Overlap' between two gust response analysis methods'", Journal of Aircraft, 1992, Vol.29, pp. 741-742, doi: 10.2514/3.46239

[103] Scott, R.C., Pototzky, A.S., and Perry, B., III, "Computation of maximized gust loads for nonlinear aircraft using matched-filter-based schemes", Journal of Aircraft, 1993, Vol.30, pp. 763-768, doi: 10.2514/3.46409

[104] Jones, J.G., "Formulation of design envelope criterion in terms of deterministic spectral procedure", Journal of Aircraft, 1993, Vol.30, pp. 137-139, doi: 10.2514/3.46321

[105] Flomenhoft, H.I., "Brief history of gust models for aircraft design", Journal of Aircraft, 1994, Vol.31. pp. 1225-1227, doi: 10.2514/3.46637

[106] Fuller, J.R., "Evolution of airplane gust loads design requirements", Journal of Aircraft, 1995, Vol.32, pp. 235-246, doi: 10.2514/3.46709

[107] Scott, R.C., Pototzky, A.S., and Perry, B., III, "Matched-filter and stochastic-simulation-based methods of gust loads prediction", Journal of Aircraft, 1995, Vol.32, pp. 1047-1055, doi: 10.2514/3.46835

[108] Chen, R.P., "Statistical discrete gust-power spectral density methods overlap - Holistic proof and beyond", Journal of Aircraft, 1995, Vol.32, pp. 570-576, doi: 10.2514/3.46757

[109] Zeiler, T.A., "Matched Filter Concept and Maximum Gust Loads", Journal of Aircraft, 1997, Vol.34, pp. 101-108, doi: 10.2514/2.2141

[110] Karpel, M., Moulin, B., and Chen, P.-C., "Dynamic Response of Aeroservoelastic Systems to Gust Excitation", Journal of Aircraft, 2005, Vol.42, pp. 1264-1272, doi: 10.2514/1.6678

[111] Jones, J.G., "Measured Statistics of Multicomponent Gust Patterns in Atmospheric Turbulence", Journal of Aircraft, 2007, Vol.44, pp. 1559-1567, doi: 10.2514/1.27644

[112] Jones, J.G., "Nonlinear Aircraft Loads in Severe Atmospheric Turbulence", Journal of Aircraft, 2009, Vol.46, pp. 1627-1633, doi: 10.2514/1.42045

[113] Khodaparast, H.H., Cooper, J.E., "Rapid Prediction of Worst-Case Gust Loads Following Structural Modification", AIAA Journal, 2014, Vol.52, pp. 242-254, doi: 10.2514/1.J052031

[114] Jackson, T., "Design-Oriented Aeroservoelastic Optimization of Strain Actuated Aircraft", PhD Dissertation, 2005, Department of Aeronautics and Astronautics, University of Washington, Seattle, WA.

[115] Lind, R., and Brenner, M., Robust Aeroservoelastic Stability Analysis, Springer 1999, ISBN 1-85233-096-1.

[116] Karpel, M., Presente, E., "Structural Dynamic Loads in Response to Impulsive Excitation", Journal of Aircraft, Vol. 32, No. 4, 1995, pp. 853-861.

[117] Engelsen, F., and Livne, E., "Quadratic Stress Failure Constraints for Structures under Combined Steady and Random Excitation", AIAA Journal, Vol. 42, No. 1, January 2004, pp. 132-140

[118] Karpel, M., Shousterman, A., and Mindelis, Y., "Rigid-Body Issues in FFT-Based Dynamic Loads Analysis with Aeroservoelastic Nonlinearities", AIAA Paper 2012-1802, doi: 10.2514/6.2012-1802

[119] Wu, S., Livne, E., "Probabilistic Aeroservoelastic Reliability Assessment Considering Control System Component Uncertainty", AIAA Journal, doi: TBD

[120] Wu, S., Livne, E., "Alternative Unsteady Aerodynamic Uncertainty Modeling Approaches for Aeroservoelastic Reliability Analysis", AIAA paper 2016-1224, doi: 10.2514/6.2016-1224

[121] Wu, S., Livne, E., "Alternative Aerodynamic Uncertainty Modeling Approaches for Flutter Reliability Analysis", AIAA Journal, doi: under review

APPENDIX A. THE FINITE ELEMENT FORMULATION

Important finite elements used in the FE modeling of wing structures are membrane and plate elements (used to model skins and webs), truss Rod elements (used to model; spar and rib caps), and beam as well as rigid bar elements (used to model local reinforcements and attachment areas or link masses to the nodes they should be attached to). Beam elements are often used to model complete wings, in what is called “the stick model”, where in the case of high aspect ratio wings a detailed finite element model of the structures can be replaced by an equivalent stick model with resulting simplicity and computational efficiency.

When composite materials are used to construct airframe structures their anisotropic properties, representing the different directions of layers making the laminates used for skins, webs, and caps, must be modeled properly for both stiffness simulation and the prediction of stress related failure.

The aeroelastic simulation capability developed in this project is based on a finite element (FE) model in Matlab using three key elements: a truss element for modeling spar and rib caps, a composite triangular shell element for skins and webs and beam element for stick model. The flat triangular shell element of [18] was selected because of demonstrated good performance in linear and nonlinear cases and the availability of a detailed presentation of its development and key equations.

In order to use a finite element code (FE) correctly and efficiently, especially when optimization is involved, it is important to understand the assumptions and mathematical derivations used to develop the finite elements used in the modeling of the structures involved. Such insight into the properties of the finite elements involved would lead to efficient modeling,

efficient sensitivity analysis, efficient approximation, and efficient parametrization for optimization.

The triangular element used in this study [18] is obtained by combining the Discrete Kirchhoff Theory (DKT) Plate bending element of Batoz et al. and a membrane element with drilling degrees of freedom derived from the well known Linear Strain Triangular (LST) element. The derivation of the stiffness matrices in explicit form is not presented here and the reader should refer to [18] and the papers they are based on. A brief description of the LST and DKT elements is given first. Then the flat shell formulation for a general laminated structure is presented in detail, leading to a code that would cover deformation as well as the stress analysis for composite structures. The Mohan / Kapania element was derived for the nonlinear analysis of structures based on the updated Lagrangian formulation. This will allow extending the code in future research efforts to cover nonlinear analysis.

A.1 MEMBRANE FORMULATION

In the case of the LST element (Figure A.1), the in-plane displacement fields *u* and *v* along the local *x* and *y* axes, respectively, are represented by the standard quadratic basis in area coordinates as follows

$$u = \sum_{i=1}^{6} P_i u_i \qquad v = \sum_{i=1}^{6} P_i v_i \tag{A.1}$$

where u_i and v_i are the nodal values of the in-plane displacements and P_i are the standard quadratic shape functions in area coordinates ξ and η given by

$$\{P\} = \begin{Bmatrix} 2(1-\xi-\eta)(0.5-\xi-\eta) \\ \xi(2\xi-1) \\ \eta(2\eta-1) \\ 4\xi(1-\xi-\eta) \\ 4\xi\eta \\ 4\eta(1-\xi\eta) \end{Bmatrix} \tag{A.2}$$

The local *x*-axis is taken along the side 1-2 of the element with the origin at node 1. The local *y*-axis is perpendicular to the local *x*-axis and lies in the plane passing through the three nodes. The shape functions in $\{P\}$ are arranged in such an order that the nodes 4, 5 and 6 are at the mid point of the sides 1-2, 2-3 and 3-1, respectively.

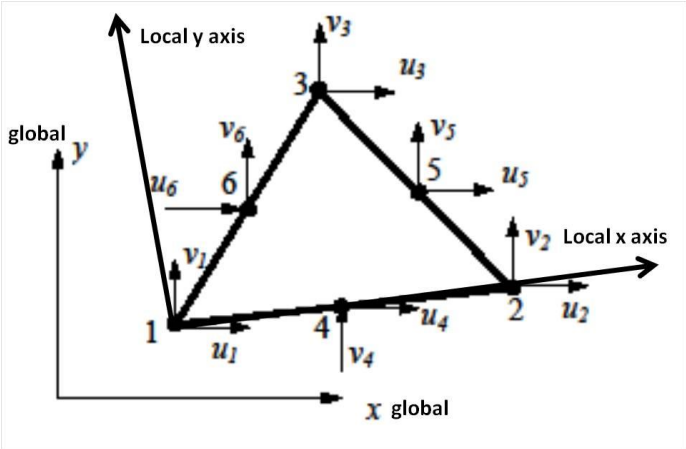

Figure A.1. The Linear Strain Triangle (LST) in local and global axes.

The normal and tangential displacements u_n and u_t along a typical element side 1-2 for example

$$u_n(s) = (1-\frac{s}{L_{12}})u_{n1} + \frac{s}{L_{12}}u_{n2} + \frac{s}{2}(1-\frac{s}{L_{12}})(\omega_2 - \omega_1) \tag{A.3}$$

$$u_t = (1-\frac{s}{L_{12}})u_{t1} + \frac{s}{L_{12}}u_{t2} \tag{A.4}$$

where *s* is the coordinate along edge 1-2, L_{12} is the length of the edge 1-2, u_{n1}, u_{t1}, u_{n2}, u_{t2} are the normal and tangential edge displacements at the nodes 1 and 2, respectively, ω_1 and ω_2 are the drilling degrees of freedom at nodes 1 and 2, respectively. The drilling degree of freedom ω is not exactly the true inplane rotation, but can be treated as the variation of the edge normal displacement u_n with respect to the edge coordinate *s* or in other words $\omega = \partial u_n / \partial s$. The true inplane rotation about the normal to the plane of the element is given by

$$\Omega = \frac{1}{2}(\partial v / \partial x - \partial u / \partial y) \tag{A.5}$$

Using straightforward algebra, it can be shown that Ω and ω are related by

$$\Omega_i - \Omega_0 = \frac{3}{4}(\omega_i - \omega_0) \tag{A.6}$$

where Ω_i are the true rotations at the vertices, Ω_0 is the average value of the true nodal rotations, and ω_i and ω_0 are the corresponding values of the drilling degree of freedom. The edge normal and tangential displacements u_n and u_t can be expressed as

$$u_n = u\cos(\gamma_{12}) + v\sin(\gamma_{12}) \tag{A.7}$$

$$u_t = -u\sin(\gamma_{12}) + v\cos(\gamma_{12}) \tag{A.8}$$

where γ_{12} is the angle between the outward normal to the edge 1-2 and the positive direction of the local *x*-axis given by

$$\cos(\gamma_{12}) = (y_2 - y_1)/L_{12}, \quad \sin(\gamma_{12}) = (x_1 - x_2)/L_{12} \tag{A.9}$$

The mi-side displacements u_4 and v_4 can now be expressed in terms of the corner displacements and rotations as

$$u_4 = \frac{1}{2}u_1 + \frac{1}{2}u_2 + (y_1 - y_2)(\omega_1 - \omega_2)/8 \tag{A.10}$$

$$v_4 = \frac{1}{2}v_1 + \frac{1}{2}v_2 + (x_2 - x_1)(\omega_1 - \omega_2)/8 \tag{A.11}$$

Similar expressions can be obtained for the mid-side displacements of the other two edges. In the updated Lagrangian formulation discussed later in this section, the in-plane strain-displacement relations are first obtained in terms of the degrees of freedom of the LST element, using the shape functions of the LST element and are expressed in terms of the degrees of the Allman element by eliminating the mid-side displacements using the expressions shown above. The triangular membrane element with drilling degrees of freedom is based on the LST element, where the displacements at the mid-nodes are eliminated and replaced by drilling rotations at the three vertices. The in-plane strain-displacement relations are presented later in this section.

A.2 PLATE BENDING FORMULATION

The formulation of the DKT plate bending element proceeds first by assuming that the transverse shear deformations are present. In other words the normal to the un-deformed middle surface of the element remains straight after deformation, but is not necessarily normal to the deformed middle surface. With this assumption and considering that the rotations of the normal are small, the displacement components *u, v, w* of any point *x, y, z* in a local coordinate system can be expressed as

$$u = z\beta_x(x, y), \quad v = z\beta_y(x, y), \quad w = w(x, y) \tag{A.12}$$

where β_x and β_y are the rotations of the normal to the undeformed middle surface in the *x*-*z* and *y*-*z* planes, respectively. The bending strains (varying linearly through the thickness) can be expressed as

$$\{\varepsilon_b\} = z\{\kappa\} \tag{A.13}$$

where $\{\kappa\}$ is the vector of curvatures given by

$$\{\kappa\} = \begin{Bmatrix} \beta_{x,x} \\ \beta_{y,y} \\ \beta_{x,y} + \beta_{y,x} \end{Bmatrix} \tag{A.14}$$

The transverse shear energy is neglected and the strain energy consisting only of the bending energy is expressed as

$$U = \frac{1}{2}\int_A \{\kappa\}^T [D]\{\kappa\}\, dA \tag{A.15}$$

where A is the area of the undeformed middle surface of the element and [D] is the standard matrix of elastic constants. Since the strain energy involves only the first derivatives of the normal rotations, the shape functions used to represent the normal rotations need to satisfy only C^0 continuity. Hence the normal rotations can be represented using the standard quadratic shape functions in area coordinates as

$$\beta_x = \sum_{i=1}^{6} \beta_{x_i} P_i \tag{A.16}$$

$$\beta_y = \sum_{i=1}^{6} \beta_{y_i} P_i \tag{A.17}$$

where β_{x_i} and β_{y_i} are the values of the normal rotations at the corners and mid-point of element edges. The nodal degrees of freedom of the Kirchhoff plate elements in general are the transverse displacement w and the slopes $\theta_x = w_{,y}$ and $\theta_y = -w_{,x}$. In order to derive the discrete equations of equilibrium in terms of the unknown nodal degrees of freedom of the element, the unknowns β_{x_i} and β_{y_i} should be expressed in terms of the nodal degrees of freedom w_i, $\theta_{x,i}$ and $\theta_{y,i}$. The 12 equations that relate the normal rotations at the corners and mid-sides to the degrees of freedom of the element are obtained by applying the discrete Kirchhoff assumptions which are explained in detail by Batozet al. After applying the discrete Kirchhoff constraints, the normal rotations β_x and β_y can be expressed as

$$\beta_x = \frac{1}{2A}\left[H_x(\xi,\eta)\right]\{a_{dkt}\} \qquad \beta_y = \frac{1}{2A}\left[H_y(\xi,\eta)\right]\{a_{dkt}\} \tag{A.18}$$

where $\{a_{dkt}\}$ is the vector of nodal degrees of freedom of the DKT element given by $\{a_{dkt}\}^T = \{w_1, \theta_{x_1}, \theta_{y_1}, w_2, \theta_{x_2}, \theta_{y_2}, w_3, \theta_{x_3}, \theta_{y_3}\}$, and $[H_x]$ and $[H_y]$ are the vectors of shape functions. These shape functions have been reordered such that the nodes 4, 5 and 6 are at the midpoints of the sides 1-2, 2-3 and 3-1, respectively. This reordering has been done in order to match the order of the nodes with that of the LST element to avoid confusion while coding.

The shape functions $[H_x]$ and $[H_y]$ after reordering are given by

$$H_x = \begin{Bmatrix} 1.5(a_4P_4 - a_6P_6) \\ b_4P_4 + b_6P_6 \\ P_1 - c_4P_4 - c_6P_6 \\ 1.5(a_5P_5 - a_4P_4) \\ b_5P_5 + b_4P_4 \\ P_1 - c_5P_5 - c_4P_4 \\ 1.5(a_6P_6 - a_5P_5) \\ b_6P_6 + b_5P_5 \\ P_1 - c_6P_6 - c_4P_4 \end{Bmatrix} \qquad H_y = \begin{Bmatrix} 1.5(d_4P_4 - d_6P_6) \\ -P_1 + e_4P_4 + e_6P_6 \\ -b_4P_4 - b_6P_6 \\ 1.5(d_5P_5 - d_4P_4) \\ -P_1 + e_5P_5 + e_4P_4 \\ -b_5P_5 - b_4P_4 \\ 1.5(d_6P_6 - d_5P_5) \\ -P_1 + e_6P_6 + e_5P_5 \\ -b_6P_6 - b_5P_5 \end{Bmatrix} \tag{A.19}$$

where

$$\begin{aligned} a_k &= -x_{ij} / l_{ij}^2 \\ b_k &= \tfrac{3}{4} x_{ij} y_{ij} / l_{ij}^2 \\ c_k &= (\tfrac{1}{4} x_{ij}^2 - \tfrac{1}{2} y_{ij}^2) / l_{ij}^2 \\ d_k &= -y_{ij} / l_{ij}^2 \\ e_k &= (\tfrac{1}{4} y_{ij}^2 - \tfrac{1}{2} x_{ij}^2) / l_{ij}^2 \\ l_{ij}^2 &= x_{ij}^2 + y_{ij}^2 \\ x_{ij} &= x_j - x_i \\ y_{ij} &= y_j - y_i \end{aligned} \tag{A.20}$$

where k = 4, 5, 6 corresponding to the sides *ij* = 1-2, 2-3, 3-1, respectively, and x_i, y_i are the nodal coordinates in the local coordinate system. As mentioned before, the derivation of the

stiffness matrix in explicit form is not presented here. Only the shape functions of the LST and DKT elements are required to derive the governing non-linear equations of equilibrium of a generally laminated shell structure, which is presented in the next section.

A.3 STATIC ANALYSIS

The equations of equilibrium governing the static response of a generally laminated structure are derived by applying the Principle of Virtual Work for a typical element using a local coordinate system as mentioned in section A.1. The Principle of Virtual Work can be expressed for a single element as follows:

$$\delta W_e = \delta W_i \tag{A.21}$$

where δW_e is the virtual work done by external forces and δW_i is the virtual work done by internal forces. The internal virtual work is given by

$$\delta W_i = \int_{C_1} \delta \{\varepsilon\}^T \{s\} \, dV \tag{A.22}$$

where *V* is the volume of the element in C_1, $\{\varepsilon\}$ is the vector of incremental Green-Lagrange strains *{s}* is the vector of Second Piola-Kirchhoff (PK2) stresses. The PK2 stresses at any time $t_1 < t < t_2$ and during the solution process can be decomposed as

$$\{s\} = \{\sigma\} + \{\Delta s\} \tag{A.23}$$

where $\{\sigma\}$ is the vector of Cauchy stresses in C_1 at time $t = t_1$ and $\{\Delta s\}$ is the vector of incremental PK2 stresses. The basic difference between the Cauchy stresses and the PK2 stresses is that the Cauchy stresses are measured in the current configuration, whereas the PK2 stresses are measured in the reference configuration. The term “current configuration” is used to denote any configuration between C_1 and C_2 obtained during the solution process. The incremental

Green-Lagrange strains and PK2 stresses in any layer *k* of a laminated structure are related by the constitutive equations given by

$$\{\Delta s\} = \left[\bar{Q}_k\right]\{\varepsilon\} \tag{A.24}$$

where $\left[\bar{Q}_k\right]$ is the standard matrix of elastic constants transformed to the local element coordinate system and is given by

$$\left[\bar{Q}_k\right] = \begin{bmatrix} c^2 & s^2 & -2cs \\ s^2 & c^2 & 2cs \\ cs & -cs & c^2 - s^2 \end{bmatrix} \begin{bmatrix} q_{11} & q_{12} & 0 \\ q_{12} & q_{22} & 0 \\ 0 & 0 & q_{66} \end{bmatrix} \begin{bmatrix} c^2 & s^2 & -2cs \\ s^2 & c^2 & 2cs \\ cs & -cs & c^2 - s^2 \end{bmatrix}^T \tag{A.25}$$

where $q_{11} = E_1/(1-\nu_{12}\nu_{21})$, $q_{12} = \nu_{12}E_2/(1-\nu_{12}\nu_{21})$, $q_{22} = E_2/(1-\nu_{12}\nu_{21})$, $q_{22} = G_{12}$, $c = \cos(\theta)$, $s = \sin(\theta)$ and E_1, E_2, ν_{12}, G_{12} are the properties in the principal material directions of the k^{th} layer and θ is the angle which the E_1 direction of the k^{th} layer makes with the local *x*-axis, measured counter clock wise from the local *x*-axis.

Assuming that the thickness of the structure and the incremental rotations are moderate, the variation of strain through the thickness can be expressed as

$$\{\varepsilon\} = \{e\} + z\{\kappa\} \tag{A.26}$$

where $\{e\}$ and $\{\kappa\}$ are the vectors of incremental membrane strains and bending strains and are given by

$$\{e\} = \begin{Bmatrix} u_{,x} + 1/2(u_{,x}^2 + v_{,x}^2 + w_{,x}^2) \\ v_{,y} + 1/2(u_{,y}^2 + v_{,y}^2 + w_{,y}^2) \\ u_{,y} + v_{,x} + u_{,x}u_{,y} + v_{,x}v_{,y} + w_{,x}w_{,y} \end{Bmatrix} \tag{A.27}$$

$$\{\kappa\} = \begin{Bmatrix} \beta_{x,x} & \beta_{y,y} & \beta_{x,y} + \beta_{y,x} \end{Bmatrix}^T \tag{A.28}$$

where *u,v,w* are the incremental displacements of the mid-plane of the element, β_x and β_y are the incremental rotations of the normal to the undeformed mid-plane in the local $x - z$ and $y - z$ planes, respectively. The internal virtual work can now be expressed as

$$\delta W_i = \int_{C_1} \delta\{\varepsilon\}^T \{s\}\, dV = \int_{C_1} \left(\delta\{e\}^T \{N\} + \delta\{\kappa\}^T \{M\}\right) dA \tag{A.29}$$

where A is the area of the mid-plane of the element in C_1, and *{N}* and *{M}* are the force and moment resultants, respectively:

$$\{N\} = \{N_1\} + \{\Delta N^m\} \tag{A.30}$$

$$\{M\} = \{M_1\} + \{\Delta M^m\} \tag{A.31}$$

where $\{N_1\}$, $\{M_1\}$ are the force and moment resultants in C_1 at time $t = t_1$, $\{\Delta N^m\}$, $\{\Delta M^m\}$ are the incremental force and moment resultants due to mechanical stresses:

$$\{N_1, M_1\} = \int_{-\frac{h}{2}}^{\frac{h}{2}} \{\sigma\}(1, z)dz \tag{A.32}$$

$$\{\Delta N^m\} = \int_{-\frac{h}{2}}^{\frac{h}{2}} \left[\bar{Q}_k\right]\left(\{e\} + z\{k\}\right)dz = [A]\{e\} + [B]\{\kappa\} \tag{A.33}$$

$$\{\Delta M^m\} = \int_{-\frac{h}{2}}^{\frac{h}{2}} \left[\bar{Q}_k\right]\left(\{e\} + z\{k\}\right)zdz = [B]\{e\} + [D]\{\kappa\} \tag{A.34}$$

where *[A], [B], [D]* are the standard matrices of elastic constants. In the present study all the area integrals are evaluated using a 3 point integration scheme in area coordinates. The integral over the thickness is computed by summing the contribution from each layer of the laminate. The first variation of the membrane strains can be expressed as

$$\{\delta e\} = \begin{cases} \delta u_{,x} + u_{,x}\delta u_{,x} + v_{,x}\delta v_{,x} + w_{,x}\delta w_{,x} \\ \delta v_{,y} + u_{,y}\delta u_{,y} + v_{,y}\delta v_{,y} + w_{,y}\delta w_{,y} \\ \delta u_{,y} + \delta v_{,y} + u_{,x}\delta u_{,y} + u_{,y}\delta u_{,x} + v_{,x}\delta v_{,y} + v_{,y}\delta v_{,x} + w_{,x}\delta w_{,y} + w_{,y}\delta w \end{cases} \tag{A.35}$$

The above equation can be rearranged as

$$\{\delta e\} = [G_1]\left\{\delta u_{,x} \quad \delta u_{,y} \quad \delta v_{,x} \quad \delta v_{,y} \quad \delta w_{,x} \quad \delta w_{,y}\right\}^T \tag{A.36}$$

where

$$[G_1] = \begin{bmatrix} 1+u_{,x} & 0 & v_{,x} & 0 & w_{,x} & 0 \\ 0 & u_{,y} & 0 & 1+v_{,y} & 0 & w_{,y} \\ u_{,y} & 1+u_{,x} & 1+v_{,y} & v_{,x} & w_{,y} & w_{,x} \end{bmatrix} \tag{A.37}$$

The in-plane displacements u and v can be expressed in terms of the nodal quantities as

$$\begin{Bmatrix} u \\ v \end{Bmatrix} = \begin{bmatrix} \{P\}^T & 0 \\ 0 & \{P\}^T \end{bmatrix} \{a_{lst}\} \tag{A.38}$$

where $\{a_{lst}\}$ is the vector of nodal degrees of freedom of the LST element given by $\{a_{lst}\} = \{u_1 \quad u_2 \quad u_3 \quad u_4 \quad u_5 \quad u_6 \quad v_1 \quad v_2 \quad v_3 \quad v_4 \quad v_5 \quad v_6\}$ and $\{P\}$ is the vector of quadratic shape functions in area co-ordinates given by above. The derivatives of the in-plane displacements are given by

$$\begin{Bmatrix} u_{,x} \\ u_{,y} \\ v_{,x} \\ v_{,y} \end{Bmatrix} = \begin{bmatrix} \{P_{,x}\}^T & 0 \\ \{P_{,y}\}^T & 0 \\ 0 & \{P_{,x}\}^T \\ 0 & \{P_{,y}\}^T \end{bmatrix} [T_{lst}]\{a\} = [B_{lst}]\{a\} \tag{A.39}$$

where $\{P_{,x}\}$ and $\{P_{,y}\}$ are the vectors of derivatives of the shape functions with respect to the local *x* and *y* co-ordinates, respectively, and are given by

$$\{P_{,x}\} = \frac{1}{2A}\left(b_2\{P_{,\xi}\} + b_3\{P_{,\eta}\}\right) \tag{A.40}$$

$$\{P_{,y}\} = \frac{1}{2A}\left(c_2\{P_{,\xi}\} + c_3\{P_{,\eta}\}\right) \tag{A.41}$$

where $2A = b_2c_3 - c_2b_3$, $b_2 = y_3 - y_1$, $b_3 = y_1 - y_2$, $c_2 = x_1 - x_3$, $c_3 = x_2 - x_1$. The matrix $[T_{lst}]$ is used to express the nodal degrees of the LST element $[a_{lst}]$ in terms of the nodal degrees of freedom of the shell element $\{a\}$ as $\{a_{lst}\} = [T_{lst}]\{a\}$, where

$$\{a\} = \{u_1 \quad v_1 \quad w_1 \quad \theta_{x_1} \quad \theta_{y_1} \quad \theta_{z_1} \quad u_2 \quad v_2 \quad w_2 \quad \theta_{x_2} \quad \theta_{y_2} \quad \theta_{z_2} \quad u_3 \quad v_3 \quad w_3 \quad \theta_{x_3} \quad \theta_{y_3} \quad \theta_{z_3}\} \tag{A.42}$$

The transformation matrix $[T_{lst}]$ is given by

$$[T_{lst}]=\begin{bmatrix}
1 & 0 & 0 & 0 & 0 & 0 & 0 & 0 & 0 & 0 & 0 & 0 & 0 & 0 & 0 & 0 & 0 & 0\\
0 & 0 & 0 & 0 & 0 & 0 & 1 & 0 & 0 & 0 & 0 & 0 & 0 & 0 & 0 & 0 & 0 & 0\\
0 & 0 & 0 & 0 & 0 & 0 & 0 & 0 & 0 & 0 & 0 & 0 & 1 & 0 & 0 & 0 & 0 & 0\\
0.5 & 0 & 0 & 0 & 0 & b_3/8 & 0.5 & 0 & 0 & 0 & 0 & -b_3/8 & 0 & 0 & 0 & 0 & 0 & 0\\
0 & 0 & 0 & 0 & 0 & 0 & 0.5 & 0 & 0 & 0 & 0 & b_1/8 & 0.5 & 0 & 0 & 0 & 0 & -b_1/8\\
0.5 & 0 & 0 & 0 & 0 & -b_2/8 & 0 & 0 & 0 & 0 & 0 & 0 & 0.5 & 0 & 0 & 0 & 0 & b_2/8\\
0 & 1 & 0 & 0 & 0 & 0 & 0 & 0 & 0 & 0 & 0 & 0 & 0 & 0 & 0 & 0 & 0 & 0\\
0 & 0 & 0 & 0 & 0 & 0 & 0 & 1 & 0 & 0 & 0 & 0 & 0 & 0 & 0 & 0 & 0 & 0\\
0 & 0 & 0 & 0 & 0 & 0 & 0 & 0 & 0 & 0 & 0 & 0 & 0 & 1 & 0 & 0 & 0 & 0\\
0 & 0.5 & 0 & 0 & 0 & c_3/8 & 0 & 0.5 & 0 & 0 & 0 & -c_3/8 & 0 & 0 & 0 & 0 & 0 & 0\\
0 & 0 & 0 & 0 & 0 & 0 & 0 & 0.5 & 0 & 0 & 0 & c_1/8 & 0 & 0.5 & 0 & 0 & 0 & -c_1/8\\
0 & 0.5 & 0 & 0 & 0 & -c_2/8 & 0 & 0 & 0 & 0 & 0 & 0 & 0 & 0.5 & 0 & 0 & 0 & c_2/8
\end{bmatrix} \tag{A.43}$$

In the case of the DKT element the transverse displacement *w* is not defined explicitly over the interior of the element. In area coordinates, *w* is expressed as $w(\xi,\eta)=(1-\xi-\eta)w_1+\xi w_2+\eta w_3$ from which the derivatives can be obtained as

$$\begin{Bmatrix} w_{,x} \\ w_{,y} \end{Bmatrix}=\frac{1}{2A}\begin{bmatrix} -b_2-b_3 & b_2 & b_3 \\ -c_2-c_3 & c_2 & c_3 \end{bmatrix}[T_w]\{a\}=[B_w]\{a\} \tag{A.44}$$

where $[T_w]$ is used to express $\{w_1 \quad w_2 \quad w_3\}^T$ in terms of $\{a\}$ as $\{w_1 \quad w_2 \quad w_3\}^T=[T_w]\{a\}$. The transformation matrix $[T_w]$ is made of zeroes and ones, the determination of which is straightforward. The first variation of the membrane strains can be expressed as

$$\{\delta e\}=[G_1][G_2]\{\delta a\} \tag{A.45}$$

where $[G_2]$ is a matrix of size 6x18 with the first 4 rows made of $[B_{lst}]$ and the last 2 rows made of $[B_w]$. The first variation of the bending strains can now be expressed as

$$\{\delta\kappa\}=\frac{1}{2A}\begin{bmatrix} b_2H^T_{x,\xi}+b_3H^T_{x,\eta} \\ c_2H^T_{y,\xi}+c_3H^T_{y,\eta} \\ c_2H^T_{x,\xi}+c_3H^T_{x,\eta}+b_2H^T_{y,\xi}+b_3H^T_{y,\eta} \end{bmatrix}[T_{dkt}]\{\delta a\}=[B_{dkt}]\{\delta a\} \tag{A.46}$$

where $H_{x,\xi}$, $H_{x,\eta}$, $H_{y,\xi}$, $H_{y,\eta}$ are the derivatives of the shape functions with respect to the area coordinates.

The matrix $[T_{dkt}]$ which is used to expresses $[a_{dkt}]$ in terms of $[a]$ as $[a_{dkt}]=[T_{dkt}]\{a\}$, is made up of zeroes and ones.

The external virtual work can be expressed as

$$\delta W_e = \{\delta a\}^T \{f\} \tag{A.47}$$

where {*f*} is the element external force vector. The equations of equilibrium at the element level can be expressed as

$$\{g\} = \{q\} - \{f\} = 0 \tag{A.48}$$

where $\{q\}$ is the element internal force vector given by

$$\{q\} = \int_{C_1} \left([G_2]^T [G_1]^T \{N\} + [B_{dkt}]^T \{M\} \right) dA \tag{A.49}$$

The element internal and external force vectors thus obtained in the element local co-ordinates are converted to the global co-ordinates using the standard coordinate transformation and are assembled to obtain the global internal force vector q and external force vector f. The non-linear governing equations of equilibrium of the entire finite element model in the global Cartesian co-ordinate system at any time t can be written as $g_t = q_t - f_t = 0$, where g is the residue or the imbalance between the internal and external forces.

The non-linear equations of equilibrium can be solved using the Newton-Raphson method, an iterative or step-by-step process in which a linearized form of the equilibrium equations is solved in each step. Assuming that a known equilibrium configuration exists at some time t_1, the equations of equilibrium at some time $t_1 + \Delta t$ can be linearized using the truncated Taylor series expansion about the known configuration at time t_1 as

$$g_{t_1+\Delta t} = q_{t_1} + \left(\frac{\partial q}{\partial a} \right)_{t_1} \delta a - f_{t_1+\Delta t} = q_{t_1} + [K]\delta a - f_{t_1+\Delta t} = 0 \tag{A.50}$$

where [K] is the global tangent stiffness matrix which is obtained by transforming the local element stiffness matrices [k] and assembling them in the standard way. The derivatives of $\{N\}$ and $\{M\}$ with respect to $\{a\}$ can be readily obtained as

$$\begin{aligned}\frac{\partial\{N\}}{\partial\{a\}} &= [A][G_1][G_2]+[B][B_{dkt}]\\ \frac{\partial\{M\}}{\partial\{a\}} &= [B][G_1][G_2]+[D][B_{dkt}]\end{aligned} \tag{A.51}$$

The variation of the product $[G_2]^T[G_1]^T\{N\}$ is given by

$$\delta\left([G_2]^T[G_1]^T\{N\}\right)=[G_2]^T\left(\delta[G_1]^T\right)\{N\}+[G_2]^T[G_1]^T\delta\{N\} \tag{A.52}$$

Using the special property of the matrix $[G_1]$, the product $\left(\delta[G_1]^T\right)\{N\}$ can be expressed as

$$\left(\delta[G_1]^T\right)\{N\}=\begin{bmatrix}\hat{N} & 0 & 0\\ 0 & \hat{N} & 0\\ 0 & 0 & \hat{N}\end{bmatrix}[G_2]\delta\{a\} \tag{A.53}$$

where n_x, n_y and n_{xy} are the components of $\{N\}$ and $\hat{N}=\begin{bmatrix}n_x & n_{xy}\\ n_{xy} & n_y\end{bmatrix}$

The element tangent stiffness matrix [k] can now be expressed as

$$\begin{aligned}[k]=\int_{C_1}&([G_2]^T[G_1]^T[A][G_1][G_2]+[B_{dkt}]^T[D][B_{dkt}]+[B_{dkt}]^T[B][G_1][G_2])\\ &+[G_2]^T[G_1]^T[B][B_{dkt}]+[G_2]^T\begin{bmatrix}\hat{N} & 0 & 0\\ 0 & \hat{N} & 0\\ 0 & 0 & \hat{N}\end{bmatrix}[G_2])dA\end{aligned} \tag{A.54}$$

Since the derivation for the truss element FEM formulation can be found in all the fundamental finite element books, this report does not include the derivation of such element.

APPENDIX B. UNSTEADY AERODYNAMICS – THE DOUBLET LATTICE METHOD

Aerodynamic compressibility is an important factor in the flutter of high speed air vehicle. It is impossible to solve these equations without the help of high speed computer. The kernel-function and doublet-lattice method (DLM) were developed along with improvements in digital computer technology. During the past two decades, the flow around more complicated shape of objects has been becoming tractable by CFD. However, the high cost and technical complications associated with non-linear CFD as well as the proven success of the doublet-lattice method plus deep understanding of the limitations of DLM, leads to DLM is still being used almost exclusively for the subsonic flutter clearance of airplanes being designed today.

Since the research focus on the reliability and variability of the parameter, it was necessary to develop an open source code which would allow access to all aerodynamic terms and parameters. Current commercial codes are packaged as black boxes, which makes it almost impractical to add uncertainty effects to all unsteady aerodynamic terms. For this research we developed our own unsteady aerodynamic code based on doublet lattice method.

B.1 LINEARIZED SMALL DISTURBANCE EQUATION

We start from the linearized small disturbance equation that read

$$\left(1-M^2\right)\Phi_{xx}+\Phi_{yy}+\Phi_{zz}-2\left(\frac{M}{a_0}\right)\Phi_{xt}-\left(\frac{1}{a_0^2}\right)\Phi_{tt}=0 \tag{B.1}$$

where

M is the free stream Mach number

Φ is the total velocity potential

a_0 is the steady speed of sound

We also denote $\beta = \sqrt{\left(1-M^2\right)}$, it will be used widely in the following derivation.

The unknown Φ, is divided into two component, a steady part (bar) and small disturbance part (tilde) which is time dependent.

$$\Phi\left(x,y,z,t\right) = \bar{\phi}\left(x,y,z\right) + \tilde{\phi}\left(x,y,z,t\right) \tag{B.2}$$

Similarly, air pressure and density can be written as

$$P\left(x,y,z,t\right) = \bar{p}\left(x,y,z\right) + \tilde{p}\left(x,y,z,t\right) \tag{B.3}$$

$$\rho\left(x,y,z,t\right) = \bar{\rho}\left(x,y,z\right) + \tilde{\rho}\left(x,y,z,t\right) \tag{B.4}$$

The speed of sound is assumed time invariant in the linearization process

$$a\left(x,y,z,t\right) = \bar{a}\left(x,y,z\right) = a_0 \tag{B.5}$$

Plug Eq(B.2)-Eq(B.5) into Eq(B.1), we can get the unsteady linearized small disturbance equation

$$\left(1-M^2\right)\tilde{\phi}_{xx} + \tilde{\phi}_{yy} + \tilde{\phi}_{zz} - 2\left(\frac{M}{a_0}\right)\tilde{\phi}_{xt} - \left(\frac{1}{a_0^2}\right)\tilde{\phi}_{tt} = 0 \tag{B.6}$$

Introducing the Bernoulli's equation

$$\frac{\partial\phi}{\partial t} + \frac{q^2}{2} + \int\frac{dp}{\rho} = 0 \tag{B.7}$$

the relationship between pressure and velocity potential can be shown as

$$\left(p - p_0\right) = -\rho_0\left(\tilde{\phi}_t + U\tilde{\phi}_x\right) \tag{B.8}$$

where U is x axis velocity components, p_0 is the pressure at the far field. Eq (B.8) can be solved by using method of characteristics. The desired result can be written as

$$\tilde{\phi}\left(x,y,z,t\right) = \frac{1}{\rho_0 U}\int_{-\infty}^{x}\left[p\left[\lambda,y,z,t-\frac{x-\lambda}{U}\right] - p_0\right]d\lambda \tag{B.9}$$

The reader should realize that λ is the dummy variable of integration.

B.2 UNSTEADY BOUNDARY CONDITION

It can be shown that the solution to the linearized small disturbance equation is unique when given the appropriate boundary conditions. A time variant surface in three space can be described by the

$$F\left(x,y,z,t\right)=0 \tag{B.10}$$

The inviscid fluid flow boundary condition requires the flow to be tangential only to a moving body at all times. In other words, all the flow normal to the surface should be zeros. Mathematically, this is described by

$$\frac{\partial F}{\partial t}+\vec{V}\bullet\nabla F=0 \tag{B.11}$$

The function describing of the surface of the wing is written as $F=F_w\left(x,y,z,t\right)$, this function is now constrained to two uncoupled components, the deformation of midplane h_m and the thickness envelope h_t about the undeformed midplane. The *F* can be defined as

$$F_w\left(x,y,z,t\right)=z-h_m\left(x,y,t\right)\pm h_t\left(x,y,t\right)=0 \tag{B.12}$$

The aerodynamic velocity vector is described as

$$\vec{V}=\left(U+u\right)\vec{i}+v\vec{j}+w\vec{k} \tag{B.13}$$

Substitute Eq(12) and (13) into Eq(11) and drop the nonlinear terms

$$w=\frac{\partial h}{\partial t}+U\frac{\partial h}{\partial x} \tag{B.14}$$

where $h=h_m\pm h_t$.

B.3 SOLUTION TO THE LINEARIZED SMALL DISTURBANCE EQUATION

Blair has shown that although the fundamental source solution can be used as an elementary solution to the aerodynamic potential equation, it turns out, that a single source sheet cannot generate a potential difference across the (*x*,*y*) plane. Therefore, no pressure or lift can be

generated. Instead of using source sheet, the source doublet was utilized to solve the velocity potential equation.

Without derivation, the fundamental source solution to Eq(B.6) is given by the following simple formula.

$$\phi_s\left(x,y,z,\xi,\eta,\zeta,t\right)=\left[\frac{1}{\bar{R}}\right]f\left(t-\tau\right) \tag{B.15}$$

This is the formula for the potential at coordinate (*x*,*y*,*z*) due to single point source at coordinate $\left(\xi,\eta,\zeta\right)$. Where $f\left(t-\tau\right)$ is the strength of the source pulse, τ is the time delay and $\bar{R}$ is the radial measure and defined as

$$\bar{R}=\left[\left(x-\xi\right)^2+\beta^2\left(y-\eta\right)^2+\beta^2\left(z-\zeta\right)^2\right]^{1/2} \tag{B.16}$$

Although it can be shown that a source doublet can solve the velocity potential with input of wing deformation *h*, the pressure *p* need to be computed later in a second step. It is common to avoid the intermediate step of the solving for the velocity potential and solve for pressure directly with the introduction of the pressure potential and subsequently the acceleration potential. Therefore, we skip the further explanation of the source doublet which was utilized to solve the velocity potential equation.

B.4 THE ACCELERATION POTENTIAL

We now start at the small disturbance equation in Eq(B.6), which can be also written as

$$\beta^2\tilde{\phi}_{xx}+\tilde{\phi}_{yy}+\tilde{\phi}_{zz}-2\left(\frac{U}{a_0^2}\right)\tilde{\phi}_{xt}-\left(\frac{1}{a_0^2}\right)\tilde{\phi}_{tt}=0 \tag{B.17}$$

Differentiate with respect to *t* and then *x*, multiply by ρ_0 and $\rho_0 U$ respectively and add them together we arrive at the equation

$$\beta^2\rho_0\left(\tilde{\phi}_t+U\tilde{\phi}_x\right)_{xx}+\rho_0\left(\tilde{\phi}_t+U\tilde{\phi}_x\right)_{yy}+\rho_0\left(\tilde{\phi}_t+U\tilde{\phi}_x\right)_{zz}$$
$$-\left[\frac{2U}{a^2}\right]\rho_0\left(\tilde{\phi}_t+U\tilde{\phi}_x\right)_{xt}-\left[\frac{1}{a^2}\right]\rho_0\left(\tilde{\phi}_t+U\tilde{\phi}_x\right)_{tt}=0 \tag{B.18}$$

Substitute Eq(B.8) into Eq(B.18), the pressure potential equation can be expressed as

$$\beta^2 p_{xx}+p_{yy}+p_{zz}-2\left(\frac{U}{a_0^2}\right)p_{xt}-\left(\frac{1}{a_0^2}\right)p_{tt}=0 \tag{B.19}$$

The form of Eq(B.19) is identical to the form of Eq(B.17) mathematically. Therefore, the elementary solution to small disturbance equation (Eq B.15) is also the solution to Eq(B.19). The elementary pressure source equation is

$$p_s=\left[\frac{1}{\bar{R}}\right]f\left(t-\tau\right) \tag{B.20}$$

where $\tau=\dfrac{-M(x-\xi)+\bar{R}}{a\beta^2}$, $\bar{R}=\left[\left(x-\xi\right)^2+\beta^2\left(y-\eta\right)^2+\beta^2\left(z-\zeta\right)^2\right]^{1/2}$.

Since we have restricted to harmonics in time, variable time dependency is then replaced by a constant frequency dependency. Thus, Eq(B.20) for a pressure source p_s with strength A takes the complex form $p_s e^{i\omega t}$.

$$p_s=\left[\frac{A}{\bar{R}}\right]e^{i\omega(t-\tau)}=\left[\frac{Ae^{-i\omega\tau}}{\bar{R}}\right]e^{i\omega t}=\bar{p}_s e^{i\omega t} \tag{B.21}$$

$$\bar{p}_s\left(x,y,z\right)=\frac{Ae^{-i\omega\tau}}{\bar{R}}=\frac{A}{\bar{R}}\exp\left[\frac{i\omega}{a\beta^2}\left(M\left(x-\xi\right)-\bar{R}\right)\right] \tag{B.22}$$

Differentiate Eq(B.21) with respect to *z* in order to obtain the definition for the pressure doublet, it will be called the acceleration potential ψ. Define the relation between pressure *p* and ψ as

$$p=\rho_0\psi \tag{B.23}$$

Then

$$\psi=\left[\frac{1}{\rho_0}\right]\frac{\partial}{\partial z}\left[p_s\right]=\left[\frac{1}{\rho_0}\right]\frac{\partial}{\partial z}\left[\bar{p}_s\right]e^{i\omega t}=\left[\frac{1}{\rho_0}\right]\bar{\psi}\left(x,y,z\right)e^{i\omega t} \tag{B.24}$$

where

$$\bar{\psi}(x,y,z)=\frac{\partial}{\partial z}[\bar{p}_s]=\frac{\partial}{\partial z}\left[\frac{A}{\bar{R}}\exp\left[\frac{i\omega}{a\beta^2}\left(M(x-\xi)-\bar{R}\right)\right]\right] \tag{B.25}$$

Eq(B.25) is now an elementary solution to Eq(B.19).

By taking the derivative with respect to z in Eq(B.25)

$$\frac{\partial}{\partial z}\bar{R}=\frac{\beta^2(z-\zeta)}{\bar{R}} \tag{B.26}$$

$$\frac{\partial}{\partial z}\left(\frac{1}{\bar{R}}\right)=\frac{-\beta^2(z-\zeta)}{\bar{R}^3} \tag{B.27}$$

Eq(B.25) can be rewritten as

$$\bar{\psi}(x,y,z)=A\beta^2(z-\zeta)\left[\frac{-i\omega}{\bar{R}^2}-\frac{1}{\bar{R}^3}\right]\exp\left[\frac{i\omega}{a\beta^2}\left(M(x-\xi)-\bar{R}\right)\right] \tag{B.28}$$

This formula describe the pressure ψ at coordinate (*x,y,z*) due to a pressure doublet at coordinate (ξ,η,ζ), integrate Eq(B.28) to get the total pressure due to a continuum of doublets.

$$\bar{\psi}(x,y,z)=\beta^2 z\int_s A(\xi,\eta)\left[\frac{-i\omega}{\bar{R}^2}-\frac{1}{\bar{R}^3}\right]\exp\left[\frac{i\omega}{a\beta^2}\left(M(x-\xi)-\bar{R}\right)\right]d\xi d\eta \tag{B.29}$$

By using the fact $A=\frac{\Delta\bar{p}}{4\pi\rho}$, Eq(B.29) can be further reduced to

$$\bar{\psi}(x,y,z)=\frac{\beta^2 z}{4\pi\rho}\int_s \Delta\bar{p}(\xi,\eta)\left[\frac{-i\omega}{\bar{R}^2}-\frac{1}{\bar{R}^3}\right]\exp\left[\frac{i\omega}{a\beta^2}\left(M(x-\xi)-\bar{R}\right)\right]d\xi d\eta \tag{B.30}$$

Combining Eq(B.8) and Eq(B.23), we can get the relation between acceleration potential and velocity potential.

$$\bar{\psi}(x,y,z)=-U\bar{\phi}_x(x,y,z)-i\omega\bar{\phi}(x,y,z) \tag{B.31}$$

Inverse Eq(B.31)

$$\bar{\phi}(x,y,z)=\frac{-1}{U}\exp\left[\frac{-i\omega x}{U}\right]\int_{-\infty}^{x}\exp\left[\frac{i\omega\lambda}{U}\right]\bar{\psi}(\alpha,y,z)\,d\alpha \tag{B.32}$$

Substitute Eq(B.32) into Eq(B.30)

$$\bar{\phi}(x,y,z)=\frac{-1}{U}\exp\left[\frac{-i\omega x}{U}\right]\int_{-\infty}^{x}\exp\left[\frac{i\omega\lambda}{U}\right]\bar{\psi}(\alpha,y,z)\,d\alpha \tag{B.33}$$

Substitute Eq(B.25) into Eq(B.33),

$$\bar{\phi}(x,y,z)=\frac{-A}{U}\exp\left[\frac{-i\omega x}{U}\right]\int_{-\infty}^{x}\exp\left[\frac{i\omega\lambda}{U}\right]\frac{\partial}{\partial z}\left[\frac{1}{\bar{R}}\exp\left[\frac{i\omega}{a\beta^2}\left(M(x-\xi)-\bar{R}\right)\right]\right] \tag{B.34}$$

Take derivative of $\bar{\phi}(x,y,z)$ with respect to *z*, the downwash *w* can be computed as

$$\bar{w}(x,y,z)=\frac{-A}{U}\frac{\partial^2}{\partial z^2}\left[\exp\left[\frac{-i\omega(x-\xi)}{U}\right]\int_{-\infty}^{x-\xi}\frac{1}{\bar{R}}\exp\left[i\omega\left(\frac{\lambda}{U}+\frac{M\lambda}{a\beta^2}-\frac{\bar{R}}{a\beta^2}\right)\right]d\right. \tag{B.35}$$

Similar as Eq(B.29), the downwash due to a continuous sheet of doublets in the identical sense can be finally written as

$$\bar{w}(x,y,z)=\left[\frac{-1}{4\pi\rho U}\right]\iint_{s}\Delta\bar{p}K\left((x-\xi),(y-\eta),z\right)d\xi d\eta \tag{B.36}$$

where

$$K(x_0,y_0,z_0)=\exp\left(\frac{-i\omega x_0}{U}\right)\frac{\partial^2}{\partial z^2}\left[\int_{-\infty}^{x_0}\frac{1}{\bar{R}}\exp\left[\frac{i\omega}{U\beta^2}\left(\lambda-M\bar{R}\right)\right]d\lambda\right] \tag{B.37}$$

Eq(37) is known as the Kernel Function.

B.5 KERNEL FUNCTION

Similarly as previous section, we skip the detailed derivation, only listing the key equations. For the kernel function for a nonplanar surface in the form

$$K=e^{-(i\omega x_0/U)}\left(K_1T_1+K_2T_2\right)/r_1^2 \tag{B.38}$$

where

$$T_1=\cos\left[\gamma(s)-\gamma(\sigma)\right] \tag{B.39}$$

$$T_2=\left\{\frac{z_0}{r_1}\cos\left[\gamma(s)\right]-\frac{y_0}{r_1}\sin\left[\gamma(s)\right]\right\}\times\left\{\frac{z_0}{r_1}\cos\left[\gamma(\sigma)\right]-\frac{y_0}{r_1}\sin\left[\gamma(\sigma)\right]\right\} \tag{B.40}$$

$$r_1 = \left(y_0^2 + z_0^2\right)^{1/2},\ x_0 = x - \xi,\ y_0 = y - \eta,\ z_0 = z - \zeta$$

The coordinate of system is illustrated in Figure B.1

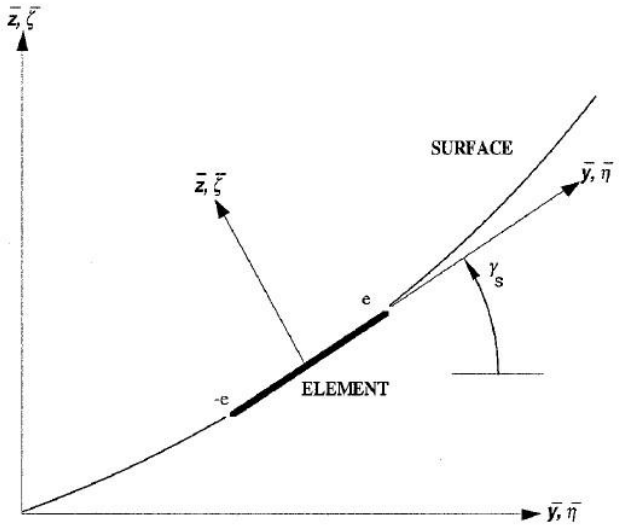

Figure B.1. Kernel function coordinate definition

Landahl has simplified the forms of K_1 and K_2 where

$$K_1 = -I_1 - \left[\frac{Mr_1}{R}\right]\left[\frac{\exp\left(-ik_1u_1\right)}{\left(1+u_1^2\right)^{1/2}}\right] \tag{B.41}$$

$$K_2 = 3I_2 + \frac{ik_1M^2r_1^2}{R^2}\cdot\frac{\exp\left(-ik_1u_1\right)}{\left(1+u_1^2\right)^{1/2}} + \frac{Mr_1}{R}\left[\left(1-u_1^2\right)\frac{\beta^2r_1^2}{R^2} + 2 + \frac{Mr_1u_1}{R}\right]\frac{\exp\left(-ik_1u_1\right)}{\left(1+u_1^2\right)^{3/2}} \tag{B.42}$$

where

$$I_1 = \int_{u_1}^{\infty}\frac{\exp\left(-ik_1u\right)}{\left(1+u^2\right)^{3/2}}du \tag{B.43}$$

$$I_2 = \int_{u_1}^{\infty}\frac{\exp\left(-ik_1u\right)}{\left(1+u^2\right)^{5/2}}du \tag{B.44}$$

$$u_1 = \left(MR - x_0\right)/\beta^2r_1,\ k_1 = \omega r_1/U,\ \beta = \left(1-M^2\right)^{1/2},$$

$$R = \left(x_0^2 + \beta^2r_1^2\right)^{1/2}$$

The integrals I_1 and I_2 cannot be expressed in terms of known functions but their numerical evaluation should pose no difficult problems. The commonly used method, proposed by Laschka, is the 11-term exponential polynomial. However, Desmarais used more terms and reduced the maximum error by two orders of magnitude as compared to Laschka's approximation.

B.6 DOUBLET LATTICE METHOD

The doublet lattice method is an empirical device which simplifies the integration of Eq(B.35). The doublet filament is placed at the ¼ chord of each box. The downwash *w* is evaluated at the ¾ chord midspan of each box. The downwash and load points are shown in Figure B.2

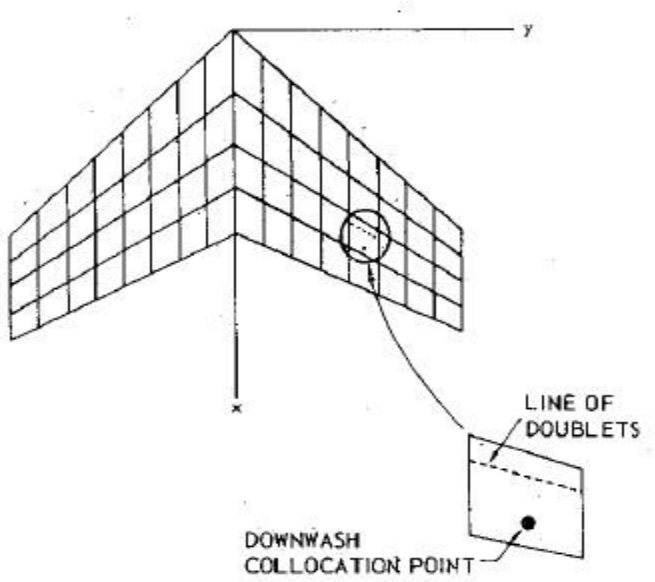

Figure B.2. DLM mesh definition of downwash and load points

Let *n* be the number of boxes, *i* denote the index of the downwash collocation point and *j* denote the index of line of doublets. The Eq(B.35) can be simplified as

$$\bar{w}_i = \sum_{j=1}^{n} A_{ij} \bar{p}_j \tag{B.45}$$

$$A_{ij} = \left(\frac{1}{8\pi}\right)\Delta x_j \cos\lambda_j \int_{ij} K\left(x_i, s_i, x_j(\mu), s_j(\mu), \omega, M\right) d\mu \tag{B.46}$$

where

Δx_j is the *j*th box average chord

λ_j is the sweep angle of the doublet line

If D_{ij} are the elements of the inversion of A_{ij}, the lifting pressure coefficients can be approximate as

$$\overline{p}_i = \sum_{j=1}^{n} D_{ij}\overline{w}_j \tag{B.47}$$

Now we consider the downwash induced at a receiving point $R = (x_R, y_R, z_R)$ by a doublet line segment with midpoint $S_m = (x_m, y_m, z_m)$ inboard point $S_i = (x_i, y_i, z_i)$ and outboard point $S_o = (x_o, y_o, z_o)$. Let $\kappa = r_1^2 K$ and denote

$$\kappa_m = \kappa(R, S_m), \kappa_i = \kappa(R, S_i), \kappa_o = \kappa(R, S_o)$$

Define the coordinate system

$$\eta = y\cos\gamma_s + z\sin\gamma_s \tag{B.48}$$

$$\zeta = -y\sin\gamma_s + z\cos\gamma_s \tag{B.49}$$

where γ_s is the dihedral angle of the local doublet line. The integration in Eq(B.46) can be approximated by

$$\begin{aligned} I_{ij} &= \int_{ij} K\left(x_i, s_i, x_j(\mu), s_j(\mu), \omega, M\right)\cos\lambda_j d\mu \\ &\approx \int_{-e}^{e} \frac{A\eta^2 + B\eta + C}{(\eta_0 - \eta)^2 + \zeta_0^2} d\eta \end{aligned} \tag{B.50}$$

where

$$e = \tfrac{1}{2} l_j \cos\lambda_j$$

$$\eta_0 = (y_R - y_m)\cos\gamma_s + (z_R - z_m)\sin\gamma_s$$

$$\zeta_0 = -(y_R - y_m)\sin\gamma_s + (z_R - z_m)\cos\gamma_s$$

$$A=\frac{\left(\kappa_i-2\kappa_m+\kappa_0\right)}{2e^2},\quad B=\frac{\left(\kappa_0-\kappa_i\right)}{2e},\quad C=\kappa_m$$

The result of the integration is

$$I_{ij}=\left[\left(\eta_0^2-\zeta_0^2\right)A+\eta_0 B+C\right]\left|\zeta_0\right|^{-1}\tan^{-1}\left(\frac{2e\left|\zeta_0\right|}{r_1^2-e^2}\right)+\left(\frac{1}{2}B+\eta_0 A\right)\log\frac{r_1^2-2\eta_0 e+e^2}{r_1^2+2\eta_0 e+e^2}+2eA \tag{B.51}$$

Finally, Rodden found it necessary to subtract the steady part from κ before applying the proceeding formulas, and then to add the effect from vortex lattice method.

B.7 GENERALIZED AERODYNAMIC

The integral equation relating downwash to pressures over the lifting surface

$$\bar{w}(x,y,z)=\left[\frac{-1}{4\pi\rho U}\right]\iint_s \Delta\bar{p}K\left((x-\xi),(y-\eta),z\right)d\xi d\eta \tag{B.52}$$

Discretization of the integral equation in the Doublet Lattice Method leads to a set of equations relating pressures at all boxes to downwash at all boxes in the matrix form:

$$\{w\}=[A]\{\Delta p\} \tag{B.53}$$

where

$\{w\}=\{w_1 \quad w_2 \quad ... \quad w_n\}^T$ is the vector of downwash values at the downwash points of all boxes, and $\{\Delta p\}=\{\Delta p_1 \quad \Delta p_2 \quad ... \quad \Delta p_n\}^T$ is the vector of pressure differences (lower surface minus upper surface at each box, located at the load point).

If a relationship between downwash at boxes (at their downwash points) and lift forces at boxes, L_i, is desired (with the lift forces acting at the load point of each box), then:

$$\{w\}=[AIC]\{L\}=[AIC]\{L\} \tag{B.54}$$

where

$$\{L\} = \begin{Bmatrix} L_1 \\ L_2 \\ \vdots \\ L_n \end{Bmatrix} = \begin{bmatrix} S_1 & & & \\ & S_2 & & \\ & & \ddots & \\ & & & S_n \end{bmatrix} \{\Delta p\} \tag{B.55}$$

The entries S_i in Eq. (B.55) above are the areas of the boxes. $[AIC]$ represents what is known as the Aerodynamic Influence Coefficients (which may be normalized in different ways).

Now we look at the downwash. Let the lifting surface move up as a function of space (location of x,y points on the surface) and time in a superposition of mode shapes and generalized displacements:

$$h(x,y,t) = h_1(x,y)q_1(t) + h_2(x,y)q_2(t) + \ldots h_N(x,y)q_N(t) = \sum_{j=1}^{N} h_j(x,y)q_j(t) \tag{B.56}$$

Note the separation of variables. Each shape is a function of space (x,y), and its contribution as a function of time is determined by the time dependence of its generalized displacement $q_j(t)$.

Recall Eq(B.54), the

$$w = \frac{\partial h}{\partial t} + U\frac{\partial h}{\partial x} \tag{B.57}$$

For simple harmonic motion at reduced frequency $k = \frac{\omega b}{U_\infty}$ and we switch from dependence on time to dependence on reduced frequency:

$$\frac{w(x,y,t)}{U} = \frac{J\omega h}{U} + \frac{\partial h}{\partial x} = Jk\frac{h}{b} + \frac{\partial h}{\partial x} \tag{B.58}$$

Note that $J = \sqrt{-1}$ is used here to denote the pure imaginary number, while elsewhere the index *j* is used to denote a mode shape number.

The generalized aerodynamic forces can now be derived.

The motion of the surface (Eq B.56):

$$h(x,y,t) = h_1(x,y)q_1(t) + h_2(x,y)q_2(t) + \ldots h_N(x,y)q_N(t) = \sum_{j=1}^{N} h_j(x,y)q_j(t)$$

This motion h determines the downwash over the surface at all downwash points on the discretized aerodynamic mesh. The result (from the integral equation) is the pressure distribution Δp over the surface (at all load points on the discretized aerodynamic mesh).

The virtual work done by these pressures when the surface moves through a virtual deformation $\delta h(x,y)$ is $\delta W = \iint \delta h(x,y)\Delta p(x,y)dxdy$.

Now,

$$\delta h(x,y,t) = h_1(x,y)\delta q_1(t) + ... + h_N(x,y)\delta q_N(t) = \sum_{i=1}^{N} h_i(x,y)\delta q_i(t) \tag{B.59}$$

Also the motion of Eq.(B.56) leads to the following downwash over the surface:

$$\frac{w(x,y,k)}{U_\infty} = \frac{\partial h}{\partial x} + Jk\frac{h}{b} = \sum_{j=1}^{N}\left(\frac{\partial h_j}{\partial x} + Jk\frac{h_j(x,y)}{b}\right)q_j(Jk) \tag{B.60}$$

The downwash, then, is a linear superposition of contributions, mode by mode, of the mode shapes used for the deformation approximation. And so, because of the linearity of the system, we may view the pressure distribution (the solution of the integral equation) as made of contributions, mode by mode, of the modes of motion used:

$$\Delta p(x,y,k) = \Delta p_1(x,y,k)q_1 + ...\Delta p_N(x,y,k)q_N = \sum_{j=1}^{N}\Delta p_j(x,y,k)q_j \tag{B.61}$$

Each $\Delta p_j(x,y,k)$ in Eq(B.61) is a solution of the integral equation with downwash contributed only by mode j with a generalized displacement $q_j = 1$. That is, $\Delta p_j(x,y,k)$ is the pressure distribution due to motion in mode j only of unit generalized displacement:

$$w_j(x,y)\Big|_{q_j=1} = U_\infty\left(\frac{\partial h_j}{\partial x} + Jk\frac{h_j(x,y)}{b}\right) = \left[\frac{-1}{4\pi\rho U}\right]\iint_s \Delta\bar{p}K\left((x-\xi),(y-\eta),z\right)d\xi \tag{B.62}$$

Then the virtual work is:

$$\delta W = \sum_{i=1}^{N}\iint \delta q_i h_i(x,y)\Delta p(x,y)dxdy = \sum_{i=1}^{N}\delta q_i \iint h_i(x,y)\sum_{j=1}^{N}\Delta p_j(x,y)q_j dxdy \tag{B.63}$$

Or:

$$\delta W = \sum_{i=1}^{N} \delta q_i \sum_{j=1}^{N} \iint h_i(x,y)\Delta p_j(x,y)dxdyq_j = \sum_{i=1}^{N} Q_i \delta q_i \tag{B.64}$$

where the generalized force associated with Lagrange equation of motion i in the set of N Lagrange equations for motions in N modes:

$$\frac{d}{dt}\left(\frac{\partial T}{\partial \dot{q}_i}\right) - \frac{\partial T}{\partial q_i} + \frac{\partial U}{\partial q_i} = Q_i \tag{B.65}$$

Is:

$$Q_i = \sum_{j=1}^{N} \iint h_i(x,y)\Delta p_j(x,y)dxdy \cdot q_j \tag{B.66}$$

When we write the N Lagrange equations for a linear aeroelastic system based on Eq(B.65):

$$[M]\{\ddot{q}\} + [K]\{q\} = \{Q\} \tag{B.67}$$

Because, for linear structural dynamics, the kinetic energy is:

$$T = \frac{1}{2}\{\dot{q}\}^T [M]\{\dot{q}\} \tag{B.68}$$

And the elastic energy is:

$$U = \frac{1}{2}\{q\}^T [K]\{q\} \tag{B.69}$$

Finally, the aerodynamic generalized forces can be written as

$$\{Q\} = q_D [A]\{q\} \tag{B.70}$$

Any term A_{ij} in the generalized aerodynamic force matrix of Eq(B.70) is the work done by motion in mode shape h_i when the pressure distribution is due to downwash of mode shape j: Δp_j

.

APPENDIX C. DERIVATION OF AEROSERVOELASTIC STATE-SPACE MODEL

The formulation of the aeroservoelastic (ASE) model begins with derivation of the state-space models for the plant, the sensor block, the actuator block, the control law and gust filter. The plant includes a flexible aircraft structure, unsteady aerodynamics, and gust response. The closed loop ASE system was shown in the following block diagram.

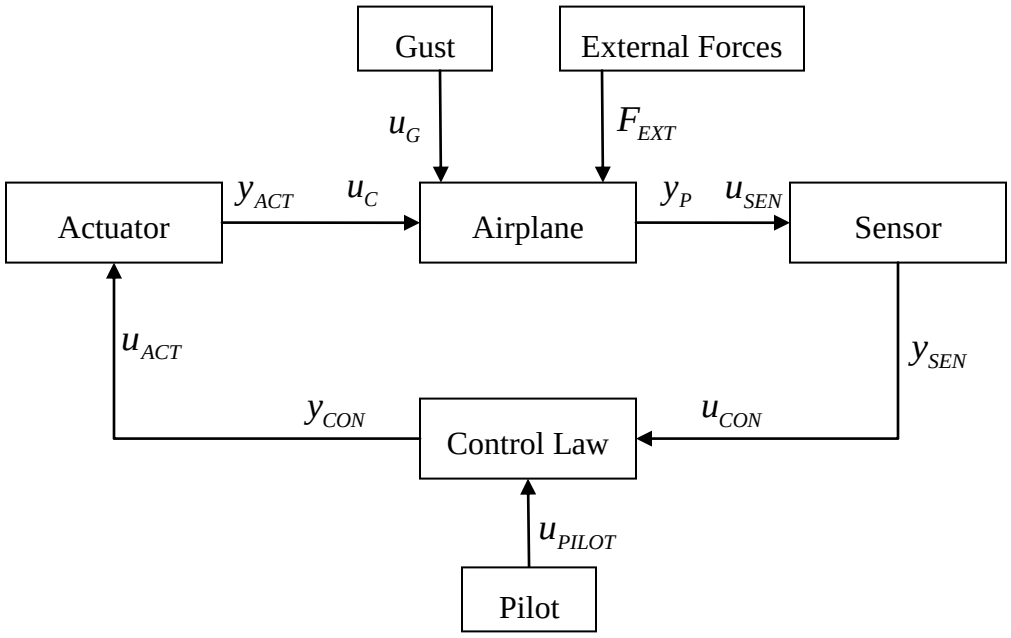

Figure C.1. Closed loop flow chart of ASE system

Before deriving the equations, we define the following terms.

$N_{DOF}^{Full\ Order}$	Number of DOF in full order structural model
n_s	Number of structural mode
n_c	Number of control mode
N_{act}	Number of distinct actuator input loads

N_β Number of lag terms used in aerodynamic fitting

N_β^G Number of lag terms used in gust fitting

n_d Number of displacements measured by sensor

n_v Number of velocities measured by sensor

n_a Number of accelerations measured by sensor

n_{act} Number of actuators

n_{sen} Number of sensors

C.1 AIRCRAFT PLANT MODEL

The aircraft plant model is based on the linear equations of motion of a flexible aircraft structure subjected to unsteady aerodynamics, external load, gust loads and internal loads caused by the activation of conventional actuators. The equations of motion of the self-induced full order FE model in Laplace domain are

$$\left([M]s^2+[C]s+[K]-q_D\left[A(s)\right]\right)\{u_{FE}\} = \frac{q_D}{U_\infty}\{F_G(s)\}W_G(s)+\{F_{EXT}\} \tag{C.1}$$

where

$[M],[C],[K]$-------Full order structural mass, damping and stiffness matrices

$\left[A(s)\right]$------Unsteady aerodynamic matrix in Laplace domain

$\{u_{FE}\}$------FEM Nodal displacements

$\frac{q_D}{U_\infty}\{F_G(s)\}W_G(s)$------Gust input

Now we transform the full order equation of motion to a reduced order system and add the conventional actuators system. Model order reduction is carried out by pre- and post-multiplying the full order system by a reduction basis $[\Phi]$. The basis $[\Phi]$ includes a selection of the lowest natural frequency modes of the structural plus a selection of modes where actuators are activated (defined as "control modes"). The control modes represent the rigid body control surface deflections.

In detail, the model order reduction is carried out as follows:

$$\{u_{FE}\} = [\Phi]\{q\} = [\Phi_s \;\vdots\; \Phi_c]\begin{Bmatrix} q_s \\ \cdots \\ q_c \end{Bmatrix} \tag{C.2}$$

where $\{q\}$ is named as modal coordinate. We farther partition the mode shapes and modal coordinate into structural terms Φ_s, q_s and control terms Φ_c, q_c.

$$\begin{aligned}\left([\Phi]^T[M][\Phi]s^2 + [\Phi]^T[C][\Phi]s + [\Phi]^T[K][\Phi] - q_D[\Phi]^T[A(s)][\Phi]\right)\{q\} \\ = \frac{q_D}{U_\infty}[\Phi]^T\{F_G(s)\}W_G(s) + [\Phi]^T\{F_{EXT}\} + \{F_{hinge}\}\end{aligned} \tag{C.3}$$

Realize that by introducing the actuators into the plant, the hinge moment applied by the actuators must be included by adding $\{F_{hinge}\}$ to the right hand side of the equation. This can be proved by considering the virtual work done by δq_c, which lead the generalized force due to control surface deflection non-zero. Therefore

$$\{F_{hinge}\} = \begin{Bmatrix} 0 \\ \cdots \\ H_C \end{Bmatrix} \tag{C.4}$$

The following terms are defined

$$\begin{bmatrix} \Phi_s^T \\ \cdots \\ \Phi_c^T \end{bmatrix}[M][\Phi_s \;\vdots\; \Phi_c] = \left[\begin{array}{c:c} [\Phi_s^T][M][\Phi_s] & [\Phi_s^T][M][\Phi_c] \\ \hdashline [\Phi_c^T][M][\Phi_s] & [\Phi_c^T][M][\Phi_c] \end{array}\right] = \left[\begin{array}{c:c} M_{ss} & M_{sc} \\ \hdashline M_{cs} & M_{cc} \end{array}\right] \tag{C.5}$$

$$\left[\begin{array}{c}\Phi_s^T \\ \hdashline \Phi_c^T\end{array}\right][C][\Phi_s \;\vdots\; \Phi_c]=\left[\begin{array}{c:c}[\Phi_s^T][C][\Phi_s] & [\Phi_s^T][C][\Phi_c] \\ \hdashline [\Phi_c^T][C][\Phi_s] & [\Phi_c^T][C][\Phi_c]\end{array}\right]=\left[\begin{array}{c:c}C_{ss} & C_{sc} \\ \hdashline C_{cs} & C_{cc}\end{array}\right] \tag{C.6}$$

$$\left[\begin{array}{c}\Phi_s^T \\ \hdashline \Phi_c^T\end{array}\right][K][\Phi_s \;\vdots\; \Phi_c]=\left[\begin{array}{c:c}[\Phi_s^T][K][\Phi_s] & [\Phi_s^T][K][\Phi_c] \\ \hdashline [\Phi_c^T][K][\Phi_s] & [\Phi_c^T][K][\Phi_c]\end{array}\right]=\left[\begin{array}{c:c}K_{ss} & K_{sc} \\ \hdashline K_{cs} & K_{cc}\end{array}\right] \tag{C.7}$$

$$\left[\begin{array}{c}\Phi_s^T \\ \hdashline \Phi_c^T\end{array}\right][A(s)][\Phi_s \;\vdots\; \Phi_c]=\left[\begin{array}{c:c}[\Phi_s^T][A(s)][\Phi_s] & [\Phi_s^T][A(s)][\Phi_c] \\ \hdashline [\Phi_c^T][A(s)][\Phi_s] & [\Phi_c^T][A(s)][\Phi_c]\end{array}\right]=\left[\begin{array}{c:c}A_{ss}(s) & A_{sc}(s) \\ \hdashline A_{cs}(s) & A_{cc}(s)\end{array}\right] \tag{C.8}$$

$$\left[\begin{array}{c}\Phi_s^T \\ \hdashline \Phi_c^T\end{array}\right]\{F_G(s)\}=\left[\begin{array}{c}[\Phi_s^T]\{F_G(s)\} \\ \hdashline [\Phi_c^T]\{F_G(s)\}\end{array}\right]=\left\{\begin{array}{c}F_{Gs}(s) \\ \hdashline F_{Gc}(s)\end{array}\right\} \tag{C.9}$$

It can be easily shown that the cross terms $C_{cs}, C_{sc}, K_{sc}, K_{cs}$ and K_{cc} are equal to zero.

Plug Eq(C.4)-Eq(C.9) in Eq(C.3), the equations of motion of the plant in model coordinate can be written as

$$\begin{aligned}&\left[\begin{array}{c:c}M_{ss} & M_{sc} \\ \hdashline M_{cs} & M_{cc}\end{array}\right]s^2\left\{\begin{array}{c}q_s \\ \hdashline q_c\end{array}\right\}+\left[\begin{array}{c:c}C_{ss} & 0 \\ \hdashline 0 & C_{cc}\end{array}\right]s\left\{\begin{array}{c}q_s \\ \hdashline q_c\end{array}\right\}+\left[\begin{array}{c:c}K_{ss} & 0 \\ \hdashline 0 & 0\end{array}\right]\left\{\begin{array}{c}q_s \\ \hdashline q_c\end{array}\right\} \\ &\qquad -q_D\left[\begin{array}{c:c}A_{ss}(s) & A_{sc}(s) \\ \hdashline A_{cs}(s) & A_{cc}(s)\end{array}\right]\left\{\begin{array}{c}q_s \\ \hdashline q_c\end{array}\right\}=\frac{q_D}{U_\infty}\left\{\begin{array}{c}F_{Gs}(s) \\ \hdashline F_{Gc}(s)\end{array}\right\}W_G(s)+\left\{\begin{array}{c}0 \\ \hdashline H_C\end{array}\right\}+\left\{\begin{array}{c}F_{EXTs} \\ \hdashline F_{EXTc}\end{array}\right\}\end{aligned} \tag{C.10}$$

Here we make an assumption that all the actuators can be considered as irreversible and the inputs q_c can be controlled directly. Therefore we move the terms with respect to q_c to the right hand side of the equations of motion and partition Eq(C.10) into two equations.

$$\begin{aligned}&[M_{ss}]s^2\{q_s\}+[C_{ss}]s\{q_s\}+[K_{ss}]\{q_s\}-q_D[A_{ss}(s)]\{q_s\}= \\ &\qquad -[M_{sc}]s^2\{q_c\}+q_D[A_{sc}(s)]\{q_c\}+\frac{q_D}{U_\infty}\{F_{Gs}(s)\}W_G(s)+\{F_{EXTs}\}\end{aligned} \tag{C.11}$$

$$\begin{aligned}&[M_{cs}]s^2\{q_s\}-q_D[A_{cs}(s)]\{q_s\}= \\ &\qquad -\left([M_{cc}]s^2+[C_{cc}]s-q_D[A_{cc}(s)]\right)\{q_c\}-\frac{q_D}{U_\infty}\{F_{Gc}(s)\}W_G(s)+\{F_{EXTc}\}+\{H_c\}\end{aligned} \tag{C.12}$$

Eq(C.11) will be used to form the state-space equation while the hinge moment $\{H_c\}$ can be solved by Eq(C.12). The size of the terms shown in Eq(C.11) are summarized as follows:

$[M_{ss}], [C_{ss}], [K_{ss}], [A_{ss}(s)]$ $\qquad\qquad$ $n_s \times n_s$

$[M_{sc}], [A_{sc}(s)]$ $n_s \times n_c$

$\{F_{Gs}(s)\}, \{q_s\}$ $n_s \times 1$

$\{q_c\}, \{F_{Gc}(s)\}, \{H_c\}$ $n_c \times 1$

$[M_{cs}], [A_{cs}(s)]$ $n_c \times n_s$

In order to make the derivation neat and clean, we assume the $\{F_{EXT}\}$ equals to zero. Once there is external load applied, it can be added in either Eq(C.11) and Eq(C.12) or the state-space form.

The unsteady aerodynamic and gust terms, $[A_{ss}(s)]$, $[A_{sc}(s)]$ and $\{F_{Gs}(s)\}$ respectively, in Eq(C.11) are already in generalized coordinates. There is variety of methods employed to produce these approximations. However, the method selected for this work is the Roger Method.

$$[A_{ss}(s)] = [P_{ss0}] + s[P_{ss1}] + s^2[P_{ss2}] + \frac{s}{s+\beta_1}[P_{ss3}] + \cdots + \frac{s}{s+\beta_{N_\beta}}\left[P_{ss(N_\beta+2)}\right] \quad \text{(C.13)}$$

$$[A_{sc}(s)] = [P_{sc0}] + s[P_{sc1}] + s^2[P_{sc2}] + \frac{s}{s+\beta_1}[P_{sc3}] + \cdots + \frac{s}{s+\beta_{N_\beta}}\left[P_{sc(N_\beta+2)}\right] \quad \text{(C.14)}$$

$$\{F_{Gs}(s)\} = \{P_{Gs0}\} + s\{P_{Gs1}\} + \frac{s}{s+\beta_1^G}\{P_{Gs3}\} + \cdots + \frac{s}{s+\beta_{N_\beta^G}^G}\left\{P_{Gs(N_\beta^G+2)}\right\} \quad \text{(C.15)}$$

Plug Eq(C.13)-Eq(C.15) into Eq(C.11) and define the following terms

$$[\bar{M}_{ss}] = [M_{ss}] - q_D[P_{ss2}] \quad \text{(C.16)}$$

$$[\bar{C}_{ss}] = [C_{ss}] - q_D[P_{ss1}] \quad \text{(C.17)}$$

$$[\bar{K}_{ss}] = [K_{ss}] - q_D[P_{ss0}] \quad \text{(C.18)}$$

$$[\bar{M}_{sc}] = [M_{sc}] - q_D[P_{sc2}] \quad \text{(C.19)}$$

$$[\bar{C}_{sc}] = -q_D[P_{sc1}] \quad \text{(C.20)}$$

$$[\bar{K}_{sc}] = -q_D[P_{sc0}] \quad \text{(C.21)}$$

The equations of motion can be written as

$$\left[\bar{M}_{ss}\right]s^2\{q_s\}+\left[\bar{C}_{ss}\right]s\{q_s\}+\left[\bar{K}_{ss}\right]\{q_s\}-q_D\frac{s}{s+\beta_1}\left[P_{ss3}\ \vdots\ P_{sc3}\right]\left\{\begin{matrix}q_s\\ \cdots\\ q_c\end{matrix}\right\}-\cdots$$

$$-q_D\frac{s}{s+\beta_{N_\beta}}\left[P_{ss(N_\beta+2)}\ \vdots\ P_{sc(N_\beta+2)}\right]\left\{\begin{matrix}q_s\\ \cdots\\ q_c\end{matrix}\right\}=-\left[\bar{M}_{sc}\right]s^2\{q_c\}-\left[\bar{C}_{sc}\right]s\{q_c\}-\left[\bar{K}_{sc}\right]\{q_c\} \tag{C.22}$$

$$+\frac{q_D}{U_\infty}\left[P_{Gs0}+P_{Gs1}s+\frac{s}{s+\beta_1^G}P_{Gs3}+\cdots+\frac{s}{s+\beta_{N_\beta^G}^G}P_{Gs(N_\beta^G+2)}\right]W_G(s)$$

Now we define the states of the equations of motion for state-space form.

$$\{x_1\}=\{q_s\} \qquad n_s\times 1 \tag{C.23}$$

$$\{x_2\}=\{sq_s\} \qquad n_s\times 1 \tag{C.24}$$

$$\{r_1\}=\frac{s}{s+\beta_1}\left[P_{ss3}\ \vdots\ P_{sc3}\right]\left\{\begin{matrix}q_s\\ \cdots\\ q_c\end{matrix}\right\} \qquad n_s\times 1 \tag{C.25}$$

$$\vdots \qquad \vdots$$

$$\left\{r_{N_\beta}\right\}=\frac{s}{s+\beta_{N_\beta}}\left[P_{ss(N_\beta+2)}\ \vdots\ P_{sc(N_\beta+2)}\right]\left\{\begin{matrix}q_s\\ \cdots\\ q_c\end{matrix}\right\} \qquad n_s\times 1 \tag{C.26}$$

$$r_1^G=\frac{s}{s+\beta_1^G}W_G(s) \qquad 1\times 1 \tag{C.27}$$

$$\vdots \qquad \vdots$$

$$r_{N_\beta^G}^G=\frac{s}{s+\beta_{N_\beta^G}^G}W_G(s) \qquad 1\times 1 \tag{C.28}$$

Then the following relationship can be derived

$$s\{x_1\}=\{x_2\} \qquad n_s\times 1 \tag{C.29}$$

$$s\{r_1\}=-\beta_1\{r_1\}+\left[P_{ss3}\right]\{x_2\}+\left[P_{sc3}\right]s\{q_c\} \qquad n_s\times 1 \tag{C.30}$$

$$\vdots \qquad \vdots \tag{C.31}$$

$$s\left\{r_{N_\beta}\right\}=-\beta_{N_\beta}\left\{r_{N_\beta}\right\}+\left[P_{ss(N_\beta+2)}\right]\{x_2\}+\left[P_{sc(N_\beta+2)}\right]s\{q_c\} \qquad n_s\times 1$$

$$sr_1^G=-\beta_1^G r_1^G+sW_G(s) \qquad 1\times 1 \tag{C.32}$$

$$\vdots \qquad \vdots$$

$$sr_{N_\beta^G}^G=-\beta_{N_\beta^G}^G r_{N_\beta^G}^G+sW_G(s) \qquad 1\times 1 \tag{C.33}$$

The complete state vector for the aircraft plant (structural motions, control motions, aerodynamic lags and gust lags) is

$$\{x_P\}^T=\left\{\{x_1\}^T\quad\{x_2\}^T\quad\{r_1\}^T\quad\cdots\quad\left\{r_{N_\beta}\right\}^T\quad r_1^G\quad\cdots\quad r_{N_\beta^G}^G\right\} \tag{C.34}$$

Plug Eq(C.29)-Eq(C.33) into Eq(C.22) and collect the states terms, the state-space equations of motion of the plant can be written as the form of

$$s\{x_P\} = [A_P]\{x_P\} + [B_C]\{u_C\} + [B_G]\{u_G\} \tag{C.35}$$

where

$$[A_P] = \begin{bmatrix} [0] & [I] & [0] & \cdots & [0] & \{0\} & \cdots & \{0\} \\ -[\bar{M}_{ss}]^{-1}[\bar{K}_{ss}] & -[\bar{M}_{ss}]^{-1}[\bar{C}_{ss}] & q_D[\bar{M}_{ss}]^{-1} & \cdots & q_D[\bar{M}_{ss}]^{-1} & \frac{q_D}{U_\infty}[\bar{M}_{ss}]^{-1}\{P_{Gs3}\} & \cdots & \frac{q_D}{U_\infty}[\bar{M}_{ss}]^{-1}\left\{P_{Gs(N_\beta^G+2)}\right\} \\ [0] & [P_{ss3}] & -\beta_1[I] & \cdots & [0] & \{0\} & \cdots & \{0\} \\ \vdots & \vdots & \vdots & \ddots & \vdots & \vdots & \ddots & \vdots \\ [0] & \left[P_{ss(N_\beta+2)}\right] & [0] & \cdots & -\beta_{N_\beta}[I] & \{0\} & \cdots & \{0\} \\ \{0\}^T & \{0\}^T & \{0\}^T & \cdots & \{0\}^T & -\beta_1^G & \cdots & 0 \\ \vdots & \vdots & \vdots & \ddots & \vdots & \vdots & \ddots & \vdots \\ \{0\}^T & \{0\}^T & \{0\}^T & \cdots & \{0\}^T & 0 & \cdots & -\beta_{N_\beta^G}^G \end{bmatrix} \tag{C.36}$$

$$[B_C] = \begin{bmatrix} [0] & [0] & [0] \\ -[\bar{M}_{ss}]^{-1}[\bar{K}_{sc}] & -[\bar{M}_{ss}]^{-1}[\bar{C}_{sc}] & -[\bar{M}_{ss}]^{-1}[\bar{M}_{sc}] \\ [0] & [P_{sc3}] & [0] \\ \vdots & \vdots & \vdots \\ [0] & \left[P_{sc(N_\beta+2)}\right] & [0] \\ \{0\}^T & \{0\}^T & \{0\}^T \\ \vdots & \vdots & \vdots \\ \{0\}^T & \{0\}^T & \{0\}^T \end{bmatrix} \tag{C.37}$$

$$[B_G] = \begin{bmatrix} \{0\} & \{0\} \\ \frac{q_D}{U_\infty}[\bar{M}_{ss}]^{-1}\{P_{Gs0}\} & \frac{q_D}{U_\infty}[\bar{M}_{ss}]^{-1}\{P_{Gs1}\} \\ \{0\} & \{0\} \\ \vdots & \vdots \\ \{0\} & \{0\} \\ 0 & 1 \\ \vdots & \vdots \\ 0 & 1 \end{bmatrix} \tag{C.38}$$

To make the derivation more clear, the size of the sub-matrix are indicated as

$$[A_P]=\begin{bmatrix} n_s\times n_s & n_s\times n_s & n_s\times n_s & \cdots & n_s\times n_s & n_s\times 1 & \cdots & n_s\times 1 \\ n_s\times n_s & n_s\times n_s & n_s\times n_s & \cdots & n_s\times n_s & n_s\times 1 & \cdots & n_s\times 1 \\ n_s\times n_s & n_s\times n_s & n_s\times n_s & \cdots & n_s\times n_s & n_s\times 1 & \cdots & n_s\times 1 \\ \vdots & \vdots & \vdots & \ddots & \vdots & \vdots & \ddots & \vdots \\ n_s\times n_s & n_s\times n_s & n_s\times n_s & \cdots & n_s\times n_s & n_s\times 1 & \cdots & n_s\times 1 \\ 1\times n_s & 1\times n_s & 1\times n_s & \cdots & 1\times n_s & 1\times 1 & \cdots & 1\times 1 \\ \vdots & \vdots & \vdots & \ddots & \vdots & \vdots & \ddots & \vdots \\ 1\times n_s & 1\times n_s & 1\times n_s & \cdots & 1\times n_s & 1\times 1 & \cdots & 1\times 1 \end{bmatrix} \quad \begin{matrix} \left(n_s\left(2+N_\beta\right)+N_\beta^G\right) \\ \times\left(n_s\left(2+N_\beta\right)+N_\beta^G\right) \end{matrix} \tag{C.39}$$

$$[B_C]=\begin{bmatrix} n_s\times n_c & n_s\times n_c & n_s\times n_c \\ n_s\times n_c & n_s\times n_c & n_s\times n_c \\ n_s\times n_c & n_s\times n_c & n_s\times n_c \\ \vdots & \vdots & \vdots \\ n_s\times n_c & n_s\times n_c & n_s\times n_c \\ 1\times n_c & 1\times n_c & 1\times n_c \\ \vdots & \vdots & \vdots \\ 1\times n_c & 1\times n_c & 1\times n_c \end{bmatrix} \quad \left(n_s\left(2+N_\beta\right)+N_\beta^G\right)\times 3n \tag{C.40}$$

$$[B_G]=\begin{bmatrix} n_s\times 1 & n_s\times 1 \\ n_s\times 1 & n_s\times 1 \\ n_s\times 1 & n_s\times 1 \\ \vdots & \vdots \\ n_s\times 1 & n_s\times 1 \\ 1\times 1 & 1\times 1 \\ \vdots & \vdots \\ 1\times 1 & 1\times 1 \end{bmatrix} \quad \left(n_s\left(2+N_\beta\right)+N_\beta^G\right)\times 2 \tag{C.41}$$

Now we derive the observation equation. Since the displacement, velocity and acceleration can only be measured by sensors or equipments, the actual motion have to be written in a series of summation of modal coordinate. Recall Eq(C.2), the displacements of location *i*,*j*,*k* can be defined as

$$\begin{Bmatrix} u_i \\ u_j \\ u_k \end{Bmatrix}=\begin{Bmatrix} \phi_{i1}q_{s1}+\phi_{i2}q_{s2}+\cdots+\phi_{in_s}q_{sn_s} \\ \phi_{j1}q_{s1}+\phi_{j2}q_{s2}+\cdots+\phi_{jn_s}q_{sn_s} \\ \phi_{k1}q_{s1}+\phi_{k2}q_{s2}+\cdots+\phi_{kn_s}q_{sn_s} \end{Bmatrix}=\begin{bmatrix} \phi_{i1} & \cdots & \phi_{in_s} \\ \phi_{j1} & \cdots & \phi_{jn_s} \\ \phi_{k1} & \cdots & \phi_{kn_s} \end{bmatrix}\begin{Bmatrix} q_{s1} \\ \vdots \\ q_{sn_s} \end{Bmatrix}=\begin{bmatrix} \psi_{i0} \\ \psi_{j0} \\ \psi_{k0} \end{bmatrix}\{q_s\}=[\Psi_0]\{q_s\} \tag{C.42}$$

Similarly, the velocity and acceleration can be written as

$$\begin{aligned}\{v\} &= [\Psi_1] s\{q_s\} \\ \{a\} &= [\Psi_2] s^2 \{q_s\}\end{aligned} \tag{C.43}$$

The observation matrix can be described as

$$\{y_P\} = [\bar{\Psi}_1]\{x_P\} + [\bar{\Psi}_2] s\{x_P\} \tag{C.44}$$

where

$$\{y_P\} = \begin{Bmatrix} u_1 & \cdots & u_{nd} & v_1 & \cdots & v_{nv} & a_1 & \cdots & a_{n_a} \end{Bmatrix}^T \tag{C.45}$$

$$[\bar{\Psi}_1] = \begin{bmatrix} [\Psi_0] & [0] & [0] \\ [0] & [\Psi_1] & [0] \\ [0] & [0] & [0] \end{bmatrix} \tag{C.46}$$

$$[\bar{\Psi}_2] = \begin{bmatrix} [0] & [0] & [0] \\ [0] & [0] & [0] \\ [0] & [\Psi_2] & [0] \end{bmatrix} \tag{C.47}$$

Again, similar as before, we indicate the size of the sub-matrix.

$$\{y_P\} = \begin{Bmatrix} 1\times n_d & 1\times n_v & 1\times n_a \end{Bmatrix}^T \qquad (n_d + n_v + n_a)\times 1 \tag{C.48}$$

$$[\bar{\Psi}_1] = \begin{bmatrix} n_d \times n_s & n_d \times n_s & n_d \times \left(n_s N_\beta + N_\beta^G\right) \\ n_v \times n_s & n_v \times n_s & n_v \times \left(n_s N_\beta + N_\beta^G\right) \\ n_a \times n_s & n_a \times n_s & n_a \times \left(n_s N_\beta + N_\beta^G\right) \end{bmatrix} \qquad \begin{matrix} (n_d + n_v + n_a) \\ \times\left(n_s\left(2 + N_\beta\right) + N_\beta^G\right) \end{matrix} \tag{C.49}$$

$$[\bar{\Psi}_2] = \begin{bmatrix} n_d \times n_s & n_d \times n_s & n_d \times \left(n_s N_\beta + N_\beta^G\right) \\ n_v \times n_s & n_v \times n_s & n_v \times \left(n_s N_\beta + N_\beta^G\right) \\ n_a \times n_s & n_a \times n_s & n_a \times \left(n_s N_\beta + N_\beta^G\right) \end{bmatrix} \qquad \begin{matrix} (n_d + n_v + n_a) \\ \times\left(n_s\left(2 + N_\beta\right) + N_\beta^G\right) \end{matrix} \tag{C.50}$$

Now plug Eq(C.35) into Eq(C.44)

$$\begin{aligned}\{y_P\} &= [\bar{\Psi}_1]\{x_P\} + [\bar{\Psi}_2]\left\{[A_P]\{x_P\} + [B_C]\{u_C\} + [B_G]\{u_G\}\right\} \\ &= \left([\bar{\Psi}_1] + [\bar{\Psi}_2][A_P]\right)\{x_P\} + [\bar{\Psi}_2][B_C]\{u_C\} + [\bar{\Psi}_2][B_G]\{u_G\} \\ &= [C_P]\{x_P\} + [D_C]\{u_C\} + [D_G]\{u_G\}\end{aligned} \tag{C.51}$$

Therefore Eq(C.35) and Eq(C.51) are the state-space form of the plant.

C.2 AIRCRAFT ACTUATOR

The actuator system in an airplane can be modeled as a block of elements; each element may be either SISO or MIMO actuator.

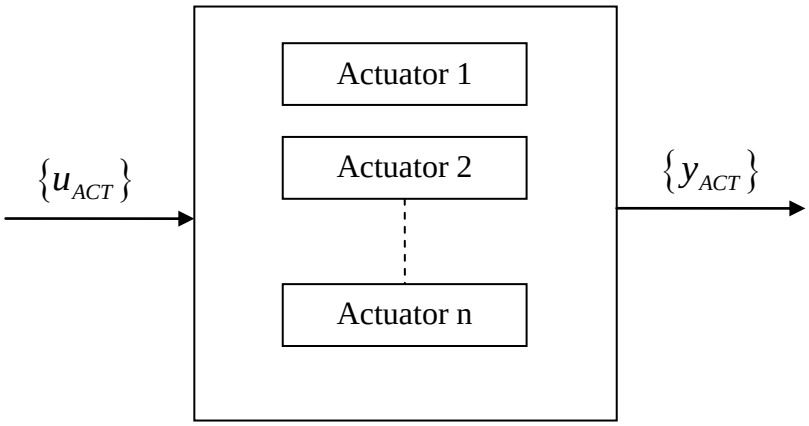

Figure C.2. System actuator block

Each actuator set in the aircraft is assigned a strictly proper transfer function in the form:

$$\frac{y_{acti}}{u_{acti}} = \frac{b_{n-1}s^{n-1} + \cdots + b_1 s + b_0}{s^n + a_{n-1}s^{n-1} + \cdots + a_1 s + a_0} \tag{C.52}$$

Note that in the actuators sets, it is often required that the transfer function numerator is at least two orders of magnitude less than the denominator. But here we start from the general case and will show the necessity to make the denominator with higher order.

First, state-space realizations of each actuator set's transfer function are created in either the observer form:

$$\left[A_{acti}\right] = \begin{bmatrix} -a_{n-1} & 1 & 0 & \cdots & 0 \\ -a_{n-2} & 0 & 1 & \cdots & 0 \\ \vdots & \vdots & \vdots & \ddots & \vdots \\ -a_1 & 0 & 0 & \cdots & 1 \\ -a_0 & 0 & 0 & \cdots & 0 \end{bmatrix} \qquad \left\{B_{acti}\right\} = \begin{Bmatrix} b_{n-1} \\ b_{n-2} \\ \vdots \\ b_1 \\ b_0 \end{Bmatrix} \tag{C.53}$$

$$\left\{C_{acti}\right\} = \begin{Bmatrix} 1 & 0 & \cdots & 0 & 0 \end{Bmatrix} \qquad D_{acti} = 0$$

or the controller form:

$$\left[A_{acti}\right]=\begin{bmatrix} 0 & 1 & 0 & \cdots & 0 \\ 0 & 0 & 1 & \cdots & 0 \\ \vdots & \vdots & \vdots & \ddots & \vdots \\ 0 & 0 & 0 & \cdots & 1 \\ -a_0 & -a_1 & -a_2 & \cdots & -a_{n-1} \end{bmatrix} \qquad \left\{B_{acti}\right\}=\begin{Bmatrix} 0 \\ 0 \\ \vdots \\ 0 \\ 1 \end{Bmatrix}$$
$$\left\{C_{acti}\right\}=\begin{Bmatrix} b_0 & b_1 & \cdots & b_{n-2} & b_{n-1} \end{Bmatrix} \qquad D_{acti}=0 \tag{C.54}$$

Therefore the state-space form or actuator *i* can be written as

$$\begin{aligned} s\left\{x_{acti}\right\}&=\left[A_{acti}\right]\left\{x_{acti}\right\}+\left\{B_{acti}\right\}\left\{u_{acti}\right\} \\ \left\{y_{acti}\right\}&=\left\{C_{acti}\right\}\left\{x_{acti}\right\} \end{aligned} \tag{C.55}$$

It can be shown that $\left\{C_{acti}\right\}\left\{B_{acti}\right\}=b_{n-1}$, therefore, if the numerator is at least two orders of magnitude less than the denominator

$$\left\{C_{acti}\right\}\left\{B_{acti}\right\}=0 \tag{C.56}$$

This will further simplify the equation in the following section.

For a block of actuators, the system state-space form of equation is

$$\begin{aligned} s\left\{x_{ACT}\right\}&=\left[A_{ACT}\right]\left\{x_{ACT}\right\}+\left[B_{ACT}\right]\left\{u_{ACT}\right\} \\ \left\{y_{ACT}\right\}&=\left[C_{ACT}\right]\left\{x_{ACT}\right\} \end{aligned} \tag{C.57}$$

where

$$\left\{x_{ACT}\right\}^T=\begin{Bmatrix} \left\{x_{act1}\right\}^T & \left\{x_{act2}\right\}^T & \cdots & \left\{x_{actn_{act}}\right\}^T \end{Bmatrix}$$
$$\left\{y_{ACT}\right\}^T=\begin{Bmatrix} \left\{y_{act1}\right\}^T & \left\{y_{act2}\right\}^T & \cdots & \left\{y_{actn_{act}}\right\}^T \end{Bmatrix}$$
$$\left[A_{ACT}\right]=\begin{bmatrix} \left[A_{act1}\right] & & & \\ & \left[A_{act2}\right] & & \\ & & \ddots & \\ & & & \left[A_{actn_{act}}\right] \end{bmatrix} \tag{C.58}$$
$$\left[B_{ACT}\right]=\begin{bmatrix} \left\{B_{act1}\right\} & & & \\ & \left\{B_{act2}\right\} & & \\ & & \ddots & \\ & & & \left\{B_{actn_{act}}\right\} \end{bmatrix}$$

$$[C_{ACT}]=\begin{bmatrix}\{C_{act1}\} & & & \\ & \{C_{act2}\} & & \\ & & \ddots & \\ & & & \{C_{actn_{act}}\}\end{bmatrix}$$

C.3 AIRCRAFT SENSOR

The sensor can be modeled either as prefect sensor or non-perfect sensor based on the user's selection. As for the prefect sensor, the output of the sensor is exact same as the output of the plant, therefore

$$\{y_{SEN}\}=\{y_P\} \tag{C.59}$$

There is a transfer function applied to non-prefect sensor. Similarly as aircraft actuator, individual sensor *i* can be also modeled as

$$\frac{y_{seni}}{u_{seni}}=\frac{b_{n-1}s^{n-1}+\cdots+b_1s+b_0}{s^n+a_{n-1}s^{n-1}+\cdots+a_1s+a_0} \tag{C.60}$$

The state-space form of Eq(C.59) is

$$\begin{aligned}s\{x_{seni}\}&=[A_{seni}]\{x_{seni}\}+\{B_{seni}\}\{u_{seni}\}\\ \{y_{seni}\}&=\{C_{seni}\}\{x_{seni}\}\end{aligned} \tag{C.61}$$

For a block of sensors, the system state-space form is

$$\begin{aligned}s\{x_{SEN}\}&=[A_{SEN}]\{x_{SEN}\}+[B_{SEN}]\{u_{SEN}\}\\ \{y_{SEN}\}&=[C_{SEN}]\{x_{SEN}\}\end{aligned} \tag{C.62}$$

where

$$\begin{aligned}\{x_{SEN}\}^T&=\left\{\{x_{sen1}\}^T \quad \{x_{sen2}\}^T \quad \cdots \quad \{x_{senn_{sen}}\}^T\right\}\\ \{y_{SEN}\}^T&=\left\{\{y_{sen1}\}^T \quad \{y_{sen2}\}^T \quad \cdots \quad \{y_{senn_{sen}}\}^T\right\}\end{aligned} \tag{C.63}$$

$$[A_{SEN}]=\begin{bmatrix}[A_{sen1}] & & & \\ & [A_{sen2}] & & \\ & & \ddots & \\ & & & [A_{senn_{sen}}]\end{bmatrix}$$

$$[B_{SEN}]=\begin{bmatrix}\{B_{sen1}\} & & & \\ & \{B_{sen2}\} & & \\ & & \ddots & \\ & & & \{B_{senn_{sen}}\}\end{bmatrix}$$

$$[C_{SEN}]=\begin{bmatrix}\{C_{sen1}\} & & & \\ & \{C_{sen2}\} & & \\ & & \ddots & \\ & & & \{C_{senn_{sen}}\}\end{bmatrix}$$

C.4 CONTROL LAW

The control law can be either optimum control or classic control.

For classic control, similarly as aircraft actuator, individual control law *i* can be also modeled as

$$\frac{y_{coni}}{u_{coni}}=\frac{b_n s^n+b_{n-1}s^{n-1}+\cdots+b_1 s+b_0}{s^n+a_{n-1}s^{n-1}+\cdots+a_1 s+a_0} \tag{C.64}$$

The state-space form of Eq(C.64) can be realized as

$$\begin{aligned} s\{x_{coni}\}&=[A_{coni}]\{x_{coni}\}+\{B_{coni}\}\{u_{coni}\}\\ \{y_{coni}\}&=\{C_{coni}\}\{x_{coni}\}+D_{coni}\{u_{coni}\}\end{aligned} \tag{C.65}$$

Realize that since $b_n \neq 0$, $D_{coni} \neq 0$.

Adding the pilot command, a series of control system state-space form is

$$\begin{aligned} s\{x_{CON}\}&=[A_{CON}]\{x_{CON}\}+[B_{CON}]\{u_{CON}\}+[B_{PILOT}]\{u_{PILOT}\}\\ \{y_{CON}\}&=[C_{CON}]\{x_{CON}\}+[D_{CON}]\{u_{CON}\}+[D_{PILOT}]\{u_{PILOT}\}\end{aligned} \tag{C.66}$$

where

$$\{x_{CON}\}^T = \left\{ \{x_{con1}\}^T \quad \{x_{con2}\}^T \quad \cdots \quad \{x_{conn_{con}}\}^T \right\}$$

$$\{y_{CON}\}^T = \left\{ \{y_{con1}\}^T \quad \{y_{con2}\}^T \quad \cdots \quad \{y_{conn_{con}}\}^T \right\}$$

$$[A_{CON}] = \begin{bmatrix} [A_{con1}] & & & \\ & [A_{con2}] & & \\ & & \ddots & \\ & & & [A_{conn_{con}}] \end{bmatrix}$$

$$[B_{CON}] = \begin{bmatrix} \{B_{con1}\} & & & \\ & \{B_{con2}\} & & \\ & & \ddots & \\ & & & \{B_{conn_{con}}\} \end{bmatrix} \tag{C.67}$$

$$[C_{CON}] = \begin{bmatrix} \{C_{con1}\} & & & \\ & \{C_{con2}\} & & \\ & & \ddots & \\ & & & \{C_{conn_{con}}\} \end{bmatrix}$$

$$[D_{CON}] = \begin{bmatrix} D_{con1} & & & \\ & D_{con2} & & \\ & & \ddots & \\ & & & D_{conn_{con}} \end{bmatrix}$$

C.5 CLOSED-LOOP SYSTEM EQUATIONS OF MOTION

Before we move to the closed loop, the set of equations are recollected to give the readers a clear and neat view.

Plant

$$s\{x_P\} = [A_P]\{x_P\} + [B_C]\{u_C\} + [B_G]\{u_G\} \tag{C.68}$$

$$\{y_P\} = [C_P]\{x_P\} + [D_C]\{u_C\} + [D_G]\{u_G\} \tag{C.69}$$

Actuator

$$s\{x_{ACT}\} = [A_{ACT}]\{x_{ACT}\} + [B_{ACT}]\{u_{ACT}\} \tag{C.70}$$

$$\{y_{ACT}\} = [C_{ACT}]\{x_{ACT}\} \tag{C.71}$$

Sensor

$$s\{x_{SEN}\} = [A_{SEN}]\{x_{SEN}\} + [B_{SEN}]\{u_{SEN}\} \tag{C.72}$$

$$\{y_{SEN}\} = [C_{SEN}]\{x_{SEN}\} \tag{C.73}$$

Control Law

$$s\{x_{CON}\} = [A_{CON}]\{x_{CON}\} + [B_{CON}]\{u_{CON}\} + [B_{PILOT}]\{u_{PILOT}\} \tag{C.74}$$

$$\{y_{CON}\} = [C_{CON}]\{x_{CON}\} + [D_{CON}]\{u_{CON}\} + [D_{PILOT}]\{u_{PILOT}\} \tag{C.75}$$

Then from Eq(C.69), the general form of plant input $\{u_c\}$ depends on displacement, velocity and acceleration of the control surfaces.

$$\{u_c\} = \begin{Bmatrix} \{q_c\} \\ s\{q_c\} \\ s^2\{q_c\} \end{Bmatrix} = \begin{Bmatrix} \{y_{ACT}\} \\ s\{y_{ACT}\} \\ s^2\{y_{ACT}\} \end{Bmatrix} \tag{C.76}$$

Now we take the first and second derivative of Eq(C.71) to find $s\{y_{ACT}\}$ and $s^2\{y_{ACT}\}$

$$s\{y_{ACT}\} = [C_{ACT}]s\{x_{ACT}\} \tag{C.77}$$

Plug Eq(C.70) into Eq(C.77)

$$s\{y_{ACT}\} = [C_{ACT}][A_{ACT}]\{x_{ACT}\} + [C_{ACT}][B_{ACT}]\{u_{ACT}\} \tag{C.78}$$

$$s^2\{y_{ACT}\} = [C_{ACT}][A_{ACT}]s\{x_{ACT}\} + [C_{ACT}][B_{ACT}]s\{u_{ACT}\} \tag{C.79}$$

Plug Eq(C.70) into Eq(C.79)

$$s^2\{y_{ACT}\} = [C_{ACT}][A_{ACT}][A_{ACT}]\{x_{ACT}\} + [C_{ACT}][A_{ACT}][B_{ACT}]\{u_{ACT}\} + [C_{ACT}][B_{ACT}]s\{u_{ACT}\} \tag{C.80}$$

Recall Eq(C.56), with the assumption that the numerator of the actuator is at least two orders of magnitude less than the denominator, Eq(C.80) can be reduced to

$$s^2\{y_{ACT}\} = [C_{ACT}][A_{ACT}][A_{ACT}]\{x_{ACT}\} \tag{C.81}$$

Plug Eq(C.71), Eq(C.77), Eq(C.81) into Eq(C.76)

$$\{u_c\} = \begin{Bmatrix} \{q_c\} \\ s\{q_c\} \\ s^2\{q_c\} \end{Bmatrix} = \begin{bmatrix} [C_{ACT}] \\ [C_{ACT}][A_{ACT}] \\ [C_{ACT}][A_{ACT}][A_{ACT}] \end{bmatrix} \{x_{ACT}\} = \left[\bar{C}_{ACT}\right]\{x_{ACT}\} \tag{C.82}$$

Plug Eq(C.82) into Eq(C.68) and Eq(C.69)

$$s\{x_P\} = [A_P]\{x_P\} + [B_C]\left[\bar{C}_{ACT}\right]\{x_{ACT}\} + [B_G]\{u_G\} \tag{C.83}$$

$$\{y_P\} = [C_P]\{x_P\} + [D_C]\left[\bar{C}_{ACT}\right]\{x_{ACT}\} + [D_G]\{u_G\} \tag{C.84}$$

Realize that $\{u_{SEN}\} = \{y_P\}$, plug Eq(C.84) into Eq(C.72)

$$s\{x_{SEN}\} = [A_{SEN}]\{x_{SEN}\} + [B_{SEN}][C_P]\{x_P\} + [B_{SEN}][D_C]\left[\bar{C}_{ACT}\right]\{x_{ACT}\} + [B_{SEN}][D_G]\{u_G\} \tag{C.85}$$

Also realize that $\{u_{CON}\} = \{y_{SEN}\}$, plug Eq(C.73) into Eq(C.74) and Eq(C.75)

$$s\{x_{CON}\} = [A_{CON}]\{x_{CON}\} + [B_{CON}][C_{SEN}]\{x_{SEN}\} + [B_{PILOT}]\{u_{PILOT}\} \tag{C.86}$$

$$\{y_{CON}\} = [C_{CON}]\{x_{CON}\} + [D_{CON}][C_{SEN}]\{x_{SEN}\} + [D_{PILOT}]\{u_{PILOT}\} \tag{C.87}$$

Since $\{u_{ACT}\} = \{y_{CON}\}$, plug Eq(C.87) into Eq(C.70)

$$\begin{aligned} s\{x_{ACT}\} = {} & [A_{ACT}]\{x_{ACT}\} + [B_{ACT}][C_{CON}]\{x_{CON}\} \\ & + [B_{ACT}][D_{CON}][C_{SEN}]\{x_{SEN}\} + [B_{ACT}][D_{PILOT}]\{u_{PILOT}\} \end{aligned} \tag{C.88}$$

Therefore, combine Eq(C.83), Eq(C.85), Eq(C.86) and Eq(C.88). The closed loop system can be written in the state-space form of

$$s\{x_{SYS}\} = [A_{SYS}]\{x_{SYS}\} + [B_{GSYS}]\{u_G\} + [B_{PILOTSYS}]\{u_{PILOT}\} \tag{C.89}$$

where

$$\{x_{SYS}\}^T = \left\{\{x_P\}^T \quad \{x_{SEN}\}^T \quad \{x_{ACT}\}^T \quad \{x_{CON}\}^T\right\}$$

$$[A_{SYS}] = \begin{bmatrix} \left[A_p\right] & [0] & [B_C]\left[\bar{C}_{ACT}\right] & [0] \\ [B_{SEN}][C_P] & [A_{SEN}] & [B_{SEN}][D_C]\left[\bar{C}_{ACT}\right] & [0] \\ [0] & [B_{ACT}][D_{CON}][C_{SEN}] & [A_{ACT}] & [B_{ACT}][C_{CON}] \\ [0] & [B_{CON}][C_{SEN}] & [0] & [A_{CON}] \end{bmatrix}$$

$$[B_{GSYS}] = \begin{bmatrix} [B_G] \\ [B_{SEN}][D_G] \\ [0] \\ [0] \end{bmatrix} \qquad [B_{PILOTSYS}] = \begin{bmatrix} [0] \\ [0] \\ [B_{ACT}][D_{PILOT}] \\ [B_{PILOT}] \end{bmatrix}$$

VITA

Sang Wu

May 30, 1987	Born in Xi'an, Shaanxi Province, China
June, 2005	Graduated from The Middle School Attached To Northwestern Polytechnical University, Xi'an, Shaanxi Province, China
June, 2009	B.S. Aerospace Engineering, Nanjing University of Aeronautics and Astronautics, Nanjing, Jiangsu Province, China
June, 2016	PhD. Aeronautics and Astronautics, University of Washington, WA, USA